



**KINETICS OF GRAPHITE OXIDATION IN REACTING
FLOW FROM IMAGING FOURIER TRANSFORM
SPECTROSCOPY**

DISSERTATION

Ashley E. Gonzales, Captain, USAF

AFIT-ENP-DS-16-S-024

DEPARTMENT OF THE AIR FORCE
AIR UNIVERSITY

AIR FORCE INSTITUTE OF TECHNOLOGY

Wright-Patterson Air Force Base, Ohio

DISTRIBUTION STATEMENT A

APPROVED FOR PUBLIC RELEASE; DISTRIBUTION UNLIMITED.

The views expressed in this document are those of the author and do not reflect the official policy or position of the United States Air Force, the United States Department of Defense or the United States Government. This material is declared a work of the U.S. Government and is not subject to copyright protection in the United States.

AFIT-ENP-DS-16-S-024

KINETICS OF GRAPHITE OXIDATION IN REACTING FLOW FROM IMAGING FOURIER
TRANSFORM SPECTROSCOPY

DISSERTATION

Presented to the Faculty
Graduate School of Engineering and Management
Air Force Institute of Technology
Air University
Air Education and Training Command
in Partial Fulfillment of the Requirements for the
Degree of Doctor of Philosophy in Optical Sciences and Engineering

Ashley E. Gonzales, MS
Captain, USAF

XXXX 2016

DISTRIBUTION STATEMENT A
APPROVED FOR PUBLIC RELEASE; DISTRIBUTION UNLIMITED.

AFIT-ENP-DS-16-S-024

KINETICS OF GRAPHITE OXIDATION IN REACTING FLOW FROM IMAGING FOURIER
TRANSFORM SPECTROSCOPY

DISSERTATION

Ashley E. Gonzales, MS
Captain, USAF

Committee Membership:

Glen P. Perram, PhD
Chair

Kevin C. Gross, PhD
Member

Marc D. Polanka, PhD
Member

Abstract

This work focuses on the characterization of laser irradiated graphite oxidation using mid-wave infrared (MWIR) imaging Fourier transform spectroscopy (IFTS). Although graphite oxidation has been studied extensively, IFTS uniquely provides spatial characterization of the reacting plumes. Spatial maps of species and temperature provide much needed insight into the transport and kinetic mechanisms and are vital for validation of numerical efforts. The current study builds on previous work using IFTS to characterize graphite oxidation in buoyant flow. Buoyant flow measurements are expanded to a wider range of graphite materials and surface temperatures. Oxidation in flat plate shear flow and stagnation flow are also evaluated to determine the role of transport.

Samples were heated using a $1.07\ \mu\text{m}$ continuous wave (CW) fiber laser. The oxidation plume was observed using MW IFTS camera at spectral resolution of $2\ \text{cm}^{-1}$ and spatial resolution of $0.5\ \text{mm/pixel}$ with framing rates of $1\ \text{Hz}$. Spectral signatures featured emission from CO and CO_2 in the $1800 - 2500\ \text{cm}^{-1}$ spectral region. A two layer radiative transfer model (RTM) using the CDSD-4000 and HITEMP cross-section databases was used to infer spatial maps of temperature and species (CO , CO_2) concentration from spectral data.

Buoyant flow work is an extension of previous work by Acosta [1]. Graphite samples of varying porosity are irradiated at 1000 and $3600\ \text{W/cm}^2$ producing surface temperatures of $1000 - 4000\ \text{K}$ and $3\text{-}8\ \text{mm}$ thick reacting plumes. Plume temperatures are found to be in non-equilibrium with surface temperatures, peaking at $2500\ \text{K}$. CO population was found to be highly correlated with surface temperature as a result of the $C_s + O_2 \Rightarrow 2CO$ and $C_s + CO_2 \Rightarrow 2CO$ surface reactions. A decline in CO_2 population

was observed near laser center due to the $C_s + C O_2 \Rightarrow 2 C O$ reaction. The $[C O]/[C O_2]$ product ratios show a general trend of: $[C O]/[C O_2] = 22 \exp(-6000/T_s)$.

Graphite oxidation in a flat plate shear flow was observed at flow speeds of 5 - 10 m/s ($Re < 7 \cdot 10^4$). Samples were irradiated at 750 and 1500 W/cm², resulting in surface temperatures of 1000 - 4000 K and 2- 4 mm thick reacting plumes. Plume temperatures are again found to be in non-equilibrium with surface temperatures, peaking at 2500 K. $C O$ population was again shown to be highly correlated with surface temperature, with some asymmetry due to flow effects. The decline in $C O_2$ population due to the $C_s + C O_2 \Rightarrow 2 C O$ reaction is less pronounced than in the buoyant case, but can still be observed at laser center. The $[C O]/[C O_2]$ product ratios show a general trend of: $[C O]/[C O_2] = 8 \exp(-3100/T_s)$. This data set represents the first spatially resolved measurements of graphite oxidation in a flat plate shear flow.

Graphite oxidation in a stagnation flow ($v = 1.5$ m/s) was observed at surface temperatures of 1500 - 3100 K, resulting in reacting layers on the order of 1 - 3 mm thick. The $[C O]/[C O_2]$ product ratios show two general trends. At lower temperatures, results compare favorably with previous results with a general trend of $[C O]/[C O_2] = 2 \exp(-2400/T_s)$. At higher temperatures (2200- 2500 K), the $[C O]/[C O_2]$ ratios transition to higher effective activation energies of 16,000 and 31,000 K. This transition coincides with the decline in $C O_2$ and rise in $C O$, suggesting it is a result of the $C_s - C O_2$ reaction. This transition takes place at different temperatures for each of the three cases, possibly due to varying $C O$ population which has been shown to inhibit the $C_s - C O_2$ reaction. This data set represents the first spatially resolved measurements of graphite oxidation in a stagnation flow.

Table of Contents

	Page
Abstract	4
List of Figures	9
List of Tables	15
I. Introduction	1
1.1 Research Objectives	2
1.2 Document Outline	4
II. Background	6
2.1 Summary	6
2.2 Carbon Oxidation	6
Overview	6
Graphite	7
CO Oxidation	8
C _(s) Oxidation	9
[C O]/[C O ₂] Temperature Dependence	14
2.3 Fourier Transform Spectroscopy	15
Radiative Transfer Model	18
2.4 Flow Conditions	19
Flat Plate Shear Flow	19
Buoyant Flow	22
Stagnation Flow	25
III. Oxidation Model	28
3.1 Conservation Equations	28
3.2 1D Model	29
Surface Temperature Sensitivity	32
Flame Length Sensitivity	33
Surface Rate Sensitivity	33
3.3 Quasi 2D Model	34
Surface Temperature Sensitivity	36
Flow Sensitivity	36
IV. Experimental Methods	42
4.1 Laser System and Diagnostics	42
4.2 Graphite Materials	43
4.3 Diagnostics	43

	Page
Thermal Imagery	43
Imaging Fourier Imaging Spectrometer	49
Visible Imagery	55
4.4 Flow Variations	55
Buoyant Flow	55
Flat Plate Shear Flow	56
Stagnation Flow	56
V. Imaging Fourier Transform Spectroscopy of Graphite Oxidation in a Buoyant Flow	60
5.1 Abstract	60
5.2 Introduction	61
5.3 Experimental	64
Materials	65
Plume Measurements	66
Thermal Measurements	68
5.4 Experimental Results and Discussion	69
Emissivity	69
Surface Temperature	70
Plume Properties	72
Diffusion	77
Temperature Dependence of $[CO]/[CO_2]$ Ratio	79
5.5 Model	80
5.6 Model Results and Discussion	83
$[CO]/[CO_2]$ Temperature Dependence	84
Non-uniqueness	85
5.7 Conclusions	86
VI. Imaging Fourier Transform Spectroscopy of Graphite Oxidation in a Flat Plate Shear Flow	89
6.1 Abstract	89
6.2 Introduction	90
6.3 Experimental	91
Overview	91
Materials	93
Plume Measurements	94
Thermal Measurements	95
6.4 Results and Discussion	96
Surface Temperature	96
Plume Properties	97
Irradiance Effects	101
Flow Effects	102

	Page
[CO]/[CO ₂] Temperature Dependence	103
6.5 Model	105
Rate Equations	105
Model Results	107
Non-uniqueness	109
6.6 Conclusions	110
VII. Imaging Fourier Transform Spectroscopy of Graphite Oxidation in a Stagnation Flow	112
7.1 Abstract	112
7.2 Introduction	113
7.3 Experimental	115
Overview	115
Graphite Samples	115
Thermal Measurements	116
Plume Measurements	117
7.4 Results and Discussion	118
Surface Temperature	118
Flow	119
Plume	123
7.5 Conclusions	126
VIII. Conclusions	128
8.1 Recommendations for Future Work	130
Appendix A. Supplemental Data	132
1.1 Graphite Oxidation in Buoyant Flow	132
1.2 Graphite Oxidation in Flat Plate Shear Flow	134
Appendix B. Two-Layer Radiative Transfer Model Error Analysis	138
2.1 Background	138
2.2 Method	139
2.3 Results	142
2.4 Summary	146
Bibliography	147

List of Figures

Figure		Page
1	Carbon oxidation kinetics	7
2	Michelson interferometer	16
3	Sample interferogram, MOPD = 0.3 cm, nOPD = 9480	17
4	Flat plate shear flow boundary layer.	20
5	Buoyant flow over isothermal vertical flat plate.	23
6	Buoyant flow boundary layer thickness as a function of T_s evaluated at $x = L = 10$ cm.	25
7	Stagnation flow.	27
8	1D Flame model for $T_s = 2500$ K and $\delta = 5$ mm: $(-)$ X_{CO} , $(-)$ X_{O_2} , $(-)$ X_{CO_2} , $(\cdot \cdot)$ $X_{O_2}^o$, $(-)$ T_{plume} , $(\cdot \cdot)$ T_{plume}^o , (\square) T_s	32
12	A_2 sensitivity of 1D Flame model with $T_s = 2500$ K and $\delta = 5$ mm. A_2 : $(\cdot \cdot)$ $A_2 = 0.1x A_2^o$, $(-)$ $A_2 = A_2^o$, $(- -)$ $A_2 = 10x A_2^o$. $(-)$ X_{CO} , $(-)$ X_{O_2} , $(-)$ X_{CO_2} , $(\cdot \cdot)$ $X_{O_2}^o$, $(-)$ T_{plume} , $(\cdot \cdot)$ T_{plume}^o , (\square) T_s	34
15	Simulated $(-)$ CO and $(-)$ CO_2 profiles for varying V_∞ : $(\cdot \cdot)$ 5 m/s, $(-)$ 7 m/s, and $(- -)$ 10 m/s.	37
9	1D Flame model for varying T_s at $\delta = 5$ and 10 mm: $(\cdot \cdot)$ $T_s = 2000$ K, $(-)$ $T_s = 2500$ K, $(- -)$ $T_s = 3000$ K. $(-)$ X_{CO} , $(-)$ X_{O_2} , $(-)$ X_{CO_2} , $(\cdot \cdot)$ $X_{O_2}^o$, $(-)$ T_{plume} , $(\cdot \cdot)$ T_{plume}^o , $(\nabla, \square, \Delta)$ T_s	38
10	1D Flame model for varying δ at $T_s = 2000$ and 3000 K: $(\cdot \cdot)$ $\delta = 3$ mm, $(-)$ $\delta = 6$ mm, $(- -)$ $\delta = 9$ mm. $(-)$ X_{CO} , $(-)$ X_{O_2} , $(-)$ X_{CO_2} , $(\cdot \cdot)$ $X_{O_2}^o$, $(-)$ T_{plume} , $(\cdot \cdot)$ T_{plume}^o , (\square) T_s	39
11	A_1 sensitivity of 1D Flame model with $T_s = 2500$ K and $\delta = 5$ mm. A_1 : $(\cdot \cdot)$ $A_1 = 0.1x A_1^o$, $(-)$ $A_1 = A_1^o$, $(- -)$ $A_1 = 10x A_1^o$. $(-)$ X_{CO} , $(-)$ X_{O_2} , $(-)$ X_{CO_2} , $(\cdot \cdot)$ $X_{O_2}^o$, $(-)$ T_{plume} , $(\cdot \cdot)$ T_{plume}^o , (\square) T_s	40
13	A_3 sensitivity of 1D Flame model with $T_s = 2500$ K and $\delta = 5$ mm. A_3 : $(\cdot \cdot)$ $A_3 = 0$, $(-)$ $A_3 = A_3^o$, $(- -)$ $A_3 = 100x A_3^o$. $(-)$ X_{CO} , $(-)$ X_{O_2} , $(-)$ X_{CO_2} , $(\cdot \cdot)$ $X_{O_2}^o$, $(-)$ T_{plume} , $(\cdot \cdot)$ T_{plume}^o , (\square) T_s	40

Figure		Page
14	Simulated (—) CO and (---) CO_2 profiles for varying T_s profiles. T_s are Gaussian ($\sigma = 10$ cm) with peak temperatures of: (..) 2000K, (—) 2500 K, and (---) 3000 K.	41
16	Sample FLIR temperature data using multiple integration times of 0.06, 0.25, 0.8, and 1.5 ms. Masked pixels (black) are outside the calibration region for that integration time setting.	46
17	Sample FLIR temperature data integrating multiple integration times of 0.06, 0.25, 0.8, and 1.5 ms. Masked pixels (black) are outside the calibration region for that integration time setting.	47
18	Temperature error (ΔT) calculated for varying emissivity ($\epsilon=0.6$ (left), 0.8 (center), and 1.0 (right), surface temperature ($T_s = 1000 - 3500$ K), and emissivity error $\Delta\epsilon = 0.01 - 0.15$ using Eq. (108).	48
19	Sample Telops IFTS data. Left: Broadband map evaluated at 2300 cm^{-1} . Masked pixels (black) are outside the calibration region. Right: Spectral radiance at select pixels. Colors correspond to highlighted pixels in the broadband map. Black indicates noise floor.....	50
20	Sample measured spectra and model. (---) measured radiance, L_{det} ; (—) modeled radiance; (---) path transmission, τ_{atmos} ; (—) CO emissivity, ϵ_{CO} ; (---) CO_2 emissivity, ϵ_{CO_2} . Model fits correspond to $T_{plume} = 2240 \pm 40$ K, $X_{CO_2} = 0.112 \pm 0.004$, $X_{CO} = 0.26 \pm 0.03$	52
21	Sample species and temperature maps (top) and uncertainty (bottom) based on 95% fit confidence. Masked values (black) represent areas with no plume data.	54
22	Buoyant flow configuration.....	57
23	Flat plate shear flow configuration.	58
24	Stagnation flow configuration.	59
25	Schematic: laser irradiated graphite in buoyant flow	65

Figure	Page
26	Graphite emissivity versus temperature; Current measurements: material - (Δ) fine, (\diamond) isomolded, (\circ) pyrolytic C-face; surface: irradiated (full), undamaged (open); Autio [2]: (\blacksquare) UF-4-S rough, (\square) UF-4-S polished; (\bullet) pyrolytic A-face, (\circ) pyrolytic C-face polished 70
27	Surface temperatures over time. (—) fine, (— —) isomolded, (— ·) pyrolytic 71
28	Sample measured and simulated spectra for isomolded sample irradiated at 1000 W/cm ² . Pixel located adjacent to surface, near beam center. (---) measured radiance, L_{det} ; (—) modeled radiance; (—) τ_{atmos} ; (—) ϵ_{CO} ; (—) ϵ_{CO_2} . Model fits correspond to $T_{plume} = 2240 \pm 40$ K, $X_{CO_2} = 0.112 \pm 0.004$, $X_{CO} = 0.26 \pm 0.03$ 73
29	Plume temperature and species mole fractions, X_i , inferred from Telops data, isomolded sample irradiated at 1000 W/cm ² and 3600 W/cm ² 74
30	Plume properties along surface normal for isomolded sample irradiated at 1000 W/cm ² and 3600 W/cm ² . (\bullet) CO, (\blacklozenge) CO ₂ , (\blacktriangle) T_{plume} , (X) T_s 75
31	Plume properties along surface (x = 0) for isomolded sample irradiated at 1000 W/cm ² and 3600 W/cm ² . (\bullet) CO, (\blacklozenge) CO ₂ , (\blacktriangle) T_{plume} , (\square) T_s 77
32	Mole fractions and flux along surface for isomolded sample irradiated at 1000 W/cm ² . Top: Mole fraction: (\bullet) X_{CO} , (\blacklozenge) X_{CO_2} ; Bottom: Surface diffusion flux calculated using Eq. (120): (\circ) Γ_{CO} , (\blacklozenge) Γ_{CO_2} 78
33	Mole fractions and flux along surface for isomolded sample irradiated at 3600 W/cm ² . Top: Mole fraction: (\bullet) X_{CO} , (\blacklozenge) X_{CO_2} ; Bottom: Surface diffusion flux calculated using Eq. (120): (\circ) Γ_{CO} , (\blacklozenge) Γ_{CO_2} 79
34	[CO]/[CO ₂] vs T_s evaluated at surface. (\circ) 1000 W/cm ² , (Δ) 3600 W/cm ² , (—) fine, (—) isomolded, (—) pyrolytic 80
35	Diffusion flux along surface for isomolded sample irradiated at 1000 W/cm ² . Diffusion flux calculated using Eq. (120): (\circ) Γ_{CO} , (\blacklozenge) Γ_{CO_2} . Diffusion flux approximated using Eq. (128): (—) Γ_{CO} 82

Figure	Page
36	Sample model fits for fine sample irradiated at 3600 W/cm ² . Top: temperature measurements: (□) T_s , (▲) T_{plume} , Middle: modeled rates: (---) R_1 , (—) R_2 , (—) $\Delta x R_g$, (—) Γ_{d-CO} , and (---) Γ_{c-CO} . Bottom: species concentrations- (●) - measured CO , (◆) - measured CO_2 , (—) modeled CO , (---) modeled CO_2 , (---) modeled O_2 , and (...) freestream O_2^o 84
37	Schematic: laser irradiated graphite in flat plate shear flow. 92
38	Surface temperatures over time. Material: (—) fine, (—) isomolded, (—) pyrolytic. Flow: (· ·) 5 m/s, (---) 7 m/s, (—) 10 m/s. 97
39	Sample spectra and fit for isomolded sample irradiated at 1500 W/cm ² with 5 m/s flow ² . (—) measured radiance, L_{det} , (—) modeled radiance, (—) path transmission, τ_{atmos} , (—) CO emissivity, ϵ_{CO} , (—) CO_2 emissivity, ϵ_{CO_2} . Model fits correspond to $T_{plume} = 2000 \pm 20$ K, $X_{CO_2} = 0.073 \pm 0.001$, $X_{CO} = 0.15 \pm 0.01$ 98
40	Plume temperature and species mole fractions, X_i , inferred from Telops data, fine sample irradiated at 1500 W/cm ² with 7 m/s flow. 99
41	Plume properties normal to the surface at laser center ($x = 0$) for fine samples irradiated at 1500 W/cm ² with 7 m/s flow. (●) CO , (◆) CO_2 , (▲) T_{plume} , (X) T_s 99
42	Plume properties along the surface ($x = 0$) for a fine sample irradiated at 1500 W/cm ² with 7 m/s flow. (●) CO , (◆) CO_2 , (▲) T_{plume} , (□) T_s 100
43	Plume properties along the surface (top) and normal to surface (bottom) for a fine sample irradiated at 750 W/cm ² (solid) and 1500 W/cm ² (open) with 5 m/s flow. Markers: (●) CO , (◆) CO_2 , (▲) T_{plume} , (■) T_s 101
44	$[CO]/[CO_2]$ vs T_s evaluated at surface for fine samples irradiated at 750 W/cm ² (●) and 1500 W/cm ² (○) with flow speeds of 5 m/s 103
45	Plume properties along the surface (top) and normal to surface (bottom) for a fine sample irradiated at 750 W/cm ² for $V = 5$ m/s (solid) and 10 m/s (open). Markers: (●) CO , (◆) CO_2 , (▲) T_{plume} , (■) T_s 104

Figure	Page
46	$[CO]/[CO_2]$ vs T_s evaluated at surface for isomolded samples irradiated at 1500 W/cm^2 with flow speeds of 5 m/s (●) and 10 m/s (○) 105
47	$[CO]/[CO_2]$ vs T_s evaluated at surface for all test cases. Material: (●) fine, (●) isomolded, (●) pyrolytic. Flow: (▽) 5 m/s, (○) 7 m/s, and (△) 10 m/s. Fit: (-) $[CO]/[CO_2] = 7.8 \exp(-3130/T_s)$ 106
48	Sample model fitting for an isomolded sample irradiated at 1500 W/cm^2 with 7 m/s flow. Top: temperature measurements - (▲) T_{plume} , (□) T_s . Middle: simulated rates - (-) CO diffusion flux, Γ_{d-CO} , (- -) CO net convection flux $\Delta\Gamma_{c-CO}$, (- -) CO oxidation rate $\Delta x R_g$, (- -) R_1 , (-) R_2 , Bottom: Species concentrations - Measurements: (●) CO, (◆) CO_2 , Model: (-) CO, (- -) CO_2 , (- -) O_2 , (..) O_2^o 108
49	Schematic: laser irradiated graphite in stagnation flow 116
50	Surface temperatures over time at irradiances of: (- -) 650 W/cm^2 ; (-) 900 W/cm^2 ; (- . -) 2400 W/cm^2 119
51	Sample interferogram, Y , and FFT, $\mathcal{F}(Y)$ 120
52	Velocity field for stagnation flow ($v=1.5 \text{ m/s}$) on sample irradiated at 2400 W/cm^2 . Broadband image in background included for spatial reference. 122
53	Species and temperature maps for sample irradiated at $I = 900 \text{ W/cm}^2$ for $t = 100 \text{ s}$ producing peak surface temperatures of $T_s = 2290 \text{ K}$ 123
54	Species and temperature over time (●) X_{CO} , (◆) X_{CO_2} , (▲) T_{plume} , (-) T_s 124
55	$[CO]/[CO_2]$ versus inverse surface temperature. Data: (□) $I = 650 \text{ W/cm}^2$ (◆) $I = 900 \text{ W/cm}^2$ (●) $I = 2400 \text{ W/cm}^2$. Fits to Eq. (??): (-) $\alpha = 1.7 \pm 0.3, \beta = 2,400 \pm 400 \text{ K}$; (- . -) $\alpha = 580 \pm 10, \beta = 16,000 \pm 3,000 \text{ K}$; (- -) $\alpha = 8.7 \cdot 10^5 \pm 0.3 \cdot 10^5, \beta = 31,000 \pm 4,000 \text{ K}$ 126
56	Graphite oxidation in buoyant flow 133
57	Oxidation of fine porosity graphite in flat plate shear flow 135
58	Oxidation of isomolded graphite in flat plate shear flow..... 136

Figure		Page
59	Oxidation of pyrolytic graphite in flat plate shear flow.....	137
60	Simulated Gaussian flame profile. Temperature: $\sigma_{g-T} = 1$ cm with peak value of $T_{plume} = 1500$ K. Species: $\sigma_{g-c} = 0.7$ cm with peak values of $X_{CO_2} = 0.2$ and $X_{CO} = 0.3$	140
61	Line of sight spectra generated using Eq. (148) for peak T_{plume} , CO , and CO_2 of 1500 K, 0.1 and 0.2 respectively. Color corresponds to line of sight location with red corresponding to flame center with LOS spacing of $\Delta x = 0.05$ cm.	141
62	Sample two-layer model fit to simulated line of sight spectra. (---) simulated measured radiance, (—) two-layer RTM radiance, (—) τ_{atmos} ; (—) ϵ_{CO} ; (—) ϵ_{CO_2} . Model fits correspond to $q_{CO} = 0.492 \pm 0.002$ cm, $q_{CO_2} = 0.139 \pm 0.0004$ cm, and $T_{plume} = 1388 \pm 1$ K,	143
63	Comparison of two-layer RTM results with truth values using (a) constant and (b) variable flame length methods. Truth values: (—) radial profile, (—) line of sight averaged, (—) T_{plume} , (—) X_{CO} , (—) X_{CO_2} . Two-layer RTM fit values: (▲) T_{plume} , (●) X_{CO} , (◆) X_{CO_2}	145

List of Tables

Table	Page
1	<i>CO</i> oxidation rate parameters. Rates of the form of Eq. (5).9
2	$C_{(s)}$ oxidation rates where $k_{si} = A_i \cdot \exp(-E_i/T)$ 13
3	Summary of carbon oxidation studies; α , β , and n correspond to fit coefficients for Eq. (18) 15
4	Simulation parameters 31
5	Graphite materials [3] 43
6	Reactions and activation energies 61
7	Summary of carbon oxidation studies; Values of A,B, n correspond to Eq. (116) 63
8	Graphite materials [3] 66
9	Emissivities for undamaged and irradiated samples 69
10	Simulation parameters. 85
11	Oxidation mechanisms 90
12	Graphite materials [3] 94
13	Simulation parameters. 109
14	Oxidation mechanisms 113
15	Graphite properties [3] 116
16	Test matrix: graphite oxidation in buoyant flow 132
17	Test matrix: graphite oxidation in flat plate shear flow 134

KINETICS OF GRAPHITE OXIDATION IN REACTING FLOW FROM IMAGING FOURIER TRANSFORM SPECTROSCOPY

I. Introduction

High energy lasers (HEL) are an attractive weapons system option due to their low incremental costs compared to traditional weapons systems [4]. Effective use of this technology requires detailed knowledge of the laser material interaction to gage the lethal fluence, defined as the delivered laser energy per unit area required to damage a particular material. Estimating lethal fluence often relies heavily on experimental data to develop empirical parameters for system configuration, which can be costly given the numerous laser-material-environment combinations. Recently, efforts have been made to model the laser-material interaction, allowing the transition from costly experimental data to predictive modeling. Developing an effective model requires detailed knowledge of the processes governing the laser-material interaction, such as heating and cooling of the material, surface oxidation, ablation, sublimation, and combustion kinetics of the resulting plume [5].

The focus of this work is to characterize surface oxidation and plume kinetics of laser irradiated graphite. While graphite is not a typical material of interest for weapons applications, it has several advantages from a research perspective and is useful as a stepping point for more relevant materials. The relative composition simplicity of graphite, consisting primarily of carbon, greatly simplify surface oxidation mechanisms. Carbon oxidation has been studied extensively, both theoretically and experimentally, and has recently expanded to CFD studies with the availability of surface kinetic packages [6]. Despite the high level of interest, much is still not understood about the kinetic

mechanisms. This is in part due to the lack of spatially resolved experimental data for validation of theoretical and numerical efforts.

Mid-wave infrared (MWIR) imaging Fourier transform spectroscopy (IFTS) has recently been demonstrated as a useful tool for the study of combustion systems. The hyperspectral (spatial - spectral) data provide a wealth of information to characterize the material-oxidizer interaction. Combustion species (CO , CO_2 , H_2O) and plume temperature can be inferred from the spectral content at each image pixel, allowing for full spatial characterization of the combustion plume. Recent laser lethality work has demonstrated the usefulness of IFTS in characterizing laser irradiated graphite, fiberglass reinforced polymers (FRP), and poly(methyl methacrylate) (PMMA) [7].

The present study focuses on characterizing graphite oxidation using IFTS hyperspectral imagery. The primary goal of this study is to characterize the surface oxidation and plume kinetics coupling. The secondary goal is to provide experimental data to assess the validity of the numerical model being developed through research partnerships. Oxidation was evaluated in three flow conditions. Buoyant flow measurements will focus on expanding work by Acosta and characterizing surface kinetics. Flat plate and stagnation flow cases will gain understanding of the role of mass transport as well as provide data needed for validation of numerical work.

1.1 Research Objectives

The focus of this work was to characterize of graphite oxidation in a reacting flow. This was achieved through three objectives:

1. **Characterization:** Characterize graphite oxidation using IFTS.

Graphite oxidation was characterized using IFTS to provide species and temperature maps. Three graphite materials were evaluated at surface temperatures of 1000 - 4000 K to determine dependence on surface temperature and material.

Plume properties and surface temperature were inferred from IFTS and MW thermal imagery, respectively. Three flow conditions were evaluated to highlight the role of transport mechanisms: buoyant flow (Chapter IV), flat plate shear flow (Chapter V), and stagnation flow (Chapter VI). Differences in oxidation plumes and $[CO]/[CO_2]$ product ratios for each flow condition are discussed.

Two techniques were developed to infer diffusion and convective transport properties from IFTS data. Diffusion transport is estimated using species gradients inferred from 2D species maps. Convective transport is characterized through visualization of the velocity flow field. Velocity fields are estimated using the cross-correlation of low frequency signal oscillations in neighboring pixels to estimate the flow travel time. Repeating across the array then gives a full spatial flow velocity map, enabling visualization of convective transport.

2. **Modeling:** Develop an oxidation model incorporating transport and kinetics.

While ideally the oxidation process would be modeled using CFD coupled with kinetic packages, these methods are computationally expensive and lack the simplicity to develop intuition. Two simplified models were developed to gain intuition on the role of transport and kinetic mechanisms.

A simple 1D model based on previous theoretical work is presented. A system of ordinary differential equations (ODEs) is derived from species and energy conservation equations incorporating surface and gas phase kinetics and diffusion transport (neglecting convection). A numerical boundary value solver is used to determine species concentration and temperature normal to the surface. Results are in general agreement with trends reported experimentally. Derivation of the model and sample simulations are presented in Chapter III.

A quasi 2D model was then developed to incorporate kinetics, diffusion transport

(normal to surface), and convective transport (along surface). Species and energy conservations are applied to a small control volume adjacent to the surface. Approximations to diffusion transport are applied to simplify the system of equations to a set of ODEs. A numerical solver is then used to determine species concentration and temperature along the surface. Trends are in general agreement those observed experimentally. Derivation of the model is presented in Chapter III. Model results are compared with experimental observations in Chapters IV and V.

3. **CFD Validation:** Provide experimental data for validation of numerical results.

A research partnership has been established with the University of Virginia (UVa) to aid in the numerical modeling of the surface and plume oxidation [8]. Numerical simulations of high temperature graphite oxidation in stagnation and flat plate flow have been completed. The experimental work was designed to compliment numerical efforts and provide data for validation. Experimental results provide the first sub-mm resolved measurements of graphite oxidation in reacting flow (both flat plate and stagnation). Unfortunately, we were unable to match experimental conditions to existing simulations, but this work will provide valuable data for validation of future CFD efforts. This objective is met though the flat plate and stagnation flow data found in Chapters V and VI. Additional data can be found in Appendix A.

1.2 Document Outline

An outline of the document is presented to highlight the document organization and the material presented in each chapter. Chapter II provides a more in depth coverage of the relevant background material, including a review of carbon oxidation kinetics and an introduction to IFTS and its application as a combustion diagnostic. Chapter III presents the two oxidation models, including their derivation and simulation trends.

Each of the central chapters (IV, V, VI) represent experimental work in each of the three flow conditions evaluated: buoyant, flat plate shear flow, and stagnation flow, respectively. Each central chapter is intended for submission to publication and can be read as a stand alone document. Supplemental data and figures for the three flow conditions can be found in Appendix A. Finally, conclusions and recommendations for future work can be found in Chapter VII.

II. Background

2.1 Summary

This chapter provides a review of the basic concepts needed to describe graphite oxidation and the diagnostics used in this study. Section 2.2 covers the basics of carbon oxidation, the mechanisms involved, and a review of previous experimental work. Section 2.3 includes an introduction to Fourier transform spectroscopy, which is primary diagnostic used in this study. Lastly, Section 2.4 provides background for each of the flow configurations used in this study, including basic fluid equations.

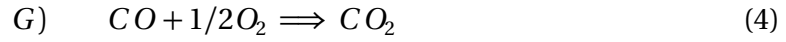
2.2 Carbon Oxidation

Overview.

Extensive research on carbon oxidation has been done due to its applications in coal/char combustion [9–11]. Despite numerous studies, much of the kinetics is still not well understood. The main source of complexity in carbon oxidation is the coupling of heterogeneous and homogeneous reactions, which make it difficult to measure surface mechanisms independently. A graphic summary of the reacting system is shown in Figure 1. Oxidizing species (O_2 , CO_2) diffuse to the surface and react with carbon, producing CO and CO_2 through S1, S2, and S3:



The CO diffuses away from the surface and oxidizes with O_2 , producing CO_2 through the gas phase reaction:



The CO_2 produced in the CO oxidation reaction can then diffuse to the surface to supply the $C_s - CO_2$ reaction. The gas phase reaction is then critical in determining the availability of oxidizer at the surface, both through preventing O_2 diffusion to the surface and supplying CO_2 . Additionally, this coupling makes direct measurement of $C_s - O_2$ reactions challenging as it difficult to prevent CO produced at the surface from oxidizing in the O_2 environment [10].

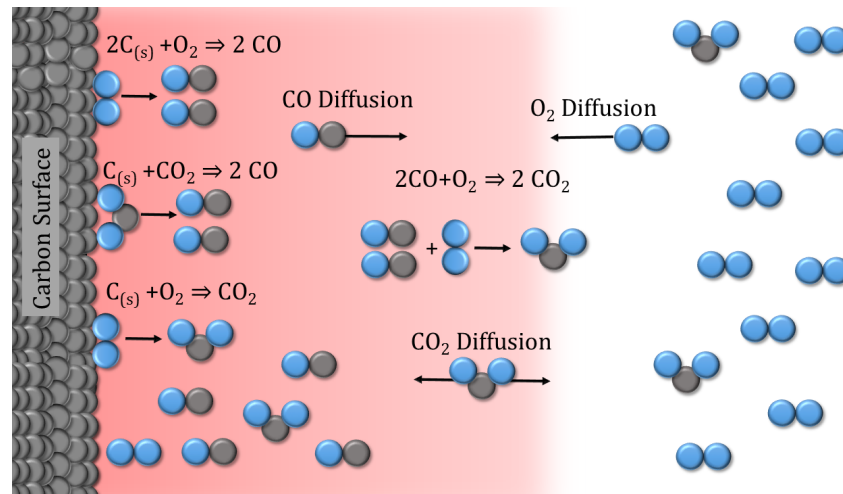


Figure 1. Carbon oxidation kinetics

Graphite.

Graphite is a popular material for studying carbon oxidation due to its high carbon content and availability. Although it can be mined naturally, most forms commonly found are manufactured. Synthetic graphite is composed predominantly of coke, carbon

black, natural graphite, and binder [12]. The coke, carbon black, and graphite are ground into a powder and held together with a coal, petroleum, or resin based binder. The mixture is then shaped, typically using isostatic press, extrusion, or die molding. Heat treatment varies, but typically involves at least two stages. In the first stage, the formed mixture is slowly heated in vacuum to remove any volatiles which may be present in the binder. A filler material may be used to fill the voids left by the escaped volatiles. In the second stage, the material is heated treated ($T \approx 3300$ K) which helps graphitize the material and remove any remaining volatiles and impurities. As a result of variation in these production steps, graphite materials often vary in porosity and impurity content, which can result in some variation in surface reactivity.

CO Oxidation.

Oxidation of CO has been widely studied due to its application in most combustion processes. While CO oxidation is written simply as the global reaction in Eq. (4), in reality it consists of many elementary reactions between CO , CO_2 , O_2 , and H_2O as well as their radicals (OH , H , O , etc). H_2O is critical in to the production of H and OH radicals which control propagating and branching reactions [13]. Extensive research has been done to develop kinetic packages consisting of a finite number of elementary reactions, while still adequately characterizing CO oxidation over a range of conditions. For example, the model proposed by Yetter et al. consists of 28 elementary reactions between 12 species [13].

For simplicity, it is often desired to use a single step **global reaction** with empirical coefficients, typically expressed as [14]:

$$R_g = [CO][O_2]^a [H_2O]^b \cdot A_g \exp\left(\frac{-E_g}{RT_p}\right) \quad (5)$$

where R_g is the gas phase oxidation rate in mol/m³/s, $[C_i]$ is the concentration of

species C_i in mol/m^3 , and $A_g \exp(\frac{-E_g}{RT_p})$ is the Arrhenius rate coefficient, k_g , with pre-exponential factor A_g in $(\text{mol/m}^3)^{-(a+b)}/\text{s}$, activation energy E_g in kcal/mol , and universal gas constant R . The $[H_2O]^b$ term is added to incorporate the influence of H_2O and its radicals in propagating reactions. Rate coefficients from previous studies are shown in Table 1. Parameters obviously vary widely, most notably the pre-exponential factors, which can vary by five orders of magnitude. One study evaluating the validity of these single step reaction rates determined that rate parameters are subject to the particular test conditions (temperature, pressure, mixture composition), and often deviate significantly when evaluated outside of the given test range [14]. Current work will use rate parameters by Soblev, which were inferred at plume temperatures of 1900 - 2400 K with $> 5\%$ O_2 and 2% H_2O [15], which are closest to the range of current test conditions ($T = 1500 - 2500 \text{ K}$, $< 1\%$ H_2O , $P = 1 \text{ atm}$).

Table 1. CO oxidation rate parameters. Rates of the form of Eq. (5).

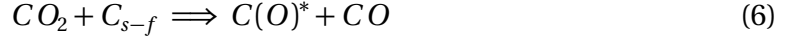
Reference	T (K)	P (atm)	O_2 (%)	H_2O (%)	A_g (*)	E_g ($\frac{\text{kcal}}{\text{mol}}$)	a	b
Friedman [16]	2010	0.06	14-16	-	$5.30 \cdot 10^6$	20	0.5	0
Hottel [17]	1280-1535	0.25-1	5-10	0-3.7	$1.74 \cdot 10^6$	16	0.5	0.3
Dryer [18]	1050-1200	1	-	0.1-3	$1.23 \cdot 10^{10}$	40	0.25	0.5
Lyon [19]	1123-1298	1-2	-	-	$4.74 \cdot 10^5$	24	0.5	0.25
Howard [20]	1060-1260	1	0.7-1.7	15-18	$1.30 \cdot 10^8$	30	0.5	0.5
Soblev (a) [15]	1910-2400	1	0.5-73	2	$3.00 \cdot 10^9$	30	0.25	0
Soblev (b) [15]	1910-2400	1	0.5-73	2	$1.70 \cdot 10^7$	27	0.2	0

(*) Units for A_g are in $(\text{mol/m}^3)^{-(a+b)}/\text{s}$.

$C_{(s)}$ Oxidation.

A full review of carbon surface oxidation mechanisms can be found in work by Laurendeau [10]. Each surface oxidation mechanism can be roughly outlined in three

steps: 1) oxidizer adsorption to produce active sites, 2) migration of active sites, and 3) desorption of products. These steps for the $C_s - CO_2$ surface reaction given by Eq. (2) can be written as follows:



where C_{s-f} represents a free carbon site, and $C(O)^*$ and $C(O)^{\prime}$ represent two active sites [10]. The simplest kinetic model of this system is the Langmuir-Hinshelwood model, which relies on three main assumptions: instantaneous migration, no interaction of adsorbed species, and a uniform reacting surface. Using these assumptions, the rates of adsorption and desorption can then be written as:

$$R_a = k_a [C_{ox}] \theta_f^{\zeta} \quad (9)$$

$$R_d = k_d (1 - \theta_f)^{\zeta} \quad (10)$$

where k_a and k_d are the adsorption and desorption rate coefficients in Arrhenius form, $[C_{ox}]$ is the oxidizer concentration, θ_f is the fraction of free carbon sites, and ζ refers to single ($\zeta = 1$) or dual ($\zeta = 2$) site interactions. Assuming equilibrium, $R_a = R_d = R_s$, and single site interactions ($\zeta = 1$), yields the surface reaction rate:

$$R_s = k_a \frac{[C_{ox}]}{1 + a[C_{ox}]} \quad (11)$$

$$a = \frac{A_a}{A_d} \exp\left(\frac{E_d - E_a}{RT}\right) \quad (12)$$

where A_i and E_i are the pre-exponential factors and activation energies for adsorption and desorption. Evaluation of Eq. (11) for the two extremes of $a[C_{ox}]$ yields the first and zero order expressions:

$$R_s = \begin{cases} k_a[C_{ox}] & a[C_{ox}] \ll 1 \\ k_d/a & a[C_{ox}] \gg 1 \end{cases} \quad (13)$$

Global reaction rates for each surface oxidation mechanism are therefore typically expressed using the form :

$$R_s = k_s[C_{ox}]^m \quad (14)$$

with reaction order $0 < m < 1$.

The limits of the Langmuir-Hinshelwood model assumptions are discussed in detail by Laurendeau [10]. First, take the assumption of no interaction of adsorbed species. Measurements have shown that both E_a and E_d are influenced by the fraction of active sites, $\theta_s = 1 - \theta_f$. For the adsorption process, as more sites become active, the more repulsive the surface becomes to potential adsorbed species, increasing the activation energy. For desorption, the process is reversed, with desorption activation energy decreasing with increasing reactivity. The simplest modification to reflect these observations is a simple linear correction:

$$E_a = E_{a0} + \omega_a \theta_s \quad (15)$$

$$E_d = E_{d0} - \omega_d \theta_s \quad (16)$$

where ω_a and ω_d describe the degree of influence of active sites. The second assumption of a uniform reacting surface implies a single activation energy. However, experimental work has already shown activation energies to exhibit a Gaussian distribution [21].

Despite these limitations Eq. (14) remains the most popular expression for surface kinetics due to its simplicity.

Measurements of the surface oxidation rates are difficult due to the coupling of the surface and gas phase reactions. This is particularly problematic in $C_s - O_2$ measurements where the available O_2 can further oxidize surface products and influence measurements. For techniques where the gas is captured and analyzed, the O_2 in the mixture can quickly oxidize CO , creating CO_2 before the gas sample is analyzed. It is therefore difficult to determine if observed CO_2 was created through surface production or CO oxidation [22, 23]. This has led to much debate over the S3 reaction. Although spatially resolved techniques, such as IFTS, can vastly improve our understanding of these surface mechanisms, there is still room for false interpretation of surface CO_2 . CO produced through S1 and S2, either at the surface or within the pores, can easily be oxidized at the surface given a significant O_2 population, producing a high surface CO_2 which can falsely interpreted as the S3 reaction.

Reactions considered for this study are shown in Table 2, which consider only $C_s - CO_2$ and $C_s - O_2$ reactions. Much work has been done on the $C_s - CO_2$ interactions [24–30]. Most debated about this reaction is the inhibition of the S2 reaction by CO , which has been noted in experimental work. Gadsby proposed this is result of CO occupation of active sites, preventing CO_2 absorption [26]. Ergun however believed this to be a result of CO reacting with $C(O)$ produced in the intermediate steps [24, 25]. In either case, a more complex form of the S2 reaction rate is derived, taking into account these elementary steps. However for simplicity, a first order Arrhenius expression, as given in Eq. (14), is often desired. Large variation is seen in pre-exponential factors and activation energies vary across literature, with reported E_i values ranging from 24,000 - 43,000 K.

$C_s - O_2$ reactions are much more difficult to characterize [10]. Central to this issue is

the secondary reactions which take place in the O_2 environment, making it difficult to isolate surface oxidation reactions. This has led to much debate on the $C_s - O_2$ products, where some believe the CO_2 observed at low surface temperatures is a direct result of the S3 reaction and others believe this to be the result of CO oxidation [31]. Large variation in pre-exponential factors and activation energies is reported, with E_i values ranging from 8,100-40,300 K [21, 32–34].

Overall, reported surface reaction rates vary wildly in pre-exponential factor and activation energy. Some of this may be attributed to the reasons discussed previously such as measurement limitations, coupling with gas phase reactions, E_a distributions, and θ_s dependence. Additionally, variation in reactivity has been linked to graphite composition and manufacturing method. Graphite composition can alter activation energy due to catalytic effects of trace minerals [10, 35]. Changes in production method can also result in variations in material porosity. Samples with high volatile content can increase in porosity due to pyrolysis of filler material as the sample is initially heated [27]. Pores then effectively create additional reactive surface area, increasing pre-exponential factors.

Table 2. $C_{(s)}$ oxidation rates where $k_{si} = A_i \cdot \exp(-E_i/T)$

Reaction	R_{s-i} (mol/m ² /s)	E_i (K)	Reference
(S1)	$[O_2]k_{s1}$	8,100-40,300	[21, 32–34]
(S2)	$[CO_2]k_{s2}$	24,000-43,300	[27–30, 36]
(S3)*	$[O_2]k_{s3}$	8,100-40,300	[21, 32, 34]

* mechanism debated

$[CO]/[CO_2]$ Temperature Dependence.

Numerous studies on carbon oxidation have been completed to date. Plots of $[CO]/[CO_2]$ versus T became popular to describe the oxidation process. In 1951, Arthur investigated carbon oxidation at low temperature (730 - 1170 K) using $POCl_3$ to suppress CO oxidation and isolate the effects from surface kinetics [37]. Two carbon materials were evaluated, an artificial graphite and coal char, to determine variation in reactivity between carbon materials. The reacted gases were then fed to a Haldane apparatus to determine CO , CO_2 , and O_2 . $[CO]/[CO_2]$ for the two carbon materials showed an exponential dependence on temperature, establishing the following expression:

$$\frac{[CO]}{[CO_2]} = 2500 \exp\left(-\frac{6,240}{T}\right) \quad (17)$$

Future carbon oxidation work continued to report data in terms of $[CO]/[CO_2]$ expressed in Arrhenius form:

$$\frac{[CO]}{[CO_2]} = \alpha \cdot [O_2]^n \exp\left(-\frac{\beta}{T}\right) \quad (18)$$

where α , β , and n are determined through fitting of experimental data. A summary of experimental studies is shown in Table 3. Much of the work was originally done using gas sampling techniques, such as mass spectrometers [21, 39–41, 89]. However this can lead to lower CO/CO_2 ratios as CO can further evolve into CO_2 given the time between sampling and analyzing. The more recent work by Acosta presented the first spatially resolved measurements of carbon oxidation using IFTS [1]. This technique shows much improvement over gas sampling techniques due to the ability to isolate species located directly adjacent to the surface. However, reported β values are significantly higher than those in earlier literature, possibly due to measurements being taken during the transient heating period and not purely during steady state.

Table 3. Summary of carbon oxidation studies; α , β , and n correspond to fit coefficients for Eq. (18)

Author	Ref	Material	T_s (K)	α	β (K)	n
Arthur	[37]	graphite, coal	730-1170	2510	6,240	-
Rossberg	[38]	electrode carbons	790-1690	1860	7,200	-
Tognotti	[39]	char, spherocarb	670-1670	50	3,070	-0.21
Otterbien	[40]	graphite, vitreous carbon	781-863	26	3,020	-0.18
Phillips	[41]	graphon	800-950	140-200	3,220	-
Du	[21]	soot	670-890	120	3,200	-0.23
Walker	[42]	graphon	800-950	170	3,220	-
Acosta	[7]	graphite	1800-2900	4910	17,970	-

Although Eq. (18) is useful in comparing experimental results, there are clearly limitations to using it as a universal expression for $[CO]/[CO_2]$. Several studies have focused on developing a kinetic-transport based expression for $[CO]/[CO_2]$ which can be applied for a larger range of test conditions and give insight into how rate parameters, species concentration, and transport influence $[CO]/[CO_2]$ [21, 43]. However, these expressions are typically only validated for a limited set of data and experimental conditions.

2.3 Fourier Transform Spectroscopy

Fourier transform spectrometers (FTS) are an attractive option due to their high spectral resolution and throughput compared to dispersive spectrometers [44]. The MWIR is a desirable spectral region for many combustion applications due to the presence of CO , CO_2 , and H_2O spectral signatures in the 1500-4000 cm^{-1} region. One type of FTS is a Michelson interferometer, which is shown in Figure 2. The incoming source beam is divided into two paths. One passes through the beam splitter, is reflected off a moving mirror, and then reflected off the beam splitter onto the detector. The second is deflected off a beam splitter and onto a fixed mirror, and then reflected back

through the beam splitter and onto the detector. A compensator plate is used to such that each beam makes three passes through the compensator or beamsplitter material. As the mirror is moved, an interference pattern is formed at the detector due to the optical path difference (OPD) between the two beams, with the maximum signal given when OPD is zero, or zero path difference (ZPD).

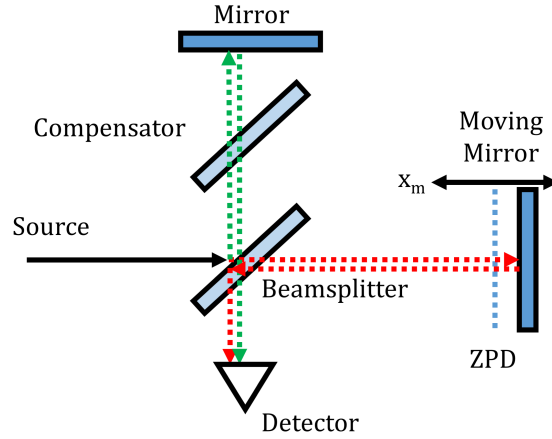


Figure 2. Michelson interferometer

The interference pattern formed over a full mirror sweep is called an interferogram. The measured intensity at each mirror position, $I(x_m)$, is given by:

$$I(x_m) = \frac{1}{2} \int_0^\infty [1 + \cos(2\pi \nu x_m)] [G(\nu)(L(\nu) + O(\nu))] d\nu = I^{DC} + I^{AC}(\nu) \quad (19)$$

ν is the wavenumber, $G(\nu)$ is the gain response of the instrument and includes the spectral response of the FPA and optics, $L(\nu)$ is the spectral radiance of the scene, and $O(\nu)$ is the offset which includes radiation emitted by the camera. A sample interferogram is shown in Figure 3 with maximum OPD (MOPD) of 0.3 cm. The measured signal can be decomposed into a constant offset, I^{DC} , and the modulated component, I^{AC} , which carries the spectral information. Low frequency oscillations, referred to as scene change

artifacts (SCA), are sometimes observed in the I^{DC} component. These are below the cut-off frequency of the interference modulation and are attributed to oscillations in the scene[45].

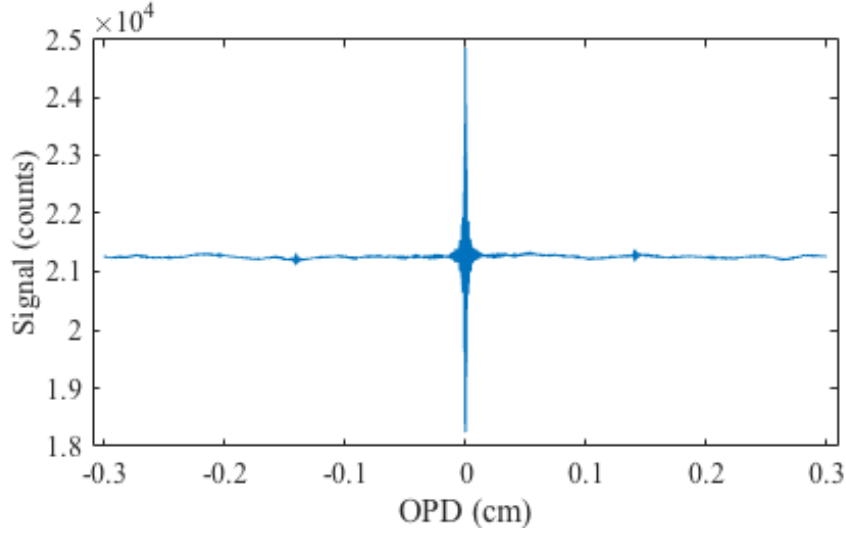


Figure 3. Sample interferogram, MOPD = 0.3 cm, nOPD = 9480

The uncalibrated spectrum is then produced by taking the fast Fourier transform (FFT) of the interferogram:

$$Y(\nu) = \mathcal{F}[I(x_m)] \quad (20)$$

The calibrated spectrum is then calculated using $Y(\nu)$ and the characterized instrument response:

$$L(\nu) = \frac{Y(\nu)}{G(\nu)} - O(\nu) \quad (21)$$

where gain and offset are determined using a blackbody calibration procedure described in Chapter IV.

Radiative Transfer Model.

A radiative transfer model (RTM) is used to infer plume properties from the measured spectra. The **simplest RTM** is the single layer model where the measured spectral radiance is expressed as:

$$L = \varepsilon(\alpha)B(T) \quad (22)$$

where $B(T)$ is the blackbody spectral radiance at temperature T , and emissivity, ε , is defined in terms of optical depth α as:

$$\varepsilon = 1 - \exp(-\alpha) \quad (23)$$

Optical depth is determined by the flame composition and can be expressed as:

$$\alpha = n\ell \sum_i X_i \sigma_i(\nu, T) \quad (24)$$

where n is concentration, ℓ is path length, X_i is the mole fraction of species i , and σ_i is the cross-section of species i at temperature T . Cross-sections are provided for common combustion species by spectral databases, such as HITRAN or CDSD [46, 47].

Most systems however require at the very least a two layer RTM. In this case, the two layers consist of the flame layer and the atmospheric layer between the flame and the detector. The measured radiance can be expressed as:

$$L_{det} = \tau_{atmos} L_{plume} + L_{atmos} \quad (25)$$

where L_{plume} and L_{atmos} are the plume and path radiance defined similarly by Eq. (22), and path transmissivity, τ_{atmos} is expressed as:

$$\tau_{atmos} = 1 - \varepsilon_{atmos}(n, X_{i-atmos}, T_{atmos}, \ell_{atmos}) \quad (26)$$

For typical combustion applications L_{atmos} is neglected ($L_{atmos} \ll L_{plume}$). The measured radiance is then expressed as:

$$L_{det} = \tau_{atmos} \cdot \epsilon_{plume} \cdot B(T_{plume}) \quad (27)$$

A nonlinear fit routine is used to determine plume and atmospheric values for X_i and temperature.

2.4 Flow Conditions

Graphite oxidation **is** evaluated in three flow conditions: buoyant flow, flat plate shear flow, and stagnation flow. For non-reacting flow, each of these flow conditions has been well studied, both theoretically and experimentally. An overview of each flow configuration, including the basic governing equations, is provided in the following sections.

Flat Plate Shear Flow.

One of the most commonly evaluated forced flow problems is the flat plate shear flow, also known as flat plate in a parallel flow, as shown in Figure 4. This case considers a uniform freestream velocity, u_∞ , incident on a flat plate with uniform temperature T_s . A boundary layer is formed between the no-slip condition imposed by the wall, $u(y=0)=0$, and the freestream velocity $u(y \rightarrow \infty)=u_\infty$. Similarly, a thermal boundary layer is also formed due to the temperature gradient. This problem has been studied extensively to determine expressions for boundary layer and thermal boundary layer **thickness**.

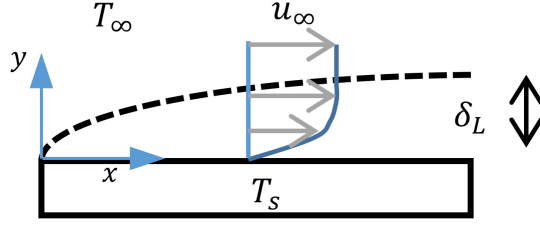


Figure 4. Flat plate shear flow boundary layer.

For this problem, the conservation mass and energy can be expressed as [48]:

$$u \frac{\partial u}{\partial x} + v \frac{\partial u}{\partial y} = \nu_k \frac{\partial^2 u}{\partial y^2} \quad (28)$$

$$u \frac{\partial T}{\partial x} + v \frac{\partial T}{\partial y} = \alpha_T \frac{\partial^2 T}{\partial y^2} \quad (29)$$

where u and v are the x and y velocity components, ν_k is the kinematic viscosity, and α_T is the thermal diffusivity. Boundary conditions are imposed by the wall ($u(0) = v(0) = 0, T(0) = T_s$) and freestream conditions ($u(x \rightarrow \infty) = u_\infty, T(x \rightarrow \infty) = T_\infty$). The similarity solution approach, developed by Blasius, uses a transformation of variables to reduce partial differential equations given by the conservation equations to a set of ordinary differential equations (ODEs), which can be solved numerically [48, 49]. For

the flat plate case, the following variable substitutions are used:

$$u = \frac{\partial \psi}{\partial y} \quad (30)$$

$$v = -\frac{\partial \psi}{\partial x} \quad (31)$$

$$\eta = y \sqrt{\frac{u_\infty}{\nu_v x}} \quad (32)$$

$$\psi = f(\eta) \left[u_\infty \sqrt{\frac{\nu_v x}{u_\infty}} \right] \quad (33)$$

$$\theta_T = \frac{T - T_s}{T_\infty - T_s} \quad (34)$$

Eq. (28) and (29) can then be written as:

$$2f''' + ff'' = 0 \quad (35)$$

$$\theta_T'' + \frac{\text{Pr}}{2} f \theta_T' = 1 \quad (36)$$

where Pr is the Prandtl number defined as the ratio of momentum and thermal diffusivities:

$$\text{Pr} = \frac{\nu_v}{\alpha_T} \quad (37)$$

Eq. (35) and (36) can be solved numerically with the following converted boundary conditions:

$$u(y=0)=0 \quad f'(\eta=0)=0 \quad (38)$$

$$u(y \rightarrow \infty)=u_\infty \quad f'(\eta \rightarrow \infty)=1 \quad (39)$$

$$v(y=0)=0 \quad f(\eta=0)=0 \quad (40)$$

$$T(y=0)=T_s \quad \theta_T(\eta=0)=0 \quad (41)$$

$$T(y \rightarrow \infty)=T_\infty \quad \theta_T(\eta \rightarrow \infty)=1 \quad (42)$$

Solutions for f , f' , θ_T , and θ'_T can then be used to infer properties of the flow. For instance, f' gives the velocity profile:

$$f'(\eta) = \frac{u}{u_\infty} \quad (43)$$

The boundary layer is then defined as the point where $u = 0.99u_\infty$, which corresponds to $\eta = 5$. Using Eq. (32), boundary layer thickness can be expressed as:

$$\delta = \frac{5x}{\sqrt{\text{Re}_x}} \quad (44)$$

where Reynolds number, Re_x , is defined as [48]:

$$\text{Re}_x = \frac{u_\infty x}{\nu_k} \quad (45)$$

A similar expression for thermal boundary layer is also developed:

$$\delta_T = \delta \text{Pr}^{-1/3} \quad (46)$$

Buoyant Flow.

In the case of buoyant flow, fluid motion is due to density gradients within the fluid and the gravitational body force. These combine to produce what is referred to as free convection flow. One of the most studied problems in free convection flow is the isothermal vertical flat plate in a quiescent environment. As depicted in Figure 5, this problem consists of a vertical flat plate with surface temperatures higher than the environment ($T_s > T_\infty$). The temperature difference produces a thermal gradient, which results in a density gradient with the heated fluid near the surface being forced upward. The velocity distribution is then dictated by the temperature gradient, with

boundary conditions of $u(0) = 0$ due to the wall, and $u(y \rightarrow \infty) = 0$ due to the quiescent fluid.

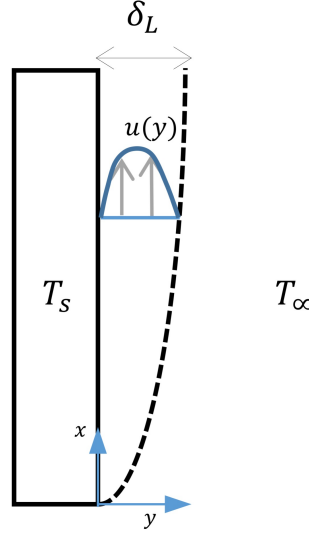


Figure 5. Buoyant flow over isothermal vertical flat plate.

The free convection boundary layer over an isothermal vertical plate has previously been solved by Ostrach using a similarity solution [48, 54]. The conservation equations can be expressed similarly to the flat plate flow case with the addition of buoyancy terms:

$$u \frac{\partial u}{\partial x} + v \frac{\partial u}{\partial y} = g\beta(T - T_\infty) + \nu_k \frac{\partial^2 u}{\partial y^2} \quad (47)$$

$$u \frac{\partial T}{\partial x} + v \frac{\partial T}{\partial y} = \alpha_T \frac{\partial^2 T}{\partial y^2} \quad (48)$$

where g is the gravitational force and β is the volumetric thermal expansion coefficient (ideal gas: $\beta = \frac{1}{T}$). The following are then used to convert u , v , and T using a change

of variables:

$$u = \frac{\partial \psi}{\partial y} \quad (49)$$

$$v = -\frac{\partial \psi}{\partial x} \quad (50)$$

$$\eta = \frac{y}{x} \left(\frac{\text{Gr}_x}{4} \right)^{1/4} \quad (51)$$

$$\psi = f(\eta) \left[4 \nu_v \left(\frac{\text{Gr}_x}{4} \right)^{1/4} \right] \quad (52)$$

$$\theta_T = \frac{T - T_\infty}{T_s - T_\infty} \quad (53)$$

where Gr_x is the Grashof number which measures the ratio of buoyancy to viscous forces [48]:

$$\text{Gr}_x = \frac{g \beta (T_s - T_\infty) x^3}{\nu_v^2} \quad (54)$$

Eq. (47) and (48) can then be written as:

$$f''' + 3f f'' - 2(f')^2 + \theta_T = 0 \quad (55)$$

$$\theta_T'' + 3\text{Pr} f \theta_T' = 0 \quad (56)$$

The boundary conditions are then transformed using the change of variables:

$$u(y=0)=0 \quad f'(\eta=0)=0 \quad (57)$$

$$u(y \rightarrow \infty)=0 \quad f'(\eta \rightarrow \infty)=0 \quad (58)$$

$$v(y=0)=0 \quad f(\eta=0)=0 \quad (59)$$

$$T(y=0)=T_s \quad \theta_T(\eta=0)=1 \quad (60)$$

$$T(y \rightarrow \infty)=T_\infty \quad \theta_T(\eta \rightarrow \infty)=0 \quad (61)$$

This set of ODEs and boundary conditions can then be solved numerically for f and θ_T .

Using these solutions, boundary layer thickness, δ , for free convection flow along a vertical plate can be approximated for $Pr = 0.7$ in terms of Gr as [48]:

$$\delta_x \approx \frac{6x}{(Gr/4)^{1/4}} \quad (62)$$

Boundary layer thickness as a function of surface temperature is shown in Figure 6. Boundary layer thickness can be seen increasing almost linearly with T_s , doubling in thickness from 20 mm at $T_s = 1000$ K to 40 mm $T_s = 3000$ K.

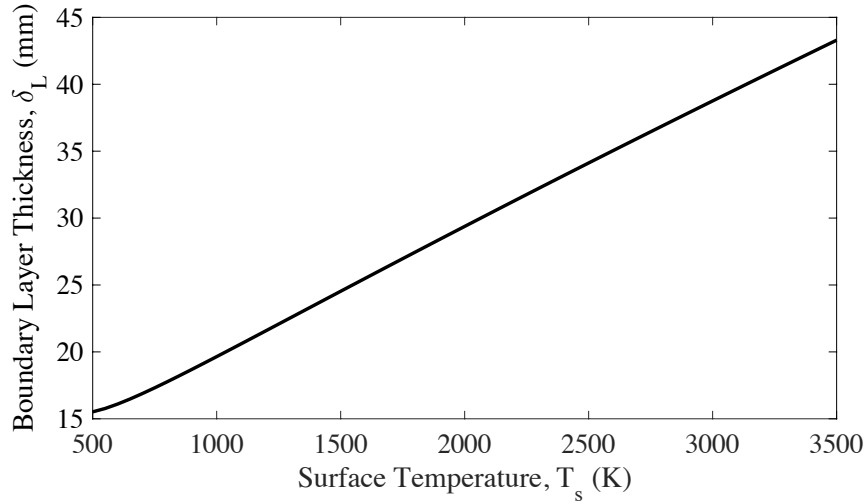


Figure 6. Buoyant flow boundary layer thickness as a function of T_s evaluated at $x = L = 10$ cm.

Stagnation Flow.

The stagnation point flow is another well studied problem. A sketch is provided in Figure 7. The impinging flow creates a small stagnation region near the stagnation point ($u(0,0) = v(0,0) = 0$). Along the surface, a velocity gradient similar to the flat plate shear flow is formed due to the no-slip condition ($u(x,0) = 0$). Solutions for u and v as

a function of location are derived using similarity solutions as with the flat plate shear flow case. Using the following variable substitutions the flow can be described using a set of solvable ODEs [50, 51]:

$$u = \frac{\partial \psi}{\partial y} \quad (63)$$

$$v = -\frac{\partial \psi}{\partial x} \quad (64)$$

$$\eta = y \sqrt{\frac{B}{\nu_v}} \quad (65)$$

$$\psi = x f(\eta) \sqrt{B \nu_v} \quad (66)$$

$$\theta_T = \frac{T - T_s}{T_\infty - T_s} \quad (67)$$

where B is the stagnation velocity gradient, which is generally proportional to u_∞/L where u_∞ is the freestream flow velocity and L is a characteristic length [52]. For a 3D axisymmetric stagnation flow, $B = 3u_\infty/L$. The conservation equations can then be written as:

$$f''' + f f'' + 1 - f'^2 = 0 \quad (68)$$

$$\theta_T'' + \text{Pr} f \theta_T' = 0 \quad (69)$$

with boundary conditions:

$$u(y=0)=0 \quad f'(\eta=0)=0 \quad (70)$$

$$v(y=0)=0 \quad f(\eta=0)=0 \quad (71)$$

$$u(y \rightarrow \infty) = Bx \quad f'(\eta \rightarrow \infty) = 1 \quad (72)$$

$$T(y=0) = T_s \quad \theta_T(\eta=0) = 0 \quad (73)$$

$$T(y \rightarrow \infty) = T_\infty \quad \theta_T(\eta \rightarrow \infty) = 1 \quad (74)$$

The ODEs and boundary conditions can be solved using a numerical boundary value solver.

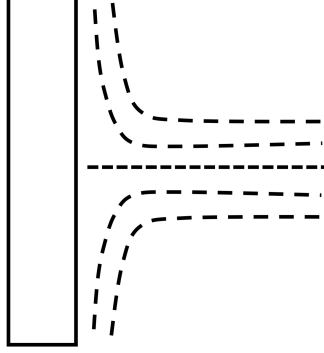


Figure 7. Stagnation flow.

The boundary layer thickness, δ , is defined as the point where velocity is 99% of the freestream value, $u(x, \delta) = 0.99u_{\infty} = 0.99Bx$. Using the numerical solutions, this point occurs at $\eta = 2$, yielding the following boundary layer thickness expression:

$$\delta = 2\sqrt{\frac{\nu_v}{B}} \quad (75)$$

A similar expression can be derived for the thermal boundary layer in terms of the boundary layer [52]:

$$\delta_T = \delta \text{Pr}^{-0.4} \quad (76)$$

which states that thermal boundary layer thickness decreases with increasing Pr.

III. Oxidation Model

This chapter provides detail regarding modeling of the carbon oxidation process. A review of the conservation equations and relevant terms is provided in Section 3.1. Two simplified oxidation models are then presented. The first, presented in Section 3.2, is a 1D diffusion - kinetics model used to evaluate properties normal to the surface. The second, presented in Section 3.3, is a quasi 2D model incorporating diffusion (normal to the surface) and convection (along surface) and is used to evaluate properties along the surface. While both models have significant limitations due to their assumptions, they are useful in gaining intuition about the problem and interpreting experimental observations. Comparison of simulations with experimental data is discussed in Chapter V - VI

3.1 Conservation Equations

The species conservation equation is expressed as:

$$\frac{dC_i}{dt} = \omega_i - v \cdot \nabla C_i + \nabla \cdot D_i \nabla C_i \quad (77)$$

where C_i is the concentration of species i , ω_i is the reaction source term, $v \cdot \nabla C_i$ is the convective transport term with velocity vector v , and $\nabla \cdot D_i \nabla C_i$ is the diffusion transport term with D_i as diffusion coefficient of species i . Similarly the conservation of energy, neglecting diffusion thermal transport, can be expressed as:

$$\frac{d\rho h}{dt} = q - v \cdot \nabla \rho h + \nabla \cdot \alpha_T \nabla \rho h \quad (78)$$

where h is the sensible enthalpy, q is the source term due to the gas phase reactions, ρ is the gas density, and α_T is the thermal resistivity. The enthalpy term can be approximated in terms of specific heat C_p as $h \approx C_p T$.

Assuming steady state and a uniform gas (ρ , c_p and D constant), Eq. (77) and (78) can then be written as:

$$-D \nabla^2 C_i = \omega_i - v \cdot \nabla C_i \quad (79)$$

$$-\lambda \nabla^2 T = q - v \rho c_p \cdot \nabla T \quad (80)$$

where λ is the thermal conductivity ($\lambda = \alpha_T \rho c_p$).

3.2 1D Model

We first consider the 1D case with the reactive surface at $y = 0$. Heterogeneous reactions take place at the surface boundary and homogeneous reactions within the gas ($y > 0$). Flow normal to the surface is neglected ($v_y = 0$). Rewriting Eq. (79) for the 1D case:

$$-D C_i'' = \omega_i \quad (81)$$

where C_i'' refers to the second derivative normal to the surface. The convection term is neglected due to the assumption of zero velocity normal to the surface. Applying this to the three species of interest, and substituting the gas phase rate equation (Eq. (5), $a = 0.2$, $b = 0$), the following species conservation equations are derived:

$$-D O'' = -\frac{1}{2} O^{0.2} F k_g \quad (82)$$

$$-D F'' = -O^{0.2} F k_g \quad (83)$$

$$-D P'' = O^{0.2} F k_g \quad (84)$$

where O , F , and P represent O_2 , CO , and CO_2 concentrations, respectively, and k_g is the gas phase rate coefficient $k_g = A_g \exp(-B_g/T)$. Similarly Eq. (80) can be written as:

$$-\lambda T'' = -(O^{0.2} F k_g) \Delta H_g \quad (85)$$

where ΔH_g is the heat of combustion in J/mol.

Two sets of boundary conditions are set by surface kinetics and freestream conditions. At the flame edge (δ), the freestream conditions are imposed:

$$O(\delta) = [O_2]^o \quad (86)$$

$$F(\delta) = [CO]^o = 0 \quad (87)$$

$$P(\delta) = [CO_2]^o = 0 \quad (88)$$

$$T(\delta) = T_{plume}^o = 300 \text{ K} \quad (89)$$

At the surface, species flux is dictated by surface reactions:

$$O'(0) = -\left(\frac{1}{D}\right)(-R_{s1} - R_{s2}) \quad (90)$$

$$F'(0) = -\left(\frac{1}{D}\right)(2R_{s1} + 2R_{s2}) \quad (91)$$

$$P'(0) = -\left(\frac{1}{D}\right)(-R_{s2} + R_{s3}) \quad (92)$$

where R_{s-i} are the surface rate equations defined as: $R_{s1} = Ok_{s1}$, $R_{s2} = Pk_{s2}$, and $R_{s3} = Ok_{s3}$. The last boundary conditions relates surface and **plume** temperature:

$$T(0) = \begin{cases} T_s & T_s < T^* \\ T^* & T_s \geq T^* \end{cases} \quad (93)$$

which assumes there is an equilibrium between surface and gas temperature adjacent

to the surface until temperature threshold, T^* . T^* is estimated to be 2400 K based on current observations.

A numerical boundary value problem (BVP) solver is used to evaluate the ODEs and boundary conditions given in Eq. (83) - (93) for a given T_s and δ . Key parameters are given in Table 4. Surface reaction rates are based on median literature values. The gas phase rate is based on the work by Soblev[15].

Table 4. Simulation parameters

parameter	value	units
D diffusivity	$4 \cdot 10^{-4}$	m^2/s
λ thermal conductivity	$6.7 \cdot 10^{-2}$	$\text{J}/\text{m}/\text{s}/\text{K}$
ΔH_g (G) heat of reaction	$-5.0 \cdot 10^5$	J/mol
ΔH_{s1} (S1) heat of reaction	$-1.0 \cdot 10^5$	J/mol
ΔH_{s2} (S2) heat of reaction	$2.0 \cdot 10^5$	J/mol
ΔH_{s3} (S3) heat of reaction	$-3.0 \cdot 10^5$	J/mol
A_1^o (S1) pre-exponential	$2.2 \cdot 10^5$	m/s
A_2^o (S2) pre-exponential	$1.1 \cdot 10^4$	m/s
A_3^o (S3) pre-exponential	$1 \cdot 10^3$	m/s
E_1 (S1) activation energy	21,500	K
E_2 (S2) activation energy	23,100	K
E_3 (S3) activation energy	21,500	K
A_g (G) pre-exponential	$1.8 \cdot 10^5$	$(\text{mol}/\text{m}^3)^{-0.2} \text{ 1/s}$
E_g (G) activation energy	13,600	K
T^* T equilibrium threshold	2400	K

A sample solution is shown in Figure 8 for a surface temperature of 2500 K and flame thickness of 5 mm. CO created at the surface diffuses away and is consumed by the gas phase reaction, resulting in negligible population at 3 mm. CO_2 is created by the CO oxidation and diffuses away from the surface until reaching freestream conditions at the flame edge. At the surface, CO_2 production is balanced by the CO_2 consumption through S2, resulting in the flat CO_2 profile. Due to the low CO population and thin

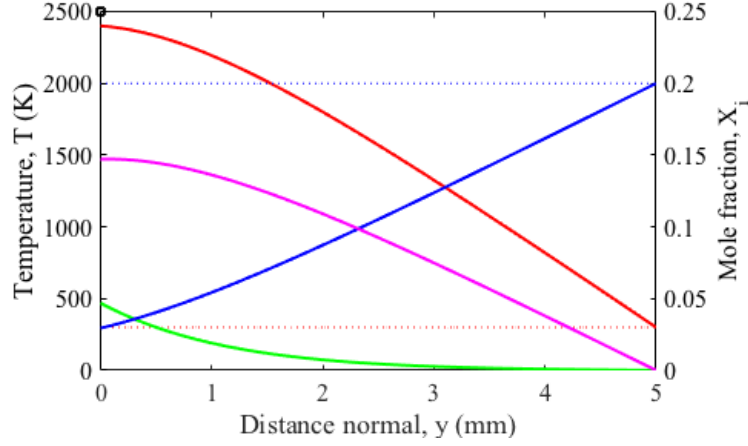


Figure 8. 1D Flame model for $T_s = 2500$ K and $\delta = 5$ mm: (—) X_{CO} , (—) X_{O_2} , (—) X_{CO_2} , (—) X_{O} , (—) T_{plume} , (· ·) T_{plume}^o , (□) T_s

flame, a significant population of O_2 diffuses to the surface. This creates what is referred to as an attached flame, where CO_2 and T_{plume} peak at the surface.

Surface Temperature Sensitivity.

A sensitivity analysis was performed to determine the influence of surface temperature. Simulations were run at $T_s = 2000, 2500$, and 3000 K and $\delta = 5$ and 10 mm. Results are shown in Figure 9. Surface reactivity increases directly with T_s , resulting in an increasing CO at the surface. The higher CO increases the gas phase reaction, which further depletes the O_2 population as it diffuses inward, increasing CO_2 population. Similar trends were noted for the 5 and 10 mm flame width cases, but with less surface O_2 for the thicker flame case due to the longer diffusion length. The transition from attached to detached flame with increasing temperature is marked by the movement of peak T_{plume} away from the surface as surface O_2 becomes depleted with increasing T_s .

Flame Length Sensitivity.

Simulations were performed at flame widths of 3, 6, and 9 mm and surface temperatures of 2000 and 3000 K. Results are displayed in Figure 10. The most evident result of the increased flame thickness is a the depletion of surface O_2 due to the longer reaction region and diffusion length. For the low T_s case, the drop in O_2 is not significant enough to produce a detached flame. The increase in δ also increases CO_2 due to lower diffusion losses. For the high T_s case, the drop in O_2 coupled with the high surface reactivity results in the transition to a detached flame, with CO_2 and T_{plume} peaking away from the surface. It should also be noted that in the detached flame case, there is insufficient O_2 at the surface and that surface oxidation is relying predominantly on CO_2 . The CO_2 consumption at the surface then outweighs the production through S3 and the gas phase oxidation. This can also be seen in the positive slope of the CO_2 profile at the surface, indicating that CO_2 is diffusing toward the surface

Surface Rate Sensitivity.

Given the uncertainty in surface reaction rates, a sensitivity analysis was performed for each surface reaction by varying pre-exponential factor. Nominal pre-exponential factors, A_i^o , are given by Table 4. Reaction S1 is evaluated in Figure 11 for $A_1 = 0.1A_1^o$, A_1^o , and $10A_1^o$. As expected an increase in S1 reactivity results in a decrease in surface O_2 . The increase in reactivity increases CO production, which in turn increases the CO_2 population.

Similar analysis for the S2 reaction is shown in Figure 12 for $A_2 = 0.1A_2^o$, A_2^o , and $10A_2^o$. Higher surface reactivity increases the CO_2 consumption at the surface. Once CO_2 consumption at the surface exceeds production, a detached flame is formed and CO_2 begins diffusing towards the surface, indicated by the positive slope in CO_2 at the surface. The increase in reactivity results in an increase in CO production, which

then increases the gas phase reactivity and lowers O_2 population. Repeated sensitivity analysis for the S3 reaction is shown in Figure 13 for $A_3 = 0$, A_3^o , and $100A_3^o$. Results suggest little sensitivity to S3 reaction, with changes in species mole fractions of less than 0.01 between $A_3 = 0$ and $A_3 = 100A_3^o$.

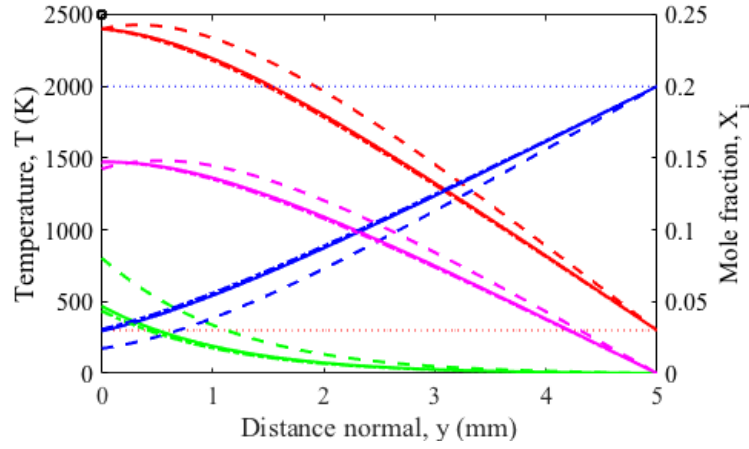


Figure 12. A_2 sensitivity of 1D Flame model with $T_s = 2500$ K and $\delta = 5$ mm. A_2 : (-) $A_2 = 0.1 \times A_2^0$, (-) $A_2 = A_2^0$, (- -) $A_2 = 10 \times A_2^0$. (-) X_{CO} , (-) X_{O_2} , (-) X_{CO_2} , (·) $X_{O_2}^0$, (-) T_{plume} , (·) T_{plume}^0 , (□) T_s

3.3 Quasi 2D Model

A quasi 2D model was developed to incorporate both diffusion normal to the surface and convection parallel to the surface. Consider a small control volume of width Δy adjacent to the surface. We apply Eq. (79) assuming zero velocity normal to the surface, $v = (v_x, 0)$:

$$\left(\frac{dC_i}{dt}\right)_s = \omega_i - ((v_x, 0) \cdot \nabla C_i) - \nabla \cdot D \nabla C_i \quad (94)$$

Assuming concentration gradients normal to the surface are much stronger than along the surface, $\frac{dC_i}{dy} \gg \frac{dC_i}{dx}$, the diffusion term is reduced to only the dy terms:

$$\left(\frac{dC_i}{dt} \right)_s = \omega_i + v_x \frac{dC_i}{dx} - \frac{d}{dy} \left(D \frac{dC_i}{dy} \right) \quad (95)$$

To reduce complexity, Eq. (95) is converted to an ODE by approximating the diffusion term and removing the y dependence. First we expand diffusion term into the two flux terms:

$$\frac{d}{dy} \left(D \frac{dC_i}{dy} \right) = \frac{1}{\Delta y} \left(-D \frac{dC_i}{dy} \Big|_{y=\Delta y} - D \frac{dC_i}{dy} \Big|_{y=0} \right) \quad (96)$$

where Δy is the width of the control volume. The diffusion flux term on the left is approximated using:

$$D \frac{dC_i}{dy} \Big|_{y=\Delta y} = \frac{D}{\delta_d} (C_i - C_i^o) \quad (97)$$

where δ_d is a diffusion length scale. The diffusion flux at the surface is determined surface reactions:

$$D \frac{dC_i}{dy} \Big|_{y=0} = \omega_{s-i} \quad (98)$$

where ω_{s-i} is the surface production rate of species i . Substituting these into Eq. (95) and assuming steady state, we get the following expression:

$$\omega_i = v_x \frac{dC_i}{dx} + \frac{1}{\Delta y} \left(\frac{D}{\delta_d} (C_i - C_i^o) - \omega_{s-i} \right) \quad (99)$$

which relates the volumetric production to the convective, diffusion, and surface flux terms. The boundary conditions for the first order ODE are then set by the upstream conditions:

$$C_i(x=0) = C_i^o \quad (100)$$

Applying Eq. (99) and (100) to CO , CO_2 , and O_2 we derive a system of 3 coupled

ODEs and boundary conditions. Given surface and plume temperature profile inputs to infer kinetic rates, the system can be solved numerically. A sensitivity analysis is performed to determine the influence of T_s and flow rate. Key parameters used are those given in Table 4.

Surface Temperature Sensitivity.

The simulation assumes a Gaussian T_s profile with width 10 cm and peaks of 2000, 2500, and 3000 K. The Gaussian plume temperature profile was fixed with a peak of 2200 K and half width 20 cm. Freestream velocity was fixed at 7 m/s. Diffusion length is assumed be equal to boundary layer thickness, $\delta_d = \delta$ (7 m/s). The resulting solutions to the quasi 2D model with varying T_s are given in Figure 14. Surface reactivity increases with surface temperature, resulting in an increase in CO due to S1 and S2. A dip in CO_2 at laser center forms as the CO_2 depletion through S2 overpowers gas phase production.

Flow Sensitivity.

Similar analysis was preformed for freestream flow conditions of 5, 7, and 10 m/s to determine the role of convective transport. Temperature profiles were fixed with peak T_s and T_{plume} of 3300 K and 2200 K, respectively, and half widths of 10 and 20 cm, respectively. Diffusion length scale was assumed to scale with boundary layer thickness, $\delta_d = \delta \propto v_\infty^{-1/2}$.

Simulation results are shown in Figure 15. The sensitivity to flow conditions can be attributed to both diffusion and convection transport effects. The increase in freestream flow conditions results in a decrease in boundary layer thickness, which decreases the diffusion length scale. The CO population is then reduced due to higher diffusion losses. Less CO_2 is then produced due to the decrease in CO population. The convection transport effects can be seen in the slight downstream shift of CO and CO_2 .

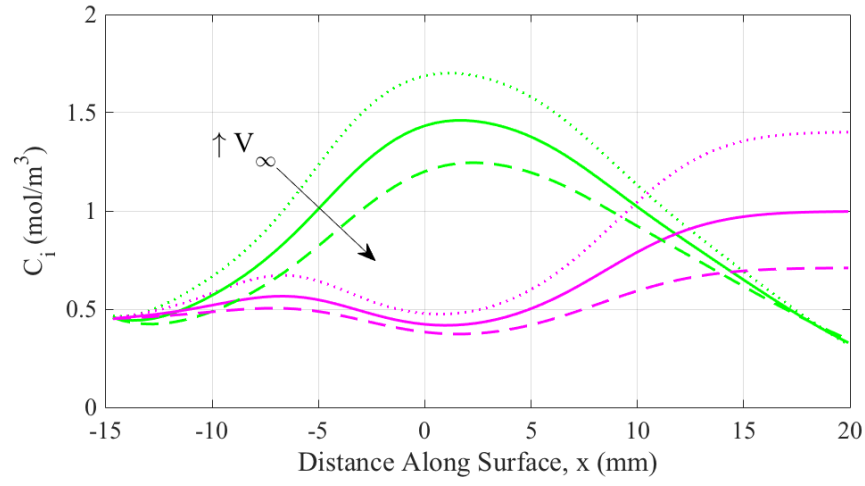
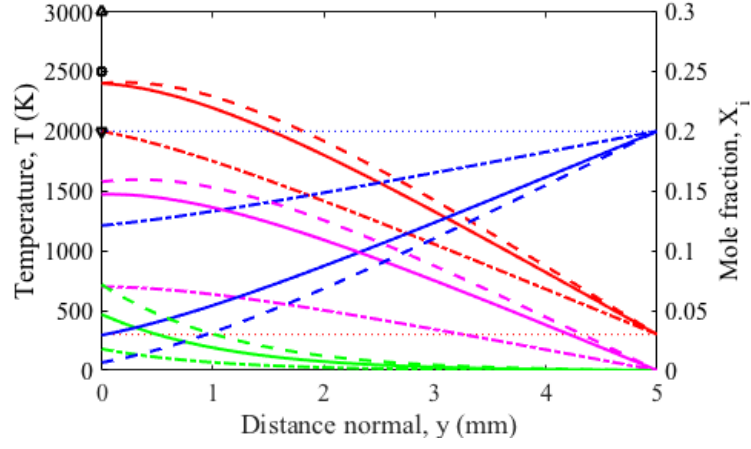
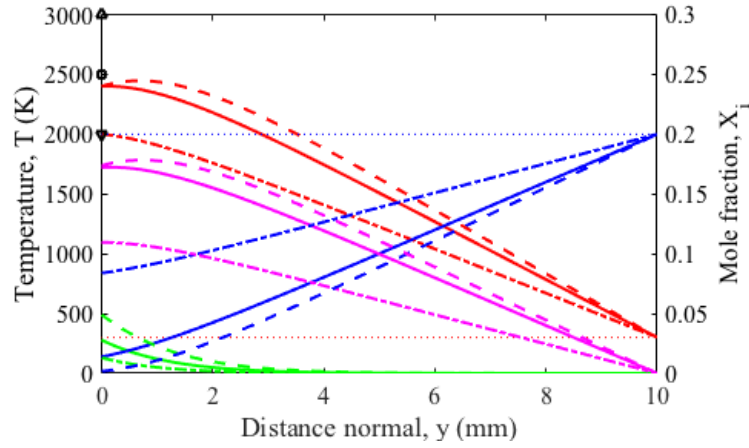


Figure 15. Simulated (—) CO and (—) CO₂ profiles for varying V_∞ : (..) 5 m/s, (—) 7 m/s, and (- -) 10 m/s.

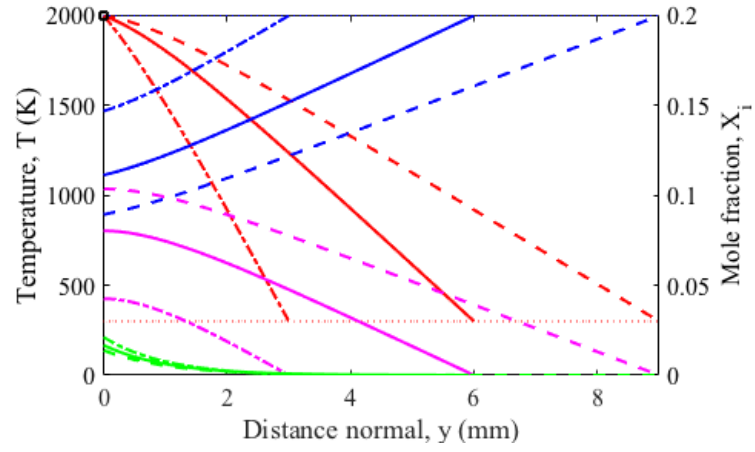


(a) $\delta = 5$ mm

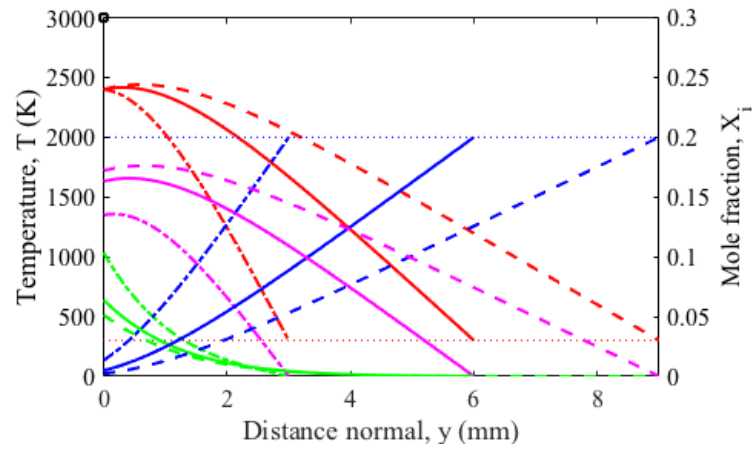


200
(b)
 $\delta =$
10
mm

Figure 9. 1D Flame model for varying T_s at $\delta = 5$ and 10 mm: (-.) $T_s = 2000$ K, (-) $T_s = 2500$ K, (- -) $T_s = 3000$ K. (-) X_{CO} , (-) X_{O_2} , (-) X_{CO_2} , (.) $X_{O_2}^o$, (-) T_{plume} , (.) T_{plume}^o , (∇ , \square , Δ) T_s



(a) $T_s = 2000$ K



(b) $T_s = 3000$ K

Figure 10. 1D Flame model for varying δ at $T_s = 2000$ and 3000 K: (-.) $\delta = 3$ mm, (-) $\delta = 6$ mm, (- -) $\delta = 9$ mm. (—) X_{CO} , (—) X_{O_2} , (—) X_{CO_2} , (· ·) $X_{O_2}^o$, (—) T_{plume} , (· ·) T_{plume}^o , (□) T_s

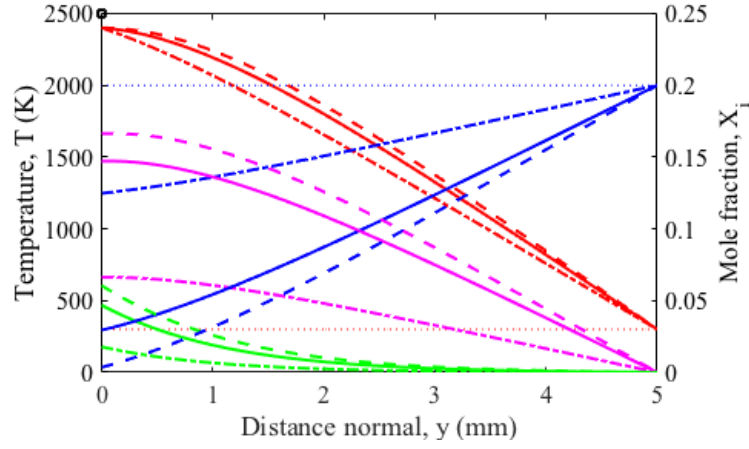


Figure 11. A_1 sensitivity of 1D Flame model with $T_s = 2500$ K and $\delta = 5$ mm. A_1 : (-) $A_1 = 0.1x A_1^o$, (-) $A_1 = A_1^o$, (-) $A_1 = 10x A_1^o$. (-) X_{CO} , (-) X_{O_2} , (-) X_{CO_2} , (-) $X_{O_2}^o$, (-) T_{plume} , (-) T_{plume}^o , (\square) T_s

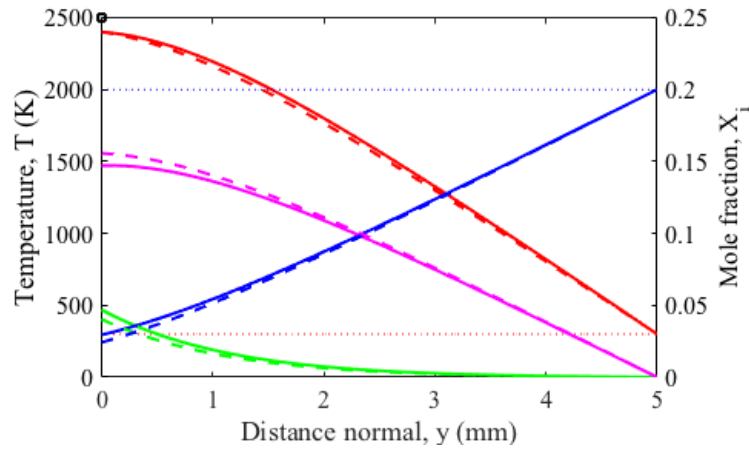


Figure 13. A_3 sensitivity of 1D Flame model with $T_s = 2500$ K and $\delta = 5$ mm. A_3 : (-) $A_3 = 0$, (-) $A_3 = A_3^o$, (-) $A_3 = 100x A_3^o$. (-) X_{CO} , (-) X_{O_2} , (-) X_{CO_2} , (-) $X_{O_2}^o$, (-) T_{plume} , (-) T_{plume}^o , (\square) T_s

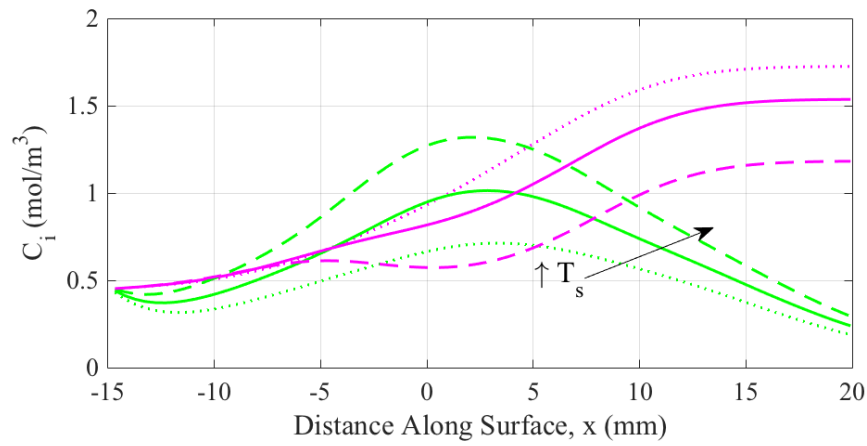


Figure 14. Simulated (—) CO and (—) CO_2 profiles for varying T_s profiles. T_s are Gaussian ($\sigma = 10$ cm) with peak temperatures of: (..) 2000K, (—) 2500 K, and (- -) 3000 K.

IV. Experimental Methods

Chapter IV provides detail regarding the experimental procedures and post processing techniques used in Chapter V - VII. Samples were tested at the Laser Hardened Materials Laboratory (LHMEL) at Wright Patterson Air Force Base. A short summary of the LHMEL laser system and beam diagnostics is given in Section 4.1. A description of the three graphite materials is included in Section 4.2. A variety of MWIR and visible diagnostics were used to monitor the gas and surface properties. Instrumentation details, operating conditions, and post processing techniques are discussed in Section 4.3. Samples were tested at three flow configurations: buoyant flow, flat plate shear flow, and stagnation flow. A description of each test configuration is given in Section 4.4.

4.1 Laser System and Diagnostics

Samples were irradiated using a 15 kW ytterbium fiber laser at $1.07 \mu\text{m}$. Laser power was characterized in two phases [55]. Prior to testing, a ballistic calorimeter was used to measure the total power output. During testing, a small fraction of the beam is routed to a transient calorimeter to measure power over the testing period. Spatial characterization of the beam profile is completed using a small picked off portion of the beam incident on a diffuse reflector and imaged using a high speed camera. The irradiance is then determined based on calorimeter power measurements and the imaged beam profile. Average irradiance over the beam profile is then determined by:

$$I_{ave} = P/d_b \quad (101)$$

where P is the total power, and d_b is the average beam diameter, defined as containing 86% of the beam power and determined using the beam profile images. A detailed description of the LHMEL test facility and its capabilities can be found in [55–57].

4.2 Graphite Materials

Three graphite materials were evaluated to determine the influence of graphite material on oxidation rate. All samples were produced by Graphtek LCC and purchased through the Graphite Store [3]. A summary of the materials is provided in Table 5. Fine and isomolded graphite materials are produced using the traditional methods outlined in Section 2.2, resulting in a porous material. Previous impurity analysis of laser irradiated fine porosity graphite report trace amounts of Si, S, Fe, Ca, Al, and K [58]. Pyrolytic graphite is formed in a chemical vapor deposition (CVD) method which creates high purity samples with near zero porosity surfaces. The layering process creates a highly anisotropic material, with high conductivity within the layer and low conductivity across layers.

Table 5. Graphite materials [3]

Material	ID	Fabrication Process	Density (g/cm ³)	Particle Size (μm)	Thermal Conductivity (W/m/K)	Ash (%)
fine	GR008G	extruded	1.76	203	130	0.06
isomolded	GM-10	isostatic press	1.82	10.2	83	0.05
pyrolytic	PG-SN	layering	2.2	NA	$k_{ }$: 400 k_{\perp} : 3.5	-

4.3 Diagnostics

Thermal Imagery.

Surface temperatures were measured using the FLIR SC6000 thermal camera. The SC6000 is capable of interweaving multiple integration times in a single test acquisition, allowing for a wider detection range. The focal plane array (FPA) is a 640 by 512 InSb,

sensitive from 1.5 - 5 μm , but is filtered using a 3.8-4.0 μm band pass filter to avoid CO_2 and H_2O emission regions. Neutral density (ND) filters are used to avoid detector saturation, and are chosen based on scene radiance and integration times. A 2.0 ND filter was used for all current measurements. Additional detail regarding the FLIR thermal camera can be found in [59].

The measured signal on the detector can then be expressed as:

$$Y = G[L + L_o]t_{int} \quad (102)$$

where Y is the measured signal (counts), G is the gain of the instrument and reflects the spectral response of optics and FPA, and t_{int} is the integration time. The radiance is divided between two terms, the scene radiance, L , and any additional thermal radiance introduced by the camera, L_o . Because the instrument uses multiple integration times, it useful to normalize by t_{int} and convert to signal flux, $S = Y/t_{int}$ (counts/s), which can be expressed as:

$$S = GL + O \quad (103)$$

where the offset, O (counts/s), incorporates the flux due to thermal radiation within the camera as well as any additional noise. Radiance is determined using the known relationship between temperature and emitted radiation,

$$L(\lambda, T) = \epsilon B(\lambda, T) \quad (104)$$

where L ($\text{W}/\text{cm}^2/\mu\text{m}$) is the measured radiance as a function temperature T and wavelength λ , ϵ is the emissivity of the material, and B is blackbody radiance as given by Planck's law:

$$B(\lambda, T) = \frac{2\pi h c^2}{\lambda^5 (\exp(\frac{hc}{\lambda k_B T}) - 1)} \quad (105)$$

where k_B is the Boltzmann constant, h is the Planck constant, and c is the speed of light. The signal flux can then be expressed as:

$$S = G[\epsilon B(\lambda_F, T)] + O \quad (106)$$

λ_F is the filtered FLIR wavelength, $\lambda_F = 3.9 \mu\text{m}$.

G and O values are determined by measuring the signal flux of a wide area blackbody, expressed as:

$$S = G[\epsilon_{BB} B(\lambda_F, T_{BB})] + O \quad (107)$$

where ϵ_{BB} is the emissivity of the blackbody, typically >0.96 , and $B(\lambda_F, T_{BB})$ is the blackbody radiance. Calibration is done in two phases. Prior to testing, blackbody measurements are taken at surface temperatures of 300 - 870 K (blackbody limit) and integration times of 0.01 - 2 ms to determine gain and offset. During testing, an additional calibration is done to determine any change in O , which is highly sensitive to changes in ambient room temperature.

Post processing of thermal imagery consisted of three steps. First a non-linearity correction is applied to account for the non-linear response at low signal. The signal is then converted to a measured radiance using Eq. (103) and the determined gain and offset. Lastly, surface temperature is computed using Eq. (104) and the inferred radiance. In the case of multiple integration time data, this produces four temperature maps, each providing a limited temperature region based on the noise floor and saturation limit. Shortest integration times were chosen to avoid saturation while still capturing peak surface temperatures. The remaining integration times were increased to capture a range of lower surface temperatures, ideally with the longest capturing room temperature. The four temperature maps are then averaged together, neglecting low signal or saturated pixels, to maximize detectable temperature range.

A sample data set is shown in Figure 16. The longest integration time, $t_{1-int} = 1.5$ ms, was chosen slightly too high, and failed to capture room temperature, with a noise floor of 400 K. The shortest integration time, $t_{1-int} = 0.06$ ms, was chosen to allow characterization of high surface temperatures within the beam ($T_s > 3000$ K). The final temperature map is then shown in Figure 17. The detectable temperature range in final temperature map (400 - 3000 K) shows the benefit of multiple integration times.

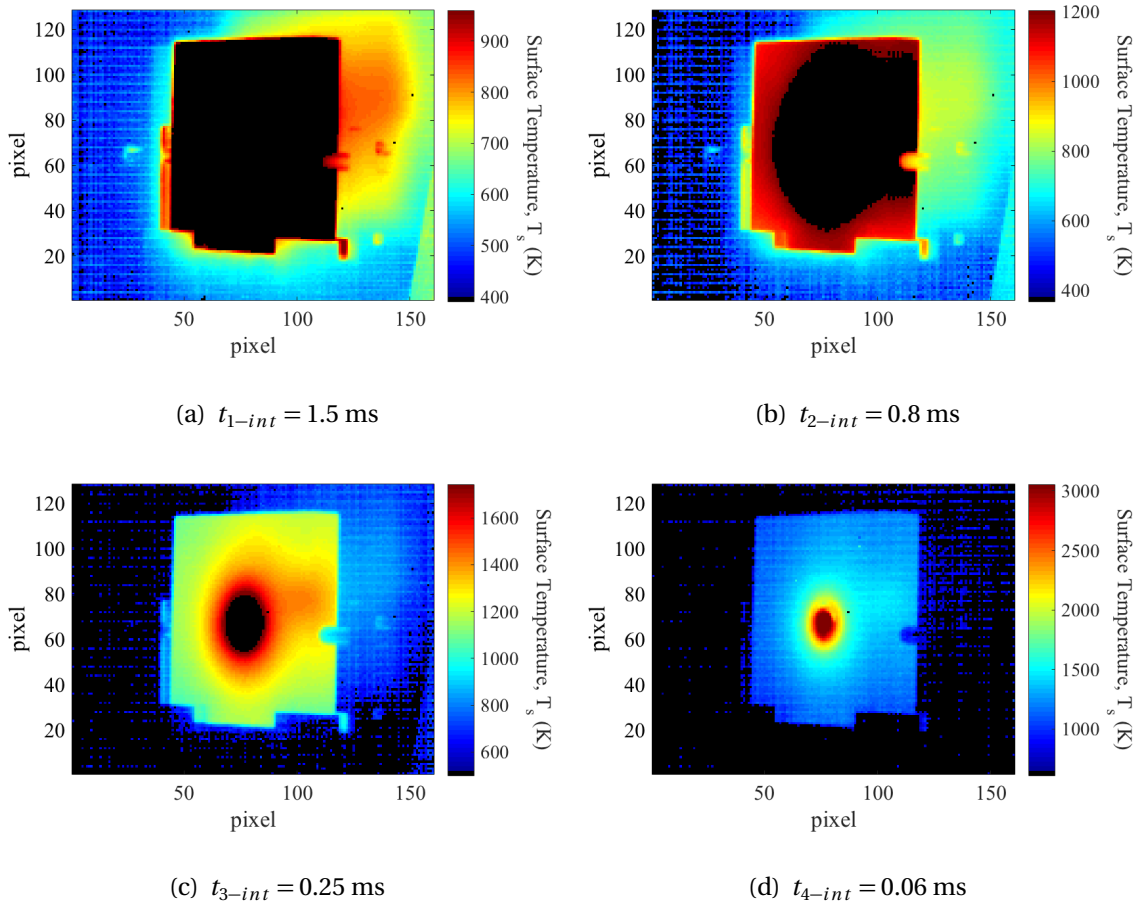


Figure 16. Sample FLIR temperature data using multiple integration times of 0.06, 0.25, 0.8, and 1.5 ms. Masked pixels (black) are outside the calibration region for that integration time setting.

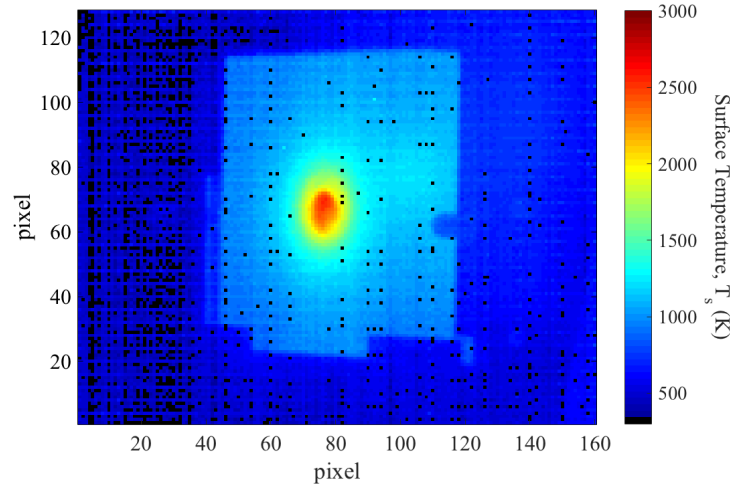


Figure 17. Sample FLIR temperature data integrating multiple integration times of 0.06, 0.25, 0.8, and 1.5 ms. Masked pixels (black) are outside the calibration region for that integration time setting.

The largest source of error in this temperature measurement technique is choice of material emissivity. To reduce this error, the emissivities of the undamaged and irradiated graphite materials were evaluated at $3.9\ \mu\text{m}$ using a Surface Optics Corp. SOC-100 Hemispherical Directional Reflectometer [60]. Samples are illuminated using a calibrated blackbody source. Reflectance, ρ , is collected at all angles using a hemispherical mirror and focused onto a FTIR spectrometer. Emissivity is then calculated assuming equilibrium, $\varepsilon = 1 - \rho$. Samples were evaluated from room temperature to the instrument limit of 500°C at wavelengths of $2\text{--}25\ \mu\text{m}$. The temperature limit of the SOC prevents emissivity measurements at comparable temperature conditions. However, for most graphite materials, emissivity is independent of temperature [2]. Therefore, emissivities of irradiated samples at 500°C will be used to process thermal imagery. The limits of this assumption are discussed in Chapter V.

Temperature uncertainties are estimated based on propagated emissivity uncer-

tainty ($\Delta\epsilon$). Temperature errors (ΔT) are calculated using the following expression:

$$\epsilon B(T) = (\epsilon + \Delta\epsilon)B(T + \Delta T) \quad (108)$$

Evaluation of Eq. (108) for varying emissivity ($\epsilon = 0.6, 0.8$, and 1.0), surface temperature ($T_s = 1000 - 3500$ K), and emissivity uncertainty ($\epsilon = 0.01 - 0.15$) is shown in Figure 18. As expected, temperature uncertainty increases with surface temperature and emissivity uncertainty. An increase temperature uncertainty is also seen with decreasing emissivity. This results in high temperature uncertainties for low emissivity materials at high temperature. For example, comparing the temperature uncertainty for samples with $\epsilon = 0.6$ and 1.0 evaluated at $T_s = 3500$ K with an emissivity uncertainty $\Delta\epsilon = 0.15$, this leads to T_s uncertainties of 710 and 380 K for $\epsilon = 0.6$ and 1.0 , respectively.

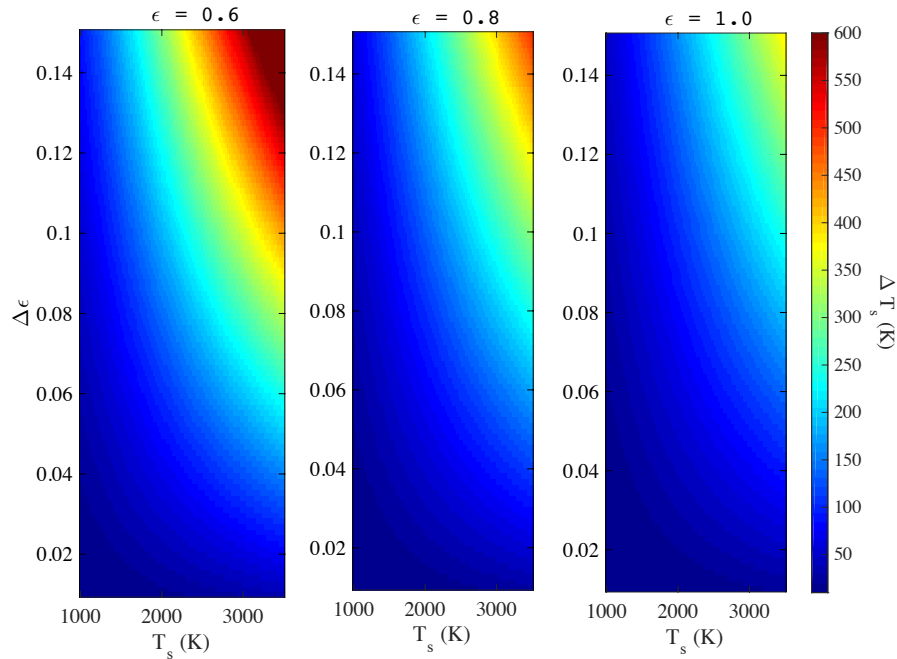


Figure 18. Temperature error (ΔT) calculated for varying emissivity ($\epsilon=0.6$ (left), 0.8 (center), and 1.0 (right), surface temperature ($T_s = 1000 - 3500$ K), and emissivity error $\Delta\epsilon = 0.01 - 0.15$ using Eq. (108).

Imaging Fourier Imaging Spectrometer.

The combustion plume was characterized using the Telops MWIR hyperspectral imager. The MWIR Telops is an imaging Fourier Transform spectrometer (IFTS) which provides spectral content at each pixel in a 320 by 256 InSb focal plane array (FPA). The IFTS is responsive from 1800-6667 cm^{-1} ($\lambda = 1.5 - 5.5 \mu\text{m}$) with a variable spectral resolution of $\Delta \nu = 0.25 - 16 \text{ cm}^{-1}$. Data rates vary with window size, with typical data rates on the order of 1 Hz. Spatial resolution varies with standoff distance, with typical values of 0.4-0.5 mm/pixel for the three flow configurations. Further detail regarding the design and performance of the IFTS can be found in references [1, 7, 61, 62].

Instrument response is characterized using a two point calibration method [62]. Gain, G , and offset, O , are determined by measuring a wide area blackbody at two temperatures. Blackbody temperatures are chosen to cover the dynamic range of the instrument. The measured signals (Y_1, Y_2) can be expressed using Eq. (21):

$$Y_1(\nu) = G(\nu)(B(\nu, T_1) + O(\nu)) \quad (109)$$

$$Y_2(\nu) = G(\nu)(B(\nu, T_2) + O(\nu)) \quad (110)$$

where $B(\nu, T_i)$ is the blackbody spectral radiance at temperature T_i . Gain and offset are then calculated at each pixel in the FPA by solving Eq. (109) - (110) using measured Y_1 and Y_2 values.

Post processing of IFTS data was completed in three steps. First, data was temporally averaged to improve signal to noise ratio. A fast Fourier transform is then used to convert the measured interferogram to wavenumber space, $Y(\nu)$. Next, Eq. (21) is used to convert $Y(\nu)$ to a calibrated radiance, $L(\nu)$. Sample IFTS data is shown in Figure 19. The broadband image on the left highlights limited calibration of the instrument. Integration times are chosen to allow the high temperature plume to fall within the

detectable limits. Pixels which contain the high temperature surface are often saturated. Pixels at the outer edge of the flame begin to fall below the noise limit of the detector ($L_{noise} \approx 5 \mu\text{W}/\text{cm}^2/\text{sr}/\text{cm}^{-1}$). The spectral radiance shown on the right corresponds to the highlighted pixels in the broadband image. CO and CO_2 features are visible in the $1900\text{--}2150 \text{ cm}^{-1}$ and $2100\text{--}2400 \text{ cm}^{-1}$ regions, respectively. Absorption due to atmospheric CO_2 can be seen within the CO_2 structure at 2350 cm^{-1} .

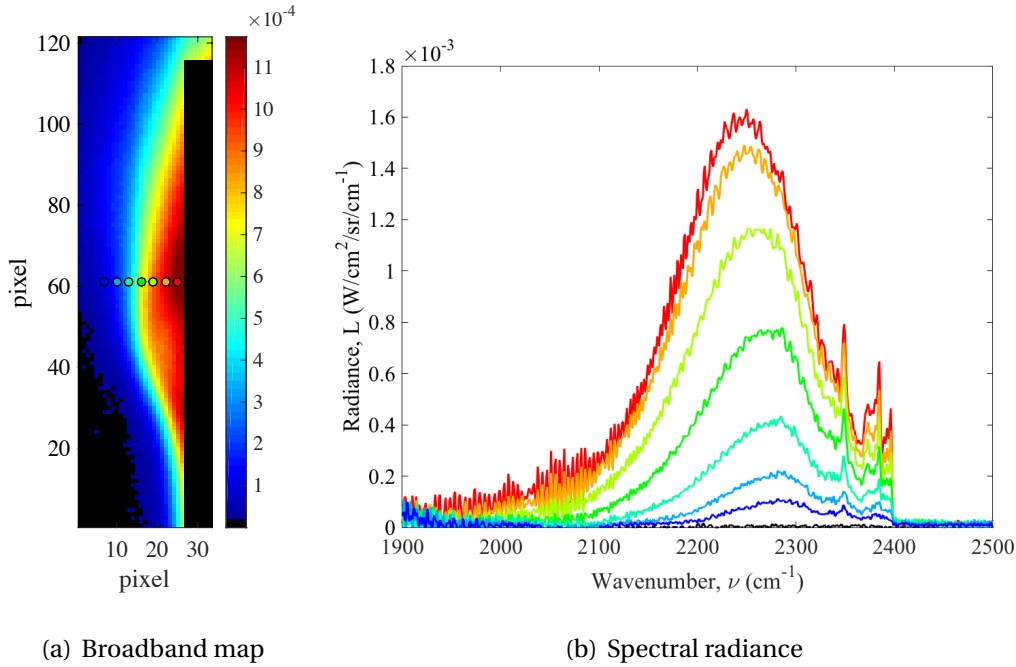


Figure 19. Sample Telops IFTS data. Left: Broadband map evaluated at 2300 cm^{-1} . Masked pixels (black) are outside the calibration region. Right: Spectral radiance at select pixels. Colors correspond to highlighted pixels in the broadband map. Black indicates noise floor

A two layer radiative transfer model (RTM), based on Eq. (27), is then used to infer T_{plume} , X_{CO} , and X_{CO_2} from the spectral signatures [1, 61]. The two layer model assumes the scene radiance can be expressed in terms of a uniform plume and atmosphere as:

$$L_{sc} = \tau_{atmos} \cdot [\epsilon_{plume}(n, X_{i-plume}, T_{plume}, \ell_f) \cdot B(T_{plume})] \quad (111)$$

The measured radiance is then a convolution of the scene radiance and the instrument line shape:

$$L_{det}(\nu) = \int L_{sc}(\nu) \text{ILS}(\nu - \nu') d\nu' \quad (112)$$

where ILS is the instrument lineshape defined for Michelson interferometers as [44]:

$$\text{ILS}(\nu) = 2x_{max} \text{sinc}(2\pi x_{max} \nu) \quad (113)$$

where x_{max} is the maximum OPD. Cross-section data is taken from HITRAN (CO , H_2O) and CDSD 4000 (CO_2) databases [46, 47]. The CDSD 4000 has been reported to provide much better agreement with reported CO_2 signatures above 2000 K [1, 63]. Flame length is assumed to be constant across the entire flame, $\ell_f = 2$ cm. A discussion of the error introduced by this assumption is included in Appendix B.

Plume properties (T_{plume} , X_{CO} , and X_{CO_2}) are then inferred using a nonlinear least squares fit of Eq. (111)-(112) to the measured spectrum. A Planckian baseline was added to account for additional blackbody radiation from soot particles or blurring from neighboring high radiance surface pixels. A sample measurement and fit is shown at the top of Figure 20. Model fits correspond to $T_{plume} = 2240 \pm 40$ K, $X_{\text{CO}_2} = 0.112 \pm 0.004$, $X_{\text{CO}} = 0.26 \pm 0.03$. Quoted uncertainties are based on the 95% confidence interval for the fit and do not include systematic errors. The dip in radiance from 2300-2400 cm^{-1} is due to the absorbance of atmospheric CO_2 , as shown by the path transmissivity in the center panel. The hot CO and CO_2 features are highlighted by the species emissivities given in the bottom panel. Their respective features can also be seen in the spectral radiance at 2000-2200 cm^{-1} and 2100-2400 cm^{-1} ranges for CO and CO_2 , respectively.

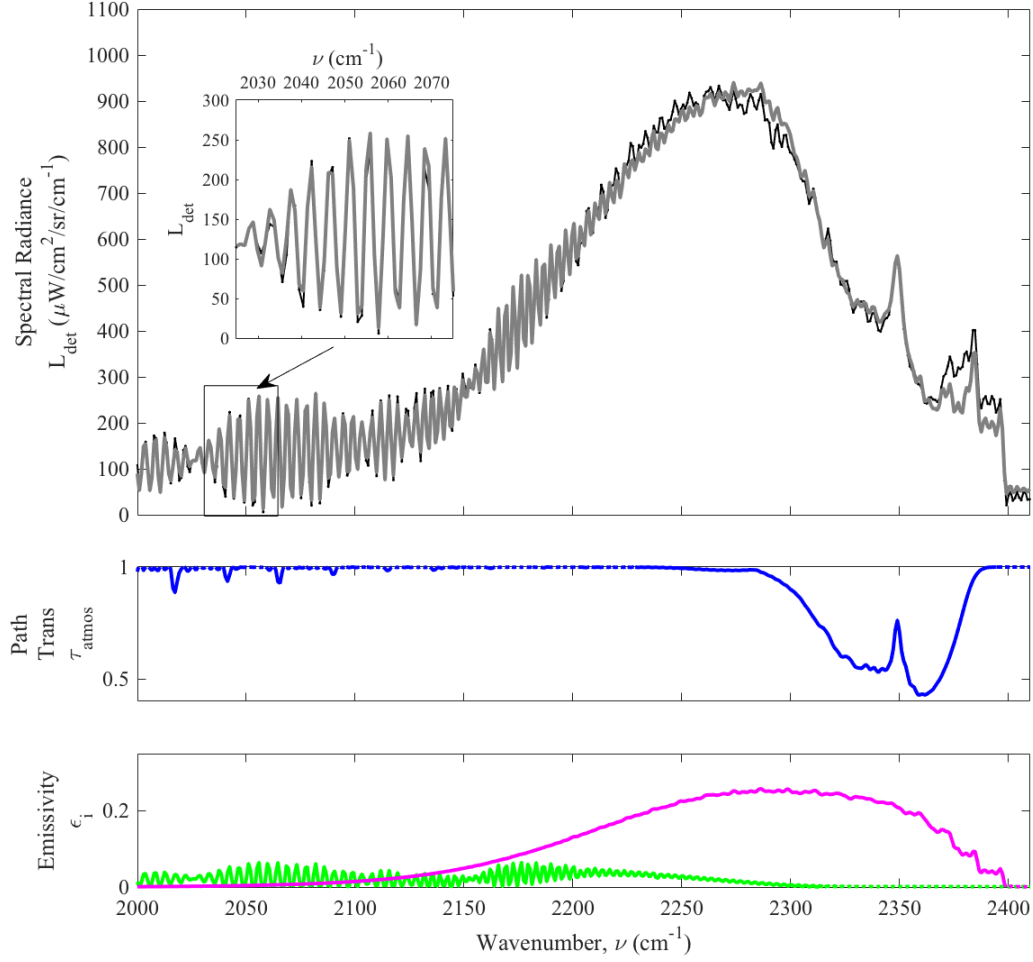
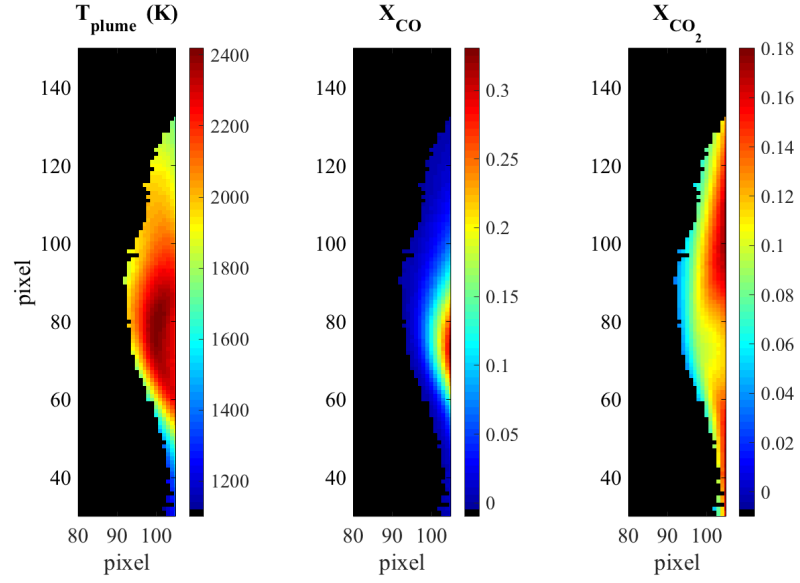


Figure 20. Sample measured spectra and model. (---) measured radiance, L_{det} ; (—) modeled radiance; (—) path transmission, τ_{atmos} ; (—) CO emissivity, ϵ_{CO} ; (—) CO_2 emissivity, ϵ_{CO_2} . Model fits correspond to $T_{plume} = 2240 \pm 40$ K, $X_{CO_2} = 0.112 \pm 0.004$, $X_{CO} = 0.26 \pm 0.03$

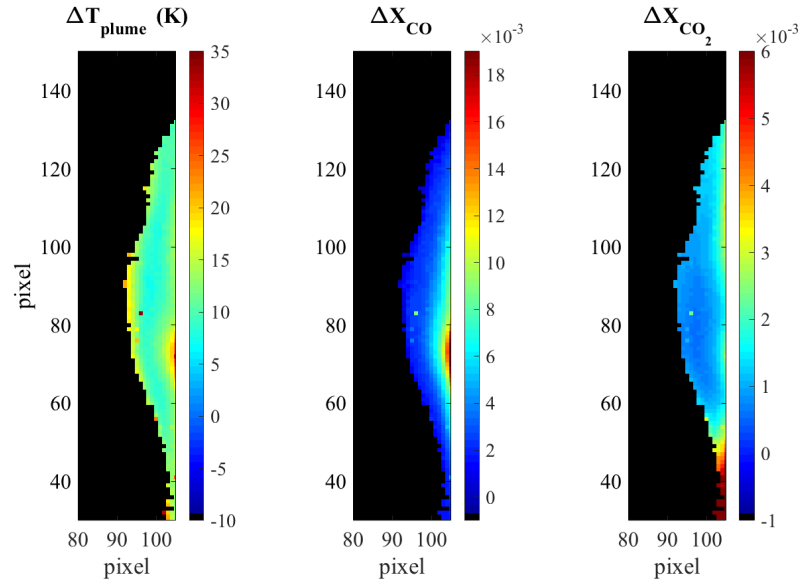
Full 2D spatial maps of species concentration and plume temperature are then inferred by fitting spectra at each pixel. Sample species and temperature maps as well as **uncertainty maps** are given in Figure 21. Masked values (black) represent pixels without fits due to inadequate signal. Uncertainties are based on the 95% confidence bounds of the fit and do not include systematic error. In general, plume temperature errors $< 2\%$ for $T_{plume} = 1800 - 2500$ K and species mole fraction uncertainties of $< 10\%$

for $X_i > 0.1$ are observed. Some fit issues arise in areas of the plume with little CO , leading to higher uncertainties in temperature fits, as seen by the higher temperature uncertainties at flame edge.

Two possible additional sources of error are line of sight averaging and pixel blurring. Error estimates for line of sight averaging are provided in Appendix B. Results suggest systematic errors of $< 12\%$ for species mole fraction and $< 10\%$ for plume temperature. To quantify the severity of the blurring, measurements of the edge spread function (ESF) were taken using a knife edge and blackbody. At focus, pixel blurring is minimal with less than 5% of radiant energy being deposited in neighboring pixels. The most severe blurring is expected at the sample surface, where the hot sample edge is 3.8 cm off focus, causing a 10 % deposit of signature into the neighboring pixels. In some cases this may result in falsely identifying the sample surface. Further detail regarding the MW Telops and its use as a combustion diagnostic can be found in [7, 61, 62, 64].



(a) Species and temperature maps



(b) Uncertainty maps

Figure 21. Sample species and temperature maps (top) and uncertainty (bottom) based on 95% fit confidence. Masked values (black) represent areas with no plume data.

Visible Imagery.

Several visible cameras were used to monitor the test facility and sample during testing. LHMEEL witness cameras were time synchronized with laser control system, allowing for accurate determination of time to ignition. High speed imagery (300 frames/s) of the combustion plume was taken using the Phantom v7 visible high speed camera. High speed imagery was used to visualize flow patterns and estimate the flow velocity through particulate tracking.

4.4 Flow Variations

Measurements were taken under three flow conditions: buoyant flow, flat plate shear flow, and stagnation flow. A description of each of test configuration is discussed below.

Buoyant Flow.

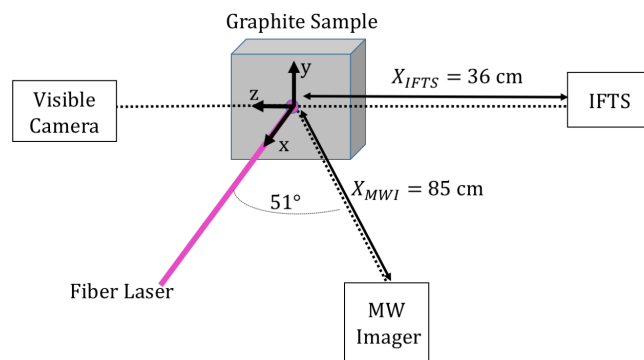
In the buoyant configuration, samples were irradiated in an open air environment, creating a buoyant flame. Three graphite materials (fine, isomolded, and pyrolytic) were evaluated at two irradiances (1000, 3600 W/cm²) for 180 s to produce steady state temperatures of up to 3100 K. Buoyant flow configuration is shown in Figure 22. Samples were mounted perpendicular to the beam in an open air environment (20% O₂, < 1% H₂O). Surface temperatures are observed using the MWIR thermal imager mounted 51 degrees from normal. The resulting buoyant flame is observed along the *z* axis using the MW IFTS and visible high speed camera. Species and temperature maps are produced from temporally averaged steady state IFTS data, from 100 - 150 s, to improve SNR.

Flat Plate Shear Flow.

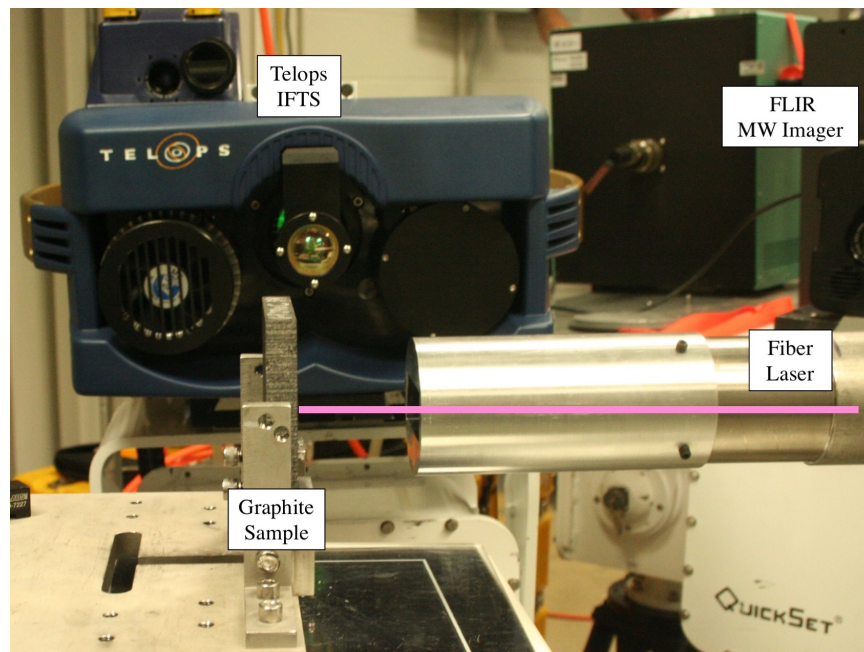
In the flat plate shear flow configuration, samples were irradiated while in a flat plate shear flow, as shown in Figure 23. Three graphite materials (fine, isomolded, and pyrolytic) were evaluated three flow speeds (5, 7, and 10 m/s) and two irradiances (750, 1500 W/cm²) for 120 s to produce steady state temperatures of up to 3000 K. Samples were mounted in a small wind tunnel, flush with the test section floor, 15 cm downstream of the established flow. The test section was equipped with side and top optical access to allow for thermal imagery of the surface and side imaging of the plume. Dry air (20% O₂, < 1% H₂O) was used to establish flows of 5, 7, and 10 m/s. Reynolds number for the 10 m/s case is well below turbulent thresholds ($Re_{turb} \approx 10^5$), for both for reacting and non-reacting flow estimates: non-reacting: $Re(300\text{ K}, 10\text{ m/s}) = 7 \cdot 10^4$, reacting: $Re(2000\text{ K}, 10\text{ m/s}) = 3 \cdot 10^3$. Expansion to higher speed laminar flow was limited by boundary layer thickness and the spatial resolution of the IFTS (0.5 mm/pixel). Species and temperature maps are produced from temporally averaged steady state IFTS data, from 80 - 100 s, to improve SNR.

Stagnation Flow.

The stagnation flow configuration is depicted in Figure 24. Stagnation flow was established using a 2.5 cm diameter nozzle, designed to produce a flat top exit flow. A 1.5 m/s dry air (< 2% H₂O) flow was established over the 6 in diameter cone test samples, creating a 3D stagnation flow with stagnation velocity gradient, $B = 3v_{\infty}/d = 30\text{ s}^{-1}$ (v_{∞} - flow velocity, d - sample diameter). Fine porosity samples were irradiated at 660 and 900 W/cm² until reaching surface temperatures of up to 2500 K. IFTS data was temporally averaged over 10 s windows to improve SNR. The resulting evolving plume data is then compared with surface temperature measurements.

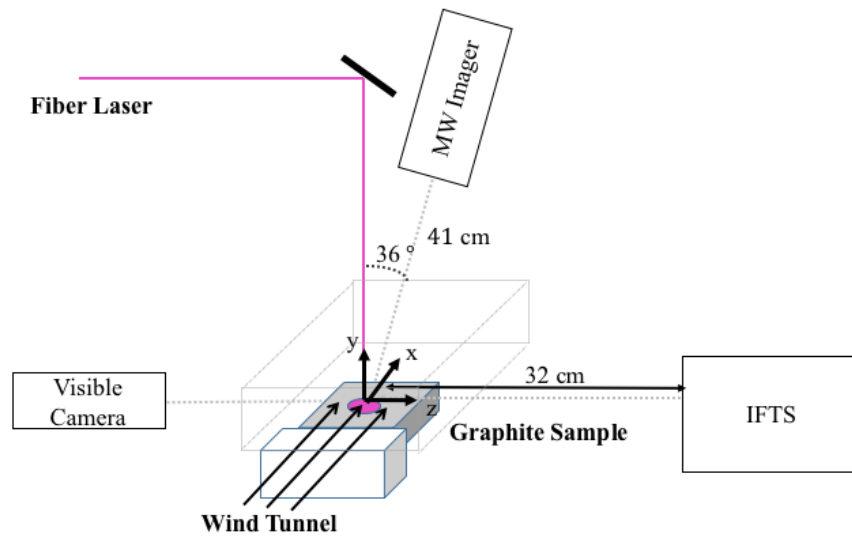


(a) Schematic

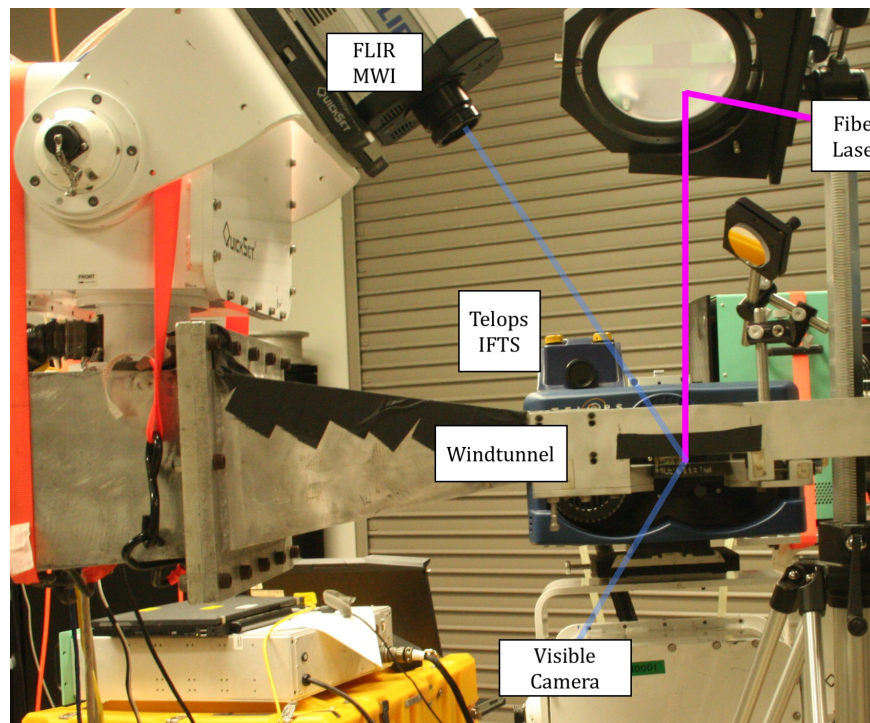


(b) Side view

Figure 22. Buoyant flow configuration

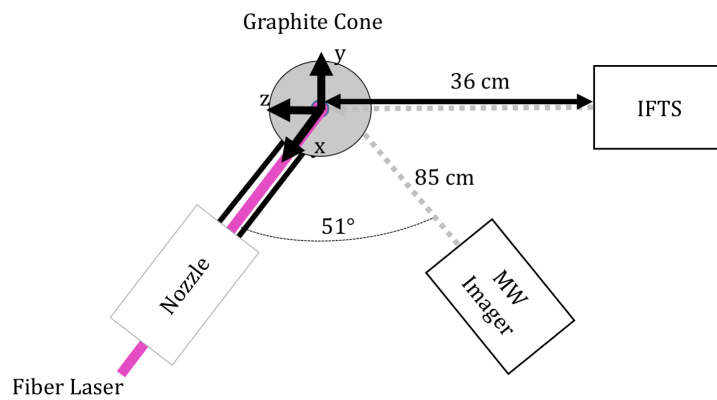


(a) Schematic

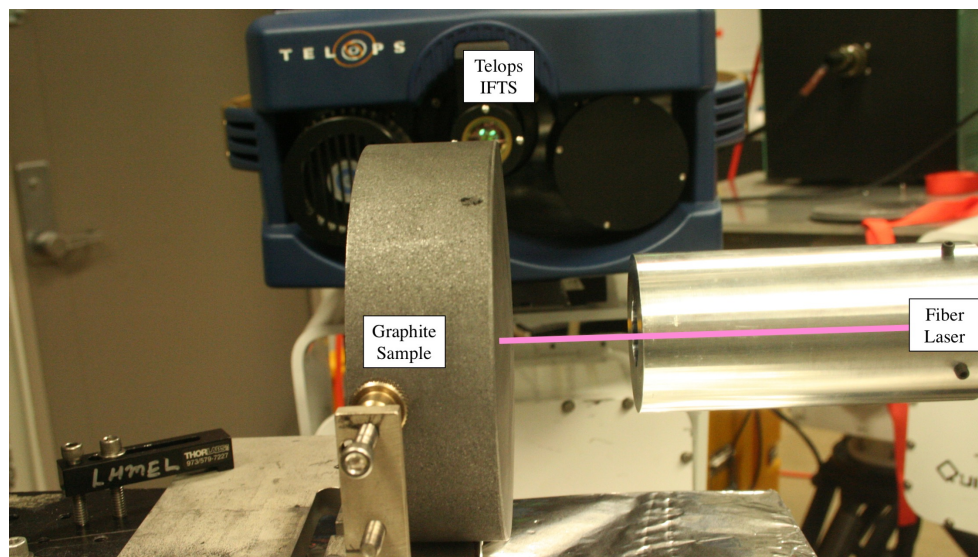


(b) Side view

Figure 23. Flat plate shear flow configuration.



(a) Schematic



(b) Side view

Figure 24. Stagnation flow configuration.

V. Imaging Fourier Transform Spectroscopy of Graphite Oxidation in a Buoyant Flow

This chapter focuses on detailing the use of the IFTS to characterize graphite oxidation in buoyant flow, in partial fulfillment of objective 1. The application of oxidation models, developed in Chapter III, are also discussed, in partial fulfillment of objective 2. The chapter is written in journal article format and can be read independently as a stand alone document. Additional details regarding background and experimental method can be found in Chapter II and IV, respectively.

5.1 Abstract

The oxidation of laser irradiated graphite is investigated for varying porosity and surface temperatures of 1500 - 3100 K at atmospheric pressure. Samples are irradiated using a 1.07 μm fiber laser at irradiances of 1000 and 3600 W/cm^2 in dry air environment (20% O_2 , < 1% H_2O), producing a buoyant flow. Combustion plumes are analyzed using a mid-wave (MW) imaging Fourier transform spectrometer (IFTS) at 2 cm^{-1} spectral resolution, 0.5 mm/pixel spatial resolution, and data cube rates of 1 Hz. Spectral signatures feature emission from CO and CO_2 in the 1800 - 2500 cm^{-1} spectral region. A radiative transfer model and cross-section data is used to infer species concentration and temperature from hyperspectral data, resulting in 2D characterization of the reacting boundary layer. Plume temperatures of up to 2500 K are observed. CO and CO_2 populations are highly correlated with temperature, with a general trend of $[\text{CO}]/[\text{CO}_2] = 22 \exp(-6,000/T_s)$. A simplified model incorporating diffusion transport and surface kinetics is presented to assess the relative strengths of the S1) $2\text{C} + \text{O}_2 \Rightarrow 2\text{CO}$, S2) $\text{C} + \text{CO}_2 \Rightarrow 2\text{CO}$, and S3) $\text{C} + \text{O}_2 \Rightarrow \text{CO}_2$ surface oxidation mechanisms. The role of kinetic and transport mechanisms is discussed.

5.2 Introduction

Carbon oxidation has been studied extensively due to its applications in coal combustion [29–31, 39, 43, 65–74]. Oxidizing species (O_2 , CO_2) react with the carbon surface, producing CO . The CO is then converted to CO_2 through the gas phase CO oxidation, which depletes the O_2 available for surface reactions. The CO_2 created in the gas phase reaction can then be used as a surface oxidizer. This coupling of surface and gas phase reactants and products is one of the main sources of complexity of this problem.

Table 6. Reactions and activation energies

	Reaction	$E_i(K)$	Ref
(G)	$CO + 1/2 O_2 \Rightarrow CO_2$	13,600	[15]
(S1)	$2C_s + O_2 \Rightarrow 2CO$	8,100-40,300	[21, 32–34]
(S2)	$C_s + CO_2 \Rightarrow 2CO$	24,000-43,300	[27–30]
(S3)	$C_s + O_2 \Rightarrow CO_2$	8,100-40,300	[21, 32, 34]

While CO oxidation is written simply as reaction G in Table 6, in reality it consists of many elementary reactions between CO , CO_2 , O_2 , and H_2O as well as their radicals. For simplicity, a single empirical expression is often used [20]:

$$R_g = [CO][O_2]^n A_g \exp\left(-\frac{E_g}{T}\right) \quad (114)$$

Values for n , A_g , and E_g , vary in literature depending on plume temperature and atmospheric conditions (% O_2 , % H_2O). We used the rate parameters provided in Table 6 derived for plume temperatures of 1900-2400 K at > 5% O_2 with 2% H_2O [15].

Surface oxidation mechanisms are typically described in terms of an empirical

reaction rate: the semiglobal form

$$R_s = k_s [C_{ox}]^m \quad (115)$$

where $[C_{ox}]$ is oxidizer concentration, k_s is the Arrhenius rate coefficient, and m is reaction order with $0 < m < 1$. Recent work has focused on developing a system of surface oxidation mechanisms to describe carbon oxidation [6, 75]. For simplicity, we will consider just the three reactions (S1, S2, and S3) shown in Table 6. Reactions with additional oxidizers, such as H_2O , or catalytic impurities are neglected. A first order ($m=1$) Arrhenius form is assumed for all surface reactions. Prior experimental work to determine appropriate pre-exponential factors and activation energies is complicated by the coupling of gas and surface reactions [10]. This coupling has lead to the debate on whether CO_2 observed at the surface is due to the S3 reaction, or created in the gas phase oxidation of CO near the surface or within the pores of the material [31].

Rate parameters for surface reactions vary across literature, both in pre-exponential factor and activation energies as shown in Table 6. Variation in reactivity is believed to be linked to graphite composition and manufacturing method. Graphite composition can alter activation energy due to catalytic effects of some minerals [10, 35]. Changes in production method can also result in variations in material porosity. Pores effectively create additional reactive surface area and increase the surface reaction rates. Samples with a high volatile content can increase in porosity due to pyrolysis of filler material as the sample is initially heated [27]. It has also been proposed that a distributed activation energy, to reflect the range of activation sites involved in the adsorption/desorption process, would be more appropriate [10].

Previous carbon oxidation studies are summarized in Table 7. Experimental studies

are typically described using the $[CO]/[CO_2]$ concentration ratio, expressed as:

$$[CO]/[CO_2] = \alpha \cdot [O_2]^n \exp(-\beta/T) \quad (116)$$

Little agreement in α and β is seen across studies, with β values ranging from 3,000 - 18,000 K. The $[CO]/[CO_2]$ ratio depends not only on the relative strengths of the surface and gas phase kinetics, but also on mass transport, which determines the availability of oxidizing species at the surface.

Table 7. Summary of carbon oxidation studies; Values of A,B, n correspond to Eq. (116)

Author	Ref	Material	T_s (K)	A	B (K)	n
Acosta	[7]	graphite	1800-2900	4910	17,970	-
Tognotti	[39]	char, spherocarb	670-1670	50	3,070	-0.21
Otterbien	[40]	graphite, vitreous carbon	781-863	26	3,020	-0.5
Phillips	[41]	graphon	800-950	140-200	3,220	-
Du	[21]	soot	670-890	120	3,200	
Arthur	[37]	graphite, coal	730-1170	2510	6,240	-
Rossberg	[38]	electrode carbons	790-1690	1860	7,200	-
Walker	[42]	graphon	800-950	170	3,220	-

Early methods of determining plume composition relied on gas chromatography (GC) or mass spectrometers (MS) [21, 27, 76, 77], and do not provide the spatial resolution of the flame structure needed to fully understand the diffusion limited kinetics. Recent work by Acosta provided the first spatially resolved plume measurements using IFTS, with resolution of 0.52 mm/pixel [1]. The spatially resolved data provided the first observations on relevant length scales for direct comparison with CFD simulations. However the previous IFTS study focused on spectral simulations and validation of the IFTS technique and did not provide a detailed kinetic interpretation.

The current study focuses on characterizing the oxidation of carbon surface as a function of temperature and graphite material. Measurements presented utilize the IFTS plume characterization technique developed by Acosta, with the addition of thermal imaging to provide spatially resolved surface temperatures. The current study expands the range of oxidation conditions, avoids significant particulate ejection and minimizes surface erosion. Three graphite samples are evaluated at surface temperatures of 1500-3100 K to determine dependence on material and surface temperature. Species and temperature maps are inferred from hyperspectral imagery. Diffusion transport is estimated using species gradients provided by the 2D species maps. A quasi 2D model incorporating diffusion and kinetics is also presented.

5.3 Experimental

Three graphite materials were each irradiated at 1000 and 3600 W/cm² for 180 s to produce steady state surface temperatures of 1500 - 3100 K. Samples were tested at the Wright-Patterson Air Force Base Laser Hardened Materials Evaluation Laboratory (LHMEL) using a 15 kW fiber laser at 1.07 μ m, which produced a 1.4 ± 0.2 cm diameter (defined as $1/e^2$) Gaussian beam. Quoted irradiance values of 1000 and 3600 W/cm² are spatially averaged over the beam profile. High and low irradiance conditions were chosen to observe a wide range of surface temperature conditions, but avoid sublimation ($T_s > 3900$ K).

A schematic of the experimental set-up is shown in Figure 25. Samples were mounted perpendicular to the beam in an open air environment (20% O₂, < 1% H₂O). The resulting buoyant flame is observed along the z axis using the MW IFTS and Phantom v7 visible high speed camera. Hyperspectral imagery is used to characterize plume properties (CO , CO_2 , T_p). Surface temperatures are observed using a FLIR SC6000 MWIR thermal imager mounted 51 degrees from normal.

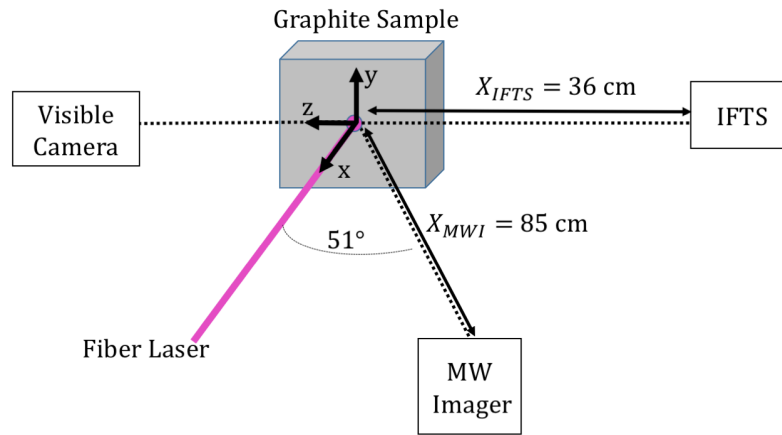


Figure 25. Schematic: laser irradiated graphite in buoyant flow

Materials.

Material properties of the three Graphtek graphite materials are shown in Table 8 [3]. The isomolded and fine samples are produced through an isostatic press and extrusion methods respectively. Impurities found in the ash content are not reported by the manufacturer, but previous work with fine samples report observations of Si, S, Fe, Ca, Al, and K [58]. Additionally these production methods make use of a more reactive binder material, which can react at much lower temperatures, increasing porosity [58, 78]. The pyrolytic material is produced in a layering method, which produces high purity samples with negligible porosity. The layering method results in high conductivity within the layers, but low conductivity between layers. Samples are cut such that the sample surface is a single layer (C-face). Additional details on graphite materials, impurities, as well as sample photographs can be found in [58].

Table 8. Graphite materials [3]

Material	ID	Density (g/cm ³)	Particle Size (μm)	Thermal Conductivity (W/m/K)	Ash (%)	Sample Size (in)
pyrolytic	PG-SN	2.2	NA	$k_{ }$: 400 k_{\perp} : 3.5	-	3 x 3 x 0.25
isomolded	GM-10	1.82	10.2	83	0.05	3 x 3 x 0.5
fine	GR008G	1.76	203	130	0.06	3* x 0.5

* 3 in diameter disks

Plume Measurements.

The combustion plume was characterized using the Telops MWIR hyperspectral imager. The MWIR Telops is an imaging Fourier transform spectrometer (IFTS) which provides spectral content at each pixel in a 320 by 256 InSb focal plane array (FPA). The IFTS is responsive from 1800-6667 cm⁻¹ ($\lambda = 1.5 - 5.5 \mu\text{m}$) with a variable spectral resolution of $\Delta\nu = 0.25 - 16 \text{ cm}^{-1}$. A 2 cm⁻¹ spectral resolution was chosen to allow for adequate resolution of the CO rotational features. A reduced window size of 64 x 256 was chosen resulting in a cube rate of 1 Hz. The 1.5 mrad pixel FOV resulted in a 0.42 mm/pixel spatial resolution. Further detail regarding the design and performance of the IFTS can be found in references [1, 7, 61, 62]

A simple two layer radiative transfer model (RTM) is used to fit the measured spectra. The measured spectra can be expressed as:

$$L_{det} = \tau_{atmos} \cdot [\epsilon_{plume}(n, X_{i-plume}, T_{plume}, \ell) \cdot B(T_{plume})] \quad (117)$$

where L_{det} is the measured spectral radiance, τ_{atmos} is the path transmission, ϵ_{plume} is the plume spectral emissivity, and $B(T_i)$ is the spectral radiance of a blackbody at T_i . Assuming equilibrium, emissivity can be written in terms of transmissivity ($\epsilon = 1 - \tau$),

with transmissivity defined by Beer's law:

$$\tau = \exp(-nl \sum_k X_k \sigma_k(\nu, T_{plume})) \quad (118)$$

where n is the number density, l is the path length, X_k is the plume species mole fraction, and σ_k is the species cross-section taken from HITRAN (CO , H_2O) and CDSD 4000 (CO_2) databases [46, 47]. The recent addition of the CDSD 4000 high temperature CO_2 cross-sections has been reported to provide much better agreement with reported CO_2 signatures above 2000 K [1, 63]. A least squares fitting routine with Equation 117 is used to infer T_{plume} , X_{CO} , and X_{CO_2} from the spectral signatures [1, 61]. A Planckian baseline was added to account for broadband emission observed in pixels near the sample surface, typically less than $10 \mu W/cm^2/sr/cm^{-1}$, which is attributed to slight blurring from radiating sample surface. Full 2D spatial maps of species concentration and plume temperature are inferred by fitting spectra at each pixel.

Uncertainties quoted for plume properties are based on the 95% confidence bounds of the fit and do not include systematic error. Plume temperature errors of less than 2% are observed for $T_{plume} = 1800 - 2500$ K. CO_2 uncertainties were typically 2–10%, with higher uncertainty for the low signal cases. Uncertainties for CO decrease with increasing concentrations, with uncertainties of < 20% for $X_{CO} > 0.01$ and < 10% for $X_{CO} > 0.1$. Two possible additional sources of error are line of sight averaging and pixel blurring. Error estimates for line of sight averaging are provided in Appendix B. Results suggest systematic errors of < 12% for species mole fraction and < 10% for plume temperature. To quantify the severity of the blurring, measurements of the edge spread function (ESF) were taken using a knife edge and blackbody. At focus, pixel blurring is minimal with less than 5% of radiant energy being deposited in neighboring pixels. However the most severe blurring is expected at the sample surface, where the hot sample edge is 3.8 cm off focus, causing a 10 % deposit of signature into the neighboring

pixels. In some cases this may result in falsely identifying the sample surface. Further detail regarding the MW Telops and its use as a combustion diagnostic can be found in [1, 61, 64, 79–81].

Thermal Measurements.

Surface temperatures were measured using the FLIR SC6000 thermal camera equipped with a 620 by 512 FPA sensitive at 3.8-4.0 μm . The SC6000 is capable of interweaving multiple integration times in a single test acquisition, allowing for a wider detection range. Thermal measurements were taken using a 2.0 ND filter and integration times of 0.1-1.5 ms, resulting in a noise floor of 600 K. Images were taken at 10 Hz and window size of 128x160 to reduce data volume. The FLIR was mounted 51° off normal to avoid laser path, resulting in vertical and horizontal spatial resolutions of 0.8 and 1.2 mm/pixel respectively.

Camera signal is converted to temperature measurements using an external blackbody (320-870 K) and calibration scheme [82]. The largest source of error in this method is the choice of material emissivity. Emissivities can vary across graphite materials, with most isotropic graphite materials showing high emissivity ($\epsilon > 0.8$), while pyrolytic graphite exhibiting emissivities as low as 0.4 [2, 83, 84]. Additionally, surface roughness can increase emissivity. In the laser damage scenario, this would result in an increase in emissivity from the low undamaged emissivity to a surface roughness dependent emissivity as the sample is irradiated. To improve surface temperature measurements, the emissivities of the graphite materials used in this study were evaluated using a Surface Optics Corp. SOC-100 Hemispherical Directional Reflectometer. Samples are illuminated using a calibrated blackbody source. Reflectance, ρ , is collected at all angles using a hemispherical mirror and focused onto a FTIR spectrometer. Emissivity is then calculated assuming equilibrium, $\epsilon = 1 - \rho$. Further details regarding the SOC

can be found in Ref [60]. Undamaged and irradiated samples were evaluated from room temperature to the instrument limit of 500°C at 3.9 μm . Although this is far below the surface temperatures used in this study (1500-3500 K), graphite emissivity has been previously shown to be relatively independent of temperature [2]. Thermal imagery is therefore processed using the emissivity of the irradiated samples measured at 30 – 500°C, assuming negligible change in emissivity at higher temperature.

5.4 Experimental Results and Discussion

Emissivity.

Emissivity data for the three graphite materials, both undamaged and irradiated, are shown in Table 9. For all samples, little surface temperature dependence was seen. A slight rise in emissivity is observed between undamaged and irradiated samples, most notably for pyrolytic samples. Similarly, work by Autio with UF-4-S, an isotropic extruded graphite, showed little temperature dependence, but did show an increase in emissivity with increased surface roughness. Autio pyrolytic data show little temperature dependence, but large variation depending on surface type (polished C-face versus A-face). Current pyrolytic measurements of the undamaged C-face fall slightly above Autio values, most likely due to the lack of surface polishing. Irradiated pyrolytic samples exhibit a slight increase in emissivity from undamaged, with values ranging between the current undamaged C-face measurements and Autio A-face measurements.

Table 9. Emissivities for undamaged and irradiated samples

	Undamaged	Irradiated
Material	ϵ_u	ϵ
Fine	0.92 \pm 0.01	0.93 \pm 0.01
Isomolded	0.88 \pm 0.01	0.90 \pm 0.03
Pyrolytic	0.52 \pm 0.05	0.58 \pm 0.05

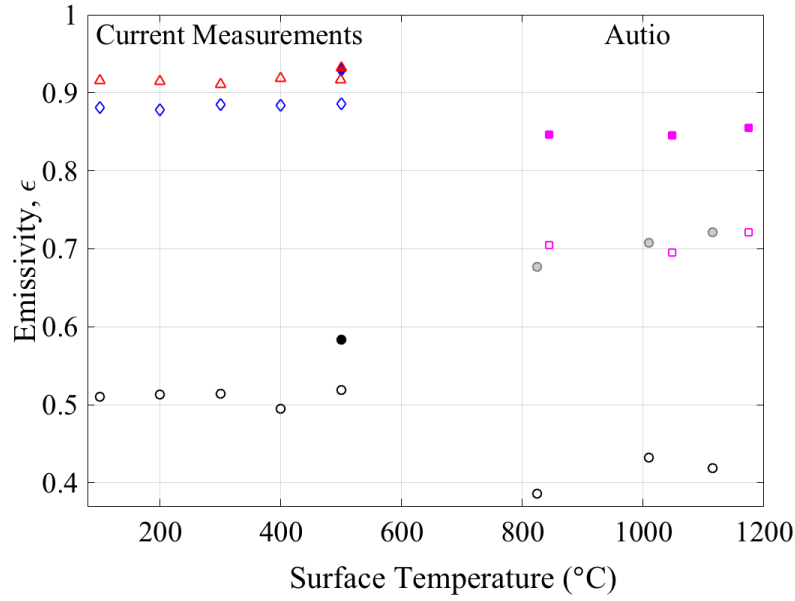


Figure 26. Graphite emissivity versus temperature;
Current measurements: material - (Δ) fine, (\diamond) isomolded, (\circ) pyrolytic C-face; surface: irradiated (full), undamaged (open); Autio [2]: (\blacksquare) UF-4-S rough, (\square) UF-4-S polished; (\bullet) pyrolytic A-face, (\circ) pyrolytic C-face polished

Surface Temperature.

MWIR imagery is converted to temperature maps using the graphite emissivities shown in Table 9. Time profiles of peak surface temperature are provided in Figure 27. For the isotropic materials (fine, isomolded), samples are **slowly heated** (50 and 200 K/s for low and high irradiance, respectively) and **ignite** within the first 60 s. The samples continue heating until reaching steady state, roughly within 100 and 50 s for low and high irradiance, respectively. For the anisotropic pyrolytic material, the surface layer is heated much more quickly due to the low conductivity between layers, resulting in heating rates of 1000 K/s and near instantaneous ignition (< 0.5 s), followed by quickly reaching steady state ($t < 5$ s). A detailed analysis of the heat transfer properties was done in parallel of this work and can be found in Ref. [82].

Temperature uncertainty is mainly due to **uncertainty in material emissivity**. For fine and isomolded materials, this results in temperature uncertainties of 3000 ± 20 K and 3000 ± 120 K, respectively. For pyrolytic materials, temperature uncertainties are much more severe, resulting in uncertainties of 3000 ± 1260 K. These uncertainties do not include systematic error, which may result from the measurement technique or in applying **emissivities measured at 780 K to higher surface temperature conditions** (1000 - 4000 K). Surface temperatures inferred for the high irradiance case suggest pyrolytic emissivity is under predicted, resulting in over estimation of surface temperature. Visual inspection of samples post test does not indicate significant hole formation, suggesting surface temperatures are under the 3900K sublimation condition. This is in conflict with the 4000 K surface temperatures inferred assuming an emissivity of 0.58, suggesting that a higher emissivity is appropriate.

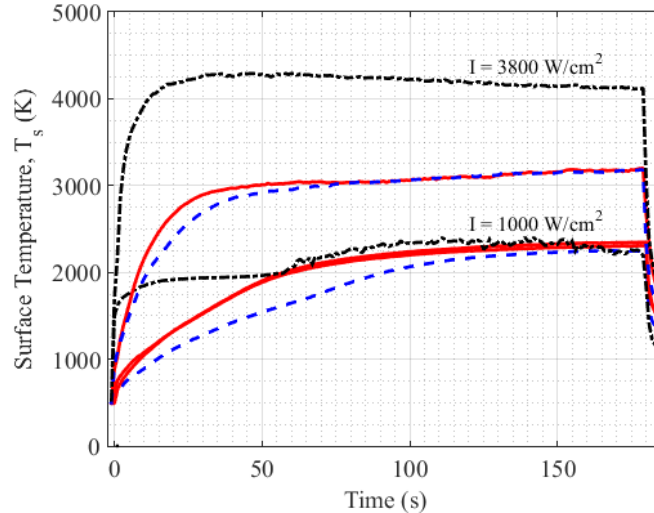


Figure 27. Surface temperatures over time. (—) fine, (---) isomolded, (- · -) pyrolytic

Plume Properties.

IFTS hyperspectral imagery was used to infer plume temperature and species concentration. Plume spectra are time averaged over the relatively steady region, from $t = 100 - 150$ s. Sample spectrum from a single pixel of a hyperspectral datacube is shown Figure 28. Measured spectra was fit using the RTM given in Eq. (142). Simulated emissivities and path transmission are also shown. Modeled spectra is in good agreement with measured data, with the exception of the $2250 - 2400 \text{ cm}^{-1}$ region where path transmission features dominate, highlighting the limitations of the two layer model. Despite these issues, good fits of the fine CO structure and broad CO_2 feature outside of the atmospheric absorption region still allow good estimation of the plume properties. The simulated fits results in plume values of $T_{plume} = 2240 \pm 40 \text{ K}$, $X_{CO_2} = 0.112 \pm 0.004$, and $X_{CO} = 0.26 \pm 0.03$, where error bounds represent the 95% confidence interval and do not include systematic error. Systematic errors of $<6 \%$ for plume temperature and $5\text{-}21 \%$ for species mole fraction are estimated (see Appendix B). The largest source of systematic error is the choice of flame length, which directly influences X_i . Reported mole fractions assume a constant flame length of 2 cm across all lines of sight.

Full spatial maps are produced by fitting all pixels in the hyperspectral data cube using a nonlinear fitting routine. Plume maps are shown in Figure 29 for an isomolded samples irradiated at 1000 and 3600 W/cm^2 . The beam is incident horizontally, centered at $y = 0$ with a radius of 7 mm. The high surface temperatures within the beam activates surface oxidation, producing CO at the surface. As the CO diffuses away, it reacts with the available O_2 producing CO_2 in the exothermic CO oxidation. The discontinuity seen in the 1000 W/cm^2 case near laser center is due to slight angling of the sample surface. Comparing the high and low irradiance case, higher surface temperatures for the 3600 W/cm^2 case result in higher CO at the surface, with X_{CO} of 0.33 and 0.12 for the high and low irradiance, respectively. The increase in CO population allowed

the CO to diffuse farther from the surface, creating a thicker flame. Buoyancy effects can be seen in flame asymmetry, both in the high CO_2 concentrations and plume temperatures observed above beam center. Estimates of the Grashof number using peak observed temperatures ($T_{plume} = 2500$ K and $T_s = 4000$ K) are well within turbulent limits $Gr = 5 \cdot 10^4 < Gr_{turb} = 10^9$, suggesting a **laminar boundary layer**.

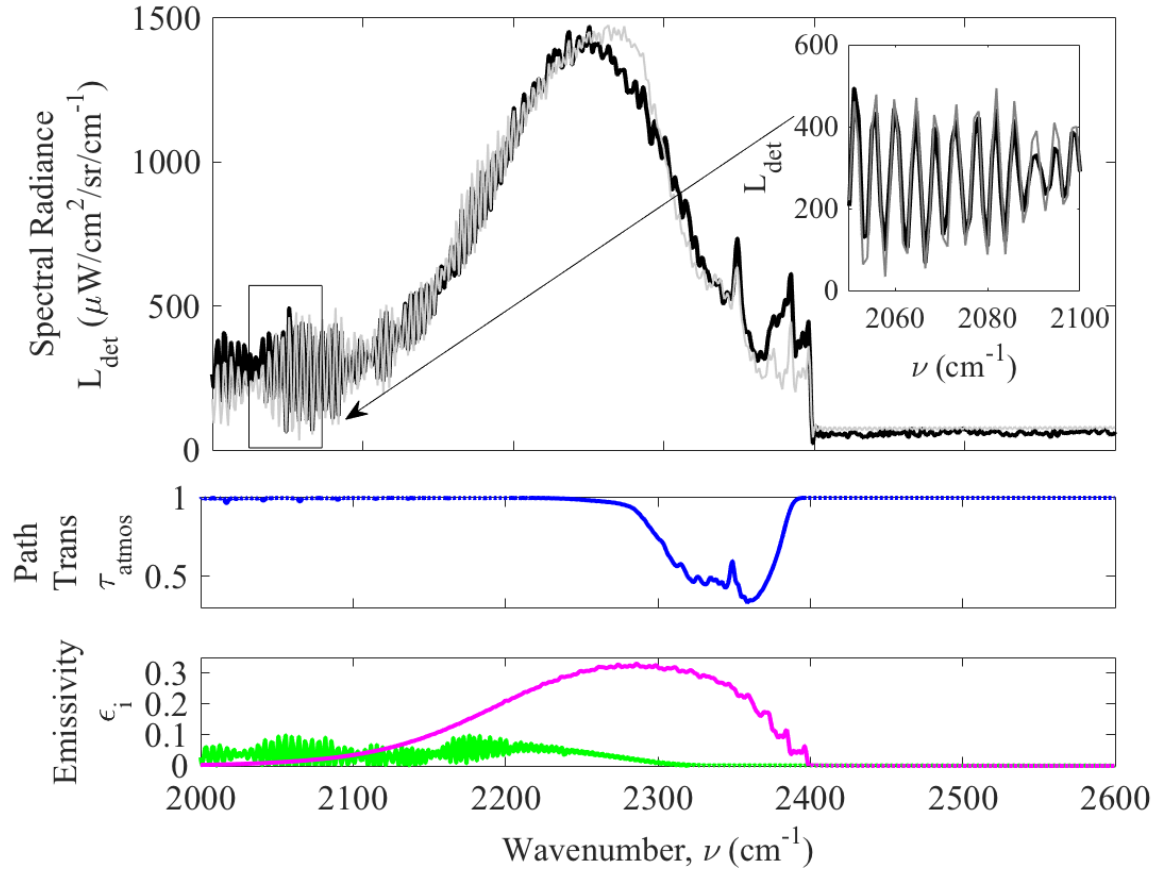
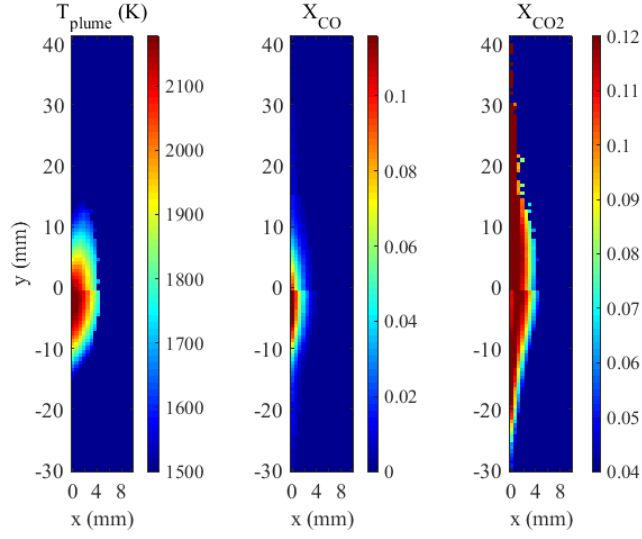
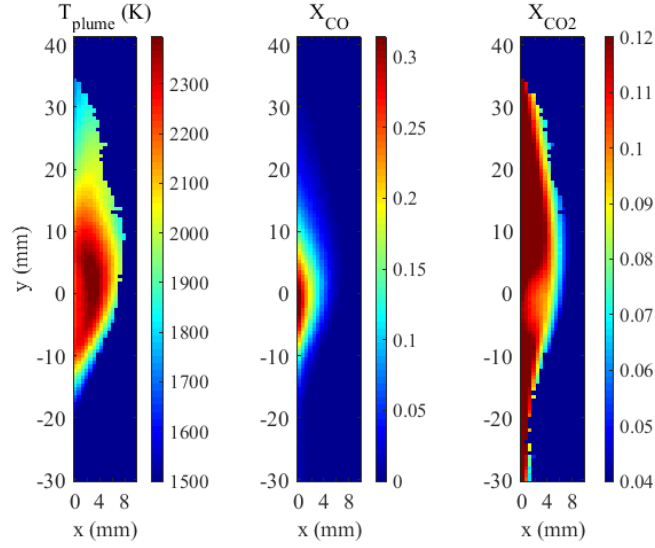


Figure 28. Sample measured and simulated spectra for isomolded sample irradiated at $1000 \text{ W}/\text{cm}^2$. Pixel located adjacent to surface, near beam center. (---) measured radiance, L_{det} ; (—) modeled radiance; (—) τ_{atmos} ; (—) ϵ_{CO} ; (—) ϵ_{CO_2} . Model fits correspond to $T_{plume} = 2240 \pm 40$ K, $X_{CO_2} = 0.112 \pm 0.004$, $X_{CO} = 0.26 \pm 0.03$.

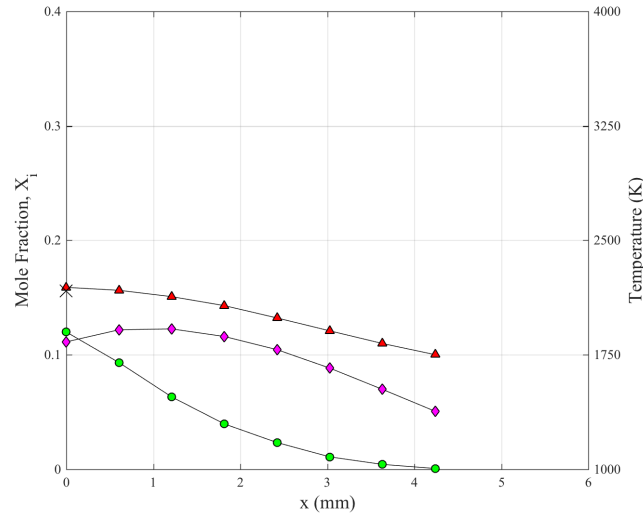


(a) $I = 1000 \text{ W/cm}^2$

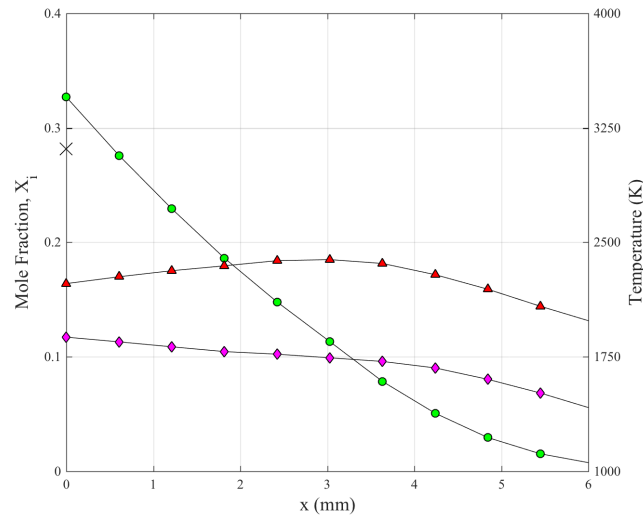


(b) $I = 3600 \text{ W/cm}^2$

Figure 29. Plume temperature and species mole fractions, X_i , inferred from Telops data, isomolded sample irradiated at 1000 W/cm^2 and 3600 W/cm^2 .



(a) $I = 1000 \text{ W/cm}^2$



(b) $I = 3600 \text{ W/cm}^2$

Figure 30. Plume properties along surface normal for isomolded sample irradiated at 1000 W/cm² and 3600 W/cm². (●) CO, (◆) CO₂, (▲) T_{plume} , (X) T_s

Plume properties normal to the surface evaluated at laser center ($y = 0$) for isomolded samples irradiated at 1000 and 3600 W/cm² are shown in Figure 30. The higher

irradiance case results in an increase in surface temperature, with T_s of 2200 and 3100 K for the low and high irradiance cases respectively. However, there is only a slight rise in peak plume temperature, from 2200 to 2400 K, with surface temperature and plume temperature no longer at thermal equilibrium at the surface for the high irradiance case. In the low irradiance case, plume temperature peaks at the surface, suggesting sufficient O_2 throughout the reacting region. In the high irradiance case, plume temperature peaks a few mm off the surface, and decreases towards the surface, suggesting that optimal $CO : O_2$ is reached off the surface and depleted O_2 population at the surface.

Increase in surface reactivity results in a rise in X_{CO} from 0.12 to 0.33. The CO produced at the surface is consumed in the gas phase reaction as it diffuses from the surface, resulting in flame widths of 4 and 6 mm for the low and high irradiance cases respectively. CO_2 profiles vary significantly between the low and high irradiance cases. The direction of the CO_2 diffusion flux, Γ_{CO_2-x} , can be inferred from the shape of the profiles where $-\Gamma_{CO_2-x} \propto \frac{d[CO_2]}{dx}$. For the low irradiance case, diffusion towards the surface is indicated by the positive slope at the surface, suggesting activation of the S2 reaction and consumption of CO_2 at the surface. For the high irradiance case, the CO_2 profile is relatively flat, even at the surface where strong CO_2 consumption is expected due to the increased surface reactivity. This may indicate some CO inhibition of the S2 reaction as others have reported [85]. The slightly negative slope indicates some CO_2 creation at the surface, either due to the gas phase reaction or S3, suggesting some O_2 availability at the surface.

Plume properties along the surface ($x = 0$) are shown in Figure 31 for isomolded samples irradiated at 1000 and 3600 W/cm². Again note the non-equilibrium between T_s and T_{plume} for the high irradiance case, with T_{plume} peaking at 2500 K. The CO concentration is highly correlated to surface temperature, peaking at $X_{CO} = 0.12$ and 0.33 for the low and high irradiance cases respectively. A dip in CO_2 near laser center

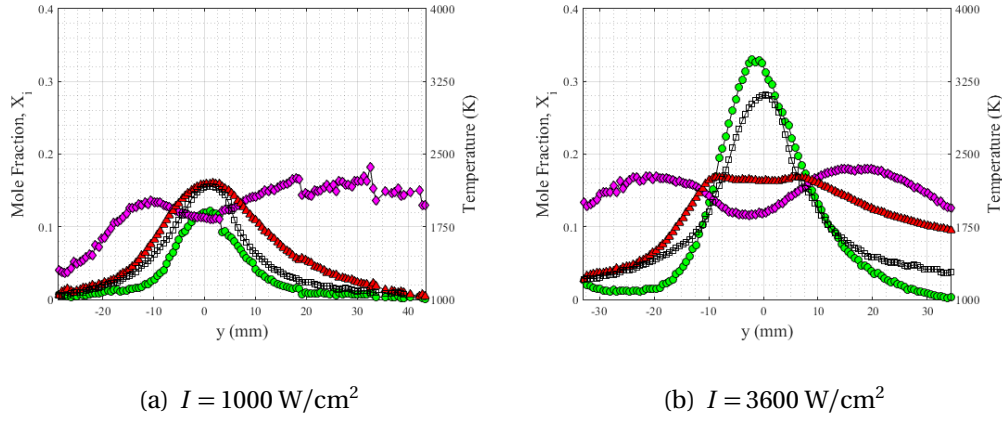


Figure 31. Plume properties along surface ($x=0$) for isomolded sample irradiated at 1000 W/cm^2 and 3600 W/cm^2 . (●) CO , (◆) CO_2 , (▲) T_{plume} , (□) T_s

is observed for both cases. The drop in CO_2 population may be a result of two effects: 1) the depletion of O_2 as it diffuses to towards the surface due to the CO oxidation, restricting the O_2 available at the surface for CO_2 production and 2) high T_s within the beam activating the S2 reaction and depleting the CO_2 population. The flame asymmetry due to buoyancy is evident in the higher T_{plume} and CO_2 above laser center as a result of the upward movement of the CO oxidation products.



Diffusion.

Diffusion flux can be evaluated directly from imagery. Diffusion flux is expressed as:

$$\Gamma_i = -D_i \frac{dC_i}{dx} \quad (119)$$

where D_i is the diffusion coefficient and $\frac{dC_i}{dx}$ is the concentration gradient. Diffusion is assumed to be mainly in the x direction due to the strong concentration gradient normal to the surface, $\frac{dC_i}{dx} > \frac{dC_i}{dy}$. The diffusion flux can then be estimated using finite

differencing:

$$\Gamma_i(j) = -\frac{D_i}{\Delta x} [(C_i(j, 2) - C_i(j, 1))] \quad (120)$$

where D_i is estimated using empirical fits found in Yaws [86], $C_i(j, k)$ is the species concentration in pixel (j, k) , and Δx is the pixel resolution.

The resulting surface flux for CO and CO_2 along the surface are shown in Figure 32 and Figure 33 for an isomolded sample at 1000 and 3600 W/cm² respectively. High CO flux is due to surface CO production through S1 and S2, which peak at laser center. Because CO_2 is produced throughout the plume, CO_2 gradients are much smaller, resulting in lower flux. The effects of S2 consumption of CO_2 can still be seen in the dip in Γ_{CO_2} , which results in a negative flux (towards surface) for the lower irradiance case as noted in Figure 30. Similar flux profiles were observed in all test cases.

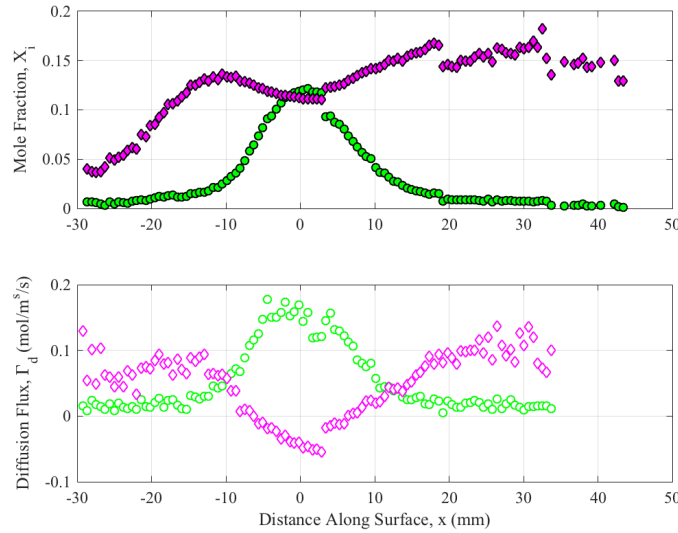


Figure 32. Mole fractions and flux along surface for isomolded sample irradiated at 1000 W/cm². Top: Mole fraction: (●) X_{CO} , (◆) X_{CO_2} ; Bottom: Surface diffusion flux calculated using Eq. (120): (○) Γ_{CO} , (◇) Γ_{CO_2} .

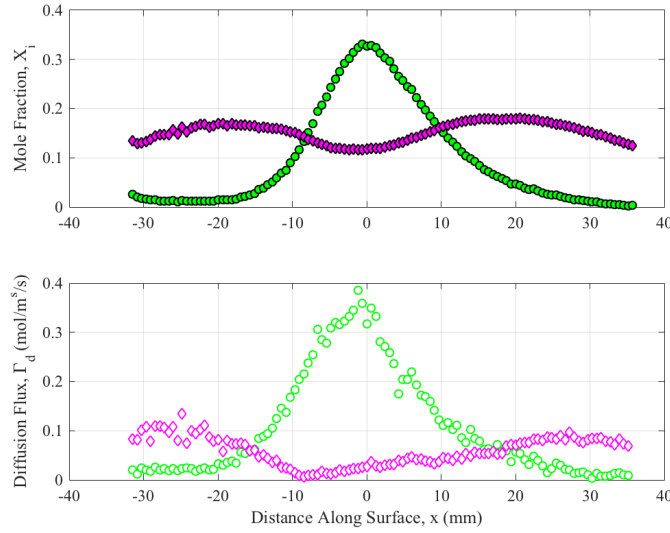


Figure 33. Mole fractions and flux along surface for isomolded sample irradiated at 3600 W/cm². Top: Mole fraction: (●) X_{CO} , (◆) X_{CO_2} ; Bottom: Surface diffusion flux calculated using Eq. (120): (○) Γ_{CO} , (◇) Γ_{CO_2}

Temperature Dependence of $[CO]/[CO_2]$ Ratio.

Measurements of $[CO]/[CO_2]$ column density ratio evaluated at sample surface ($x = 0$) are plotted versus inverse surface temperature in Figure 34. Little difference is seen across material or irradiance conditions. A sharp change in $[CO]/[CO_2]$ is seen at 1600K, suggesting a change in the limiting kinetics between low and high T_s regimes. Some hysteresis can be seen at peak temperature, where $[CO]/[CO_2]$ values above laser center are higher than those below laser center. This may be due to varying O_2 availability along the surface. Below the beam, O_2 can diffuse through the relatively thin reaction layer. Above laser center, the reaction layer is significantly thicker, limiting the O_2 available at the surface. Fits to Eq. (116) neglecting O_2 ($n = 0$) give the following expression for $T_s > 1600$ K:

$$\frac{CO}{CO_2} = (22 \pm 3) \cdot \exp\left(\frac{-6,000 \pm 500}{T_s}\right) \quad (121)$$

β values are significantly lower than the 18,000 K recently reported by Acosta, but are in good agreement with 6,000- 7,000 K values reported by Arthur and Rossberg [7, 37, 38]. While Acosta's work similarly used IFTS to determine $[CO]/[CO_2]$, there were a few key differences between Acosta and the data presented. First, Acosta thermal measurements were taken using a single channel pyrometer pointed at laser center. A range of temperature points was achieved by evaluating the $[CO]/[CO_2]$ over the heating period and through to steady state. In the current case, measurements are only evaluated at steady state. The range of temperature conditions is achieved using the spatially resolved species profiles and spatially resolved surface temperature measurements. It is unclear why these differences would result in higher β values.

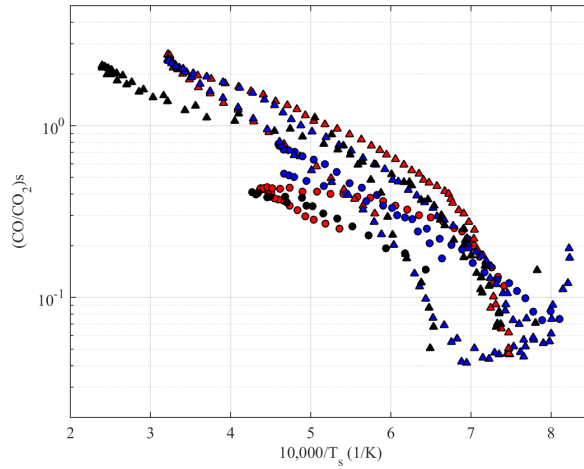


Figure 34. $[CO]/[CO_2]$ vs T_s evaluated at surface. (○) 1000 W/cm², (△) 3600 W/cm², (•) fine, (•) iso-molded, (•) pyrolytic

5.5 Model

A simplified, diffusion kinetic model is developed to further interpret the current observations. Applying the species conservation equations to a small control volume

adjacent to the surface, the following rate equations are obtained (see Chapter III):

$$\left(\frac{dC_i}{dt}\right)_s = \omega_i + v_s \frac{dC_i}{dy} - \frac{1}{\Delta x} [\omega_s - \Gamma_i] \quad (122)$$

where ω_i is the reaction source term, $v_s \frac{C_i}{dy}$ is the convective transport term assuming velocity $v = (0, v_s)$, ω_s is the surface reaction source term, Γ_i is the diffusion flux term, and Δx is the width of the control volume. Diffusion flux is assumed to be mainly in the x direction due to the strong concentration gradient normal to the surface, $\frac{dC_i}{dx} > \frac{dC_i}{dy}$. Applying Eq. (122) to the three species of interest, the following rate equations are obtained:

$$\left(\frac{d[O_2]}{dt}\right)_s = -\frac{1}{2}R_g + v_s \frac{d[O_2]}{dy} + \frac{1}{\Delta x} [-R_{s1} - R_{s3} - \Gamma_{O_2}] \quad (123)$$

$$\left(\frac{d[CO]}{dt}\right)_s = -R_g + v_s \frac{d[CO]}{dy} + \frac{1}{\Delta x} [2R_{s1} + 2R_{s2} - \Gamma_{CO}] \quad (124)$$

$$\left(\frac{d[CO_2]}{dt}\right)_s = R_g + v_s \frac{d[CO_2]}{dy} + \frac{1}{\Delta x} [-R_{s2} + R_{s3} - \Gamma_{CO_2}] \quad (125)$$

where the rates, R_g is the gas phase reaction rate assumed to be of the form:

$$R_g = A_g [O_2]^{0.2} [CO] \exp\left(-\frac{E_g}{T_{plume}}\right) \quad (126)$$

and R_{si} are the surface reaction rate assumed to be first order Arrhenius. Due to the non-equilibrium between gas and surface temperatures at the surface, a modified expression for k_i was chosen to reflect the surface reaction dependence on plume and surface temperature using a temperature mixing coefficient, ϕ :

$$k_i = A_i \exp\left(-\frac{E_i}{\phi_i T_s - (1 - \phi_i) T_p}\right) \quad (127)$$

To reduce the species conservation equations into a simplified ODE, the following

approximated diffusion flux is proposed:

$$\Gamma_i(j) = \begin{cases} -\frac{D_i}{\delta_d} [C_i^o - C_i(j, 1)] & i = CO, O_2 \\ 0 & i = CO_2 \end{cases} \quad (128)$$

where δ_d is a length scale on the order of the flame width, and C_i^o is the freestream concentration of species i . The CO_2 flux is assumed negligible compared to O_2 and CO flux.

Comparison of the approximated flux computed using Eq. (128) and the results from Eq. (120) are shown in Figure 35. Good agreement for was found using a length scale of half the flame thickness ($\delta_d = 3$ mm). The zero flux assumption for CO_2 clearly breaks down, with errors as high as $0.05 \text{ mol/m}^2/\text{s}$ within beam center.

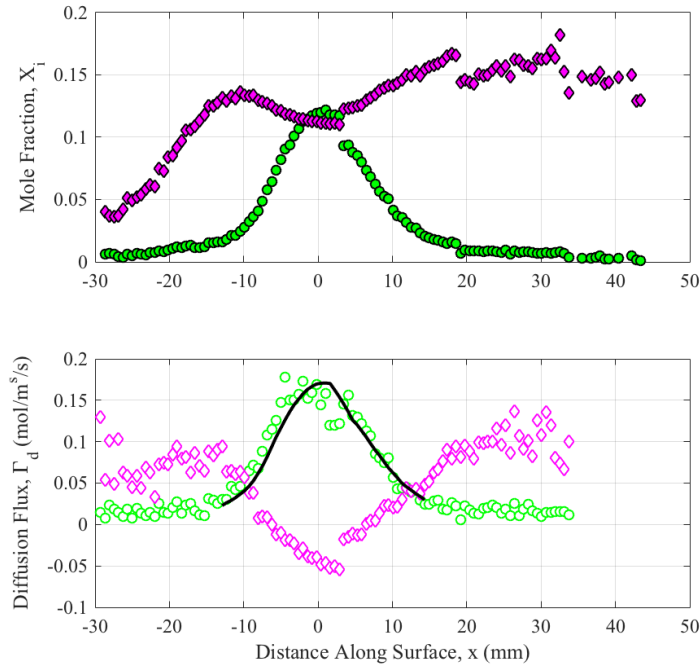


Figure 35. Diffusion flux along surface for isomolded sample irradiated at 1000 W/cm^2 . Diffusion flux calculated using Eq. (120): (\circ) Γ_{CO} , (\diamond) Γ_{CO_2} . Diffusion flux approximated using Eq. (128): (—) Γ_{CO}

Combining Eq. (123) - (128) and assuming steady state, results in a system of three first order ODEs. Boundary conditions are provided by the upstream conditions, which are assumed to be the free stream values ($X_{O_2}^o = 0.2$, $X_{CO}^o = 0$, and $X_{CO_2}^o = 0$). Due to nonlinearity and the coupling of the ODEs, a numerical solver is used. A nonlinear least squares fitting routine is used to determine reaction rate parameters necessary for agreement between simulated CO and CO_2 profiles and experimental observations. Surface reaction rates are controlled through fitting of A_i and E_i , which were allowed to vary from sample to sample. Gas phase reaction rates were controlled through fitting of A_g , which was then fixed based on best fit of the six test cases.

5.6 Model Results and Discussion

Sample fit results are shown in Figure 36 for isomolded samples irradiated at 3600 W/cm². Fits to rate parameters are achieved using a nonlinear fitting routine comparing simulated species profiles to experimental data. Reaction rates are computed using the experimental temperature profiles given in the top portion of the figure, with surface temperatures of 1400 - 3000 K. Simulated reaction rates are shown in the middle portion of the figure along with CO transport mechanisms. The resulting simulated species profiles are compared with measured profiles in the bottom portion of the figure. Good agreement is found between measured and simulated concentration profiles, with normalized root mean squared error (RMSE) of 4%.

These results allow us to infer some information about the balance of kinetic and transport mechanisms. For the CO_2 population, there is clearly a balance between CO_2 consumption through S2 and production through the gas phase reaction. For the CO population, CO production is clearly dominated by the S1 reaction, with some contribution from the S2 reaction. Due to the low flow velocities, contributions from convective transport are significantly lower than diffusion transport. This suggests

that CO is determined by balance of surface production, predominantly due to the S1: $C - O_2$ reaction, and diffusion losses.

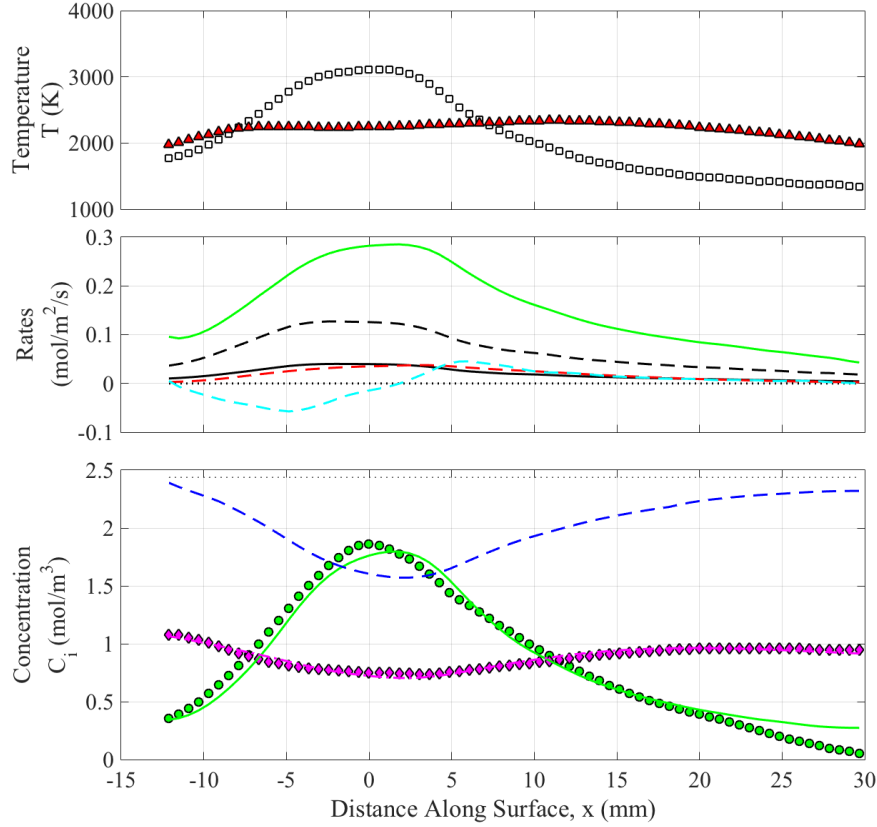


Figure 36. Sample model fits for fine sample irradiated at 3600 W/cm^2 . Top: temperature measurements: (\square) T_s , (\blacktriangle) T_{plume} , Middle: modeled rates: ($- -$) R_1 , ($-$) R_2 , ($-$) $\Delta x R_g$, ($-$) Γ_{d-CO} , and ($- -$) Γ_{c-CO} . Bottom: species concentrations- (\bullet) - measured CO , (\blacklozenge) - measured CO_2 , ($-$) modeled CO , ($- -$) modeled CO_2 , ($- - -$) modeled O_2 , and (...) freestream O_2^o

$[CO]/[CO_2]$ Temperature Dependence.

Although $[CO]/[CO_2]$ data is often expressed in terms of Eq. (116), it is useful to derive an expression in terms of kinetic mechanisms. Looking at CO_2 conservation

Table 10. Simulation parameters.

parameter	value	units
A_1 (S1) pre-exponential	3.5	m/s
A_2 (S2) pre-exponential	3.2	m/s
E_1 (S1) activation energy	10200	K
E_2 (S2) activation energy	10900	K
ϕ_1 mixing coefficient	0.5	K
ϕ_2 mixing coefficient	0.5	K
A_g (G) pre-exponential	$2.5 \cdot 10^4$	$(\text{mol}/\text{m}^3)^{-0.2} \text{ 1/s}$
E_g (G) activation energy	15,100	K
δ_d diffusion length scale	4-6	mm
v_s surface velocity	0.5	m/s

expressed in Eq. (125) and assuming negligible contributions from R_{s3} , Γ_{CO_2} , and convective flux, the following expression for $[CO]/[CO_2]$ can be derived:

$$\frac{CO}{CO_2} = [O_2]^{-0.2} \frac{1}{\Delta x} \frac{k_2}{k_g} \quad (129)$$

From this equation, the $[CO]/[CO_2]$ ratio is determined by the balance of CO_2 destruction at the surface through S2 and the CO_2 creation through the gas phase oxidation of CO . Negative O_2 dependence is in agreement trends reported by Otterbrien ($n = -0.18$), Du ($n = -0.23$) and Tognotti ($n = -0.21$) [21, 39, 40]. Negative O_2 dependence also agrees well with previous experimental observations. An increase in $[CO]/[CO_2]$ ratio between low and high irradiance is observed for all materials. The increase in irradiance produces a thicker flame, which makes it more difficult for O_2 to reach the surface. Therefore the rise in $[CO]/[CO_2]$ may be due to a decrease in O_2 .

Non-uniqueness.

Although the simplified kinetic transport model is useful in interpreting experimental data and replicating observed trends, it should be noted that there are issues of

non-uniqueness present in the model with prevent determining exact values for kinetic rate parameters. Central to this issue is the choice of A_g . Take Eq. (125), assuming steady state, negligible convection and diffusion, and negligible contribution of the S3 reaction:

$$\Delta x k_g [CO][O_2]^{0.2} = k_2 [CO_2] \quad (130)$$

which states that CO_2 created in the gas phase is balanced by the consumption of the S2 reaction. This highlights the coupling of k_g and k_2 terms, meaning choice of A_g directly determines A_2 . Choice of A_2 then influences S1 parameters through the coupling of S1 and S2 through the CO conservation equations. As values of A_g can vary by orders of magnitude in literature, it is then difficult to infer exact values for kinetic rate parameters.

5.7 Conclusions

The oxidation of laser irradiated graphite in buoyant flow has been characterized for three graphite materials at surface temperatures of 1500-3100 K. Spatial maps of CO , CO_2 , and T_{plume} are obtained using IFTS. Plume temperatures were found to be in non-equilibrium with surface temperatures, peaking at 2500 K. CO population is found to be highly correlated with surface temperature due to production through S1 and S2 surface reactions. CO_2 populations were found to decrease at laser center due to the S2 reaction. A general trend of $[CO]/[CO_2] = 22 \exp(-6000/T_s)$ is reported for $T_s = 1600-3100$. Little difference between graphite material is noted.

A simplified species conservation model, incorporating kinetics and diffusion, is presented to interpret experimental observations. A nonlinear fit routine comparing simulated and measured species profiles is used to determine the relative strengths of surface reactions. Results suggest CO population controlled by balance between production at the surface, predominantly through the S1: $C_s - O_2 \Rightarrow 2CO$ reaction,

and diffusion away from the surface. Results also indicate $C O_2$ population is controlled by the balance between consumption at the surface through S2: $C_s - C O_2 \Rightarrow 2 C O$ and production through the gas phase reaction, suggesting the contributions from the S3: $C_s - O_2 \Rightarrow C O_2$ reaction are negligible.

While the model presented provides insight into the relative contributions of kinetic and transport terms, several limitations should be discussed. First, the coupling of kinetic mechanisms presents an issue of non-uniqueness, making it difficult to accurately determine rate parameters. This may be improved through a set of experiments to decouple these parameters, such as graphite oxidation in $C O_2 / N_2$ which would isolate the S2 reaction from any O_2 mechanisms. Second, this model greatly over simplifies transport and kinetic mechanisms. In the case of kinetics, the use of Arrhenius rate expressions greatly reduces the computational complexity, but does not capture the influence of individual elementary reactions, many of which contribute to non-Arrhenius behavior. Due to these issues, rate parameters used should be considered model fit parameters and not an estimation of actual values. This technique was used simply to gage the relative contributions of kinetic and transport mechanisms and interpret experimental trends. This points to the need for detailed CFD simulations which not only greatly improve transport modeling, but can also incorporate complex kinetic rate packages.

While IFTS is an incredibly useful diagnostic, several limitations should also be noted. First, IFTS imagery remains a line of sight measurement, and due to the nonlinearities of radiative transfer, the line of sight effects can be nontrivial. Second, inferred mole fractions are highly dependent on choice of flame length due to their coupling in optical depth (see Appendix B). Data presented in this study assumes a constant flame length along the line of sight. Constant flame length assumption is less problematic along the surface, where flame width is on the order of laser beam width and relatively

constant above laser center. However this assumption may be particularly problematic when comparing measurements normal to the surface, where flame thickness changes dramatically from surface to flame edge.

VI. Imaging Fourier Transform Spectroscopy of Graphite Oxidation in a Flat Plate Shear Flow

This chapter focuses on expanding IFTS graphite oxidation measurements to the flat plate shear flow, in partial fulfillment of objective 1. Oxidation models, developed in Chapter III and evaluated against buoyant flow data in Chapter V, are evaluated for the current flow configuration, in partial fulfillment of objective 2. The chapter is written in journal article format and can be read independently as a stand alone document. Additional details regarding background and experimental method can be found in Chapter II and IV, respectively.

6.1 Abstract

The oxidation of laser irradiated graphite in laminar flow is characterized using imaging Fourier transform spectroscopy (IFTS). Samples of varying porosity are irradiated using a 1.07 μm fiber laser at irradiances of 750 and 1500 W/cm^2 in a dry flow (20% O_2 , < 1% H_2O) with flow speeds of 5 - 10 m/s, resulting in surface temperatures of 1000 - 4000 K. The resulting reacting layer is observed using a midwave (MW) IFTS at 2 cm^{-1} spectral resolution, 0.5 mm/pixel spatial resolution, and 0.75 Hz data cube rate. Spectral signatures feature emission from CO and CO_2 in the 1800 - 2500 cm^{-1} spectral region. A two layer radiative transfer model using the CDSD-4000 and HITEMP cross-section databases was used to determine path-averaged plume temperature, CO , and CO_2 concentrations from spectral signatures. Plume temperatures are found to be in non-equilibrium with surface temperatures, with peak plume temperatures of only 2500 K. CO and CO_2 populations are highly correlated with surface and plume temperature. A general trend of $[\text{CO}]/[\text{CO}_2] = 7.8 \exp(-3100/T_s)$ is reported for all materials. This data set represents the first spatially resolved measurements of graphite oxidation in a flat plate shear flow.

6.2 Introduction

Although carbon oxidation has been studied extensively both experimentally [10, 21, 27, 40, 41] and theoretically [23, 43, 87], much is still not understood regarding the coupling of kinetics and transport mechanisms. Carbon oxidation can be simplified to the reactions shown in Table 11. The CO produced at the surface through S1 and S2 is converted to CO_2 as it diffuses away from the surface. A portion of the CO_2 then diffuses back to the surface to supply the S2 reaction. The CO oxidation in the reacting layer then controls the oxidizing species available at the surface through consumption of O_2 and production of CO_2 . Accurately predicting carbon oxidation then requires detailed knowledge of CO and surface oxidation mechanisms as well as mass transport.

Table 11. Oxidation mechanisms

	Reaction
(G)	$CO + 1/2 O_2 \Rightarrow CO_2$
(S1)	$2C_s + O_2 \Rightarrow 2CO$
(S2)	$C_s + CO_2 \Rightarrow 2CO$

Imaging Fourier transform spectroscopy (IFTS) has recently been demonstrated as a useful combustion diagnostic due to the ability to infer spatial 2D maps of plume temperature and species concentration [61, 62, 64, 79]. This technique was first demonstrated on graphite oxidation in buoyant flow [1]. CO and CO_2 spectral features in the midwave infrared (MWIR) were used to infer 2D maps of plume temperature and species concentration. In the previous chapter, this was expanded to cover a wide range of surface temperature conditions ($T_s = 1000 - 4000$ K) and graphite materials. A $[CO]/[CO_2]$ product ratio of $[CO]/[CO_2] = 22 \cdot \exp(-6,000/T_s)$ was observed. A simpli-

fied kinetic transport model was used to interpret experimental observations and infer the relative strengths of kinetic and transport mechanisms.

Although the simplified kinetic model is useful to interpreting experimental trends, it is severely limited due to the over simplification of kinetics and transport mechanisms. This highlights the need for detailed CFD simulations, which not only greatly improve the transport modeling, but can also incorporate complex kinetic rate packages. *CO* oxidation rate packages using a limited number of elementary reactions are already in use [13]. Similar packages for graphite oxidation using a set of semiglobal reactions have also been developed [6]. CFD simulations incorporating these kinetic models have also been demonstrated for graphite oxidation in flat plate shear flow and stagnation flow [8]. However, validation of this work has been difficult due to the lack of spatially resolved experimental data in these flow regimes.

The current study expands on previous experimental work to investigate laser irradiated graphite in a flat plate shear flow using IFTS. This work represents the first spatially resolved measurements of graphite oxidation in a flat plate shear flow, which is vital for validation of numerical work. In addition, flat plate shear flow allows observation of graphite oxidation in a new set of transport conditions. The kinetic transport model used in previous work is again used to interpret experimental observations. Changes in $[CO]/[CO_2]$ product ratio for varying surface temperature and flow rate are discussed.

6.3 Experimental

Overview.

Three graphite materials were each irradiated at 750 and 1500 W/cm² for 120 s to produce steady state surface temperatures of 1000 - 4000 K. Samples were tested at the Wright-Patterson Air Force Base Laser Hardened Materials Evaluation Laboratory (LHMEL) using a 15 kW fiber laser at 1.07 μ m, which produced a 1.4 \pm 0.2 cm diame-

ter (defined as $1/e^2$) beam. Quoted irradiance values are spatially averaged over the beam profile. Irradiance conditions were chosen to observe a wide range of surface temperature conditions, but avoid sublimation.

Experimental procedures were similar to those outlined in a previous study of oxidation in buoyant flow, modified for a flat plate shear flow [88]. A schematic of the experimental set-up is shown in Figure 37. A test section with side and top optical access was mounted at the plenum nozzle exit. Samples were mounted flush with the test section floor, 15 cm downstream of the established flow. Dry air (20% O_2 , < 1% H_2O) was used to establish flows of 5, 7, and 10 m/s. Reynolds number for the 10 m/s case is well below turbulent thresholds ($Re_{turb} > 2 \cdot 10^5$), for both for reacting and non-reacting flow estimates: non-reacting: Re (300 K, 10 m/s) = $7 \cdot 10^4$, reacting: Re (2000 K, 10 m/s) = $3 \cdot 10^3$. Expansion to higher speed laminar flow was limited by boundary layer thickness and the spatial resolution of the instrumentation.

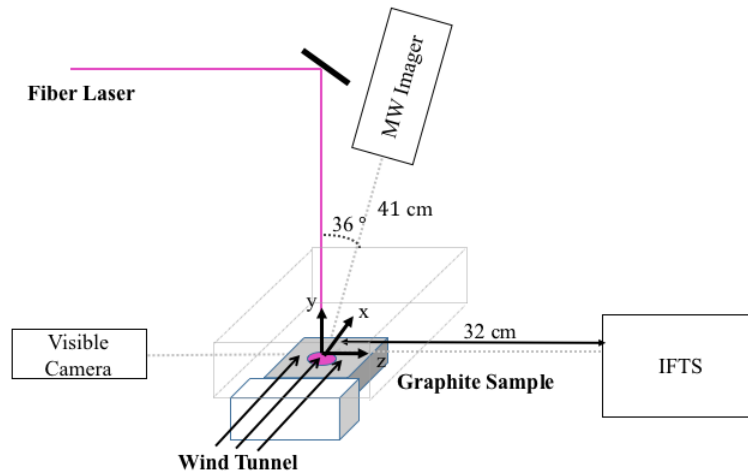


Figure 37. Schematic: laser irradiated graphite in flat plate shear flow.

Materials .

Material properties of the three Graphtek graphite materials are shown in Table 12 [3]. The isomolded and fine samples are produced through an isostatic press and extrusion methods respectively. Impurities found in the ash content are not reported by the manufacturer, but previous work with fine samples report observations of Si, S, Fe, Ca, Al, and K [58]. Additionally these production methods make use of a more reactive binder material, which can react at much lower temperatures, increasing porosity [58, 78]. The pyrolytic material is produced in a layering method, which produces high purity samples with negligible porosity. The layering method results in high conductivity within the layers, but little conductivity between layers. Samples are cut such that the sample surface is a single layer (C-face). Additional details on graphite materials, impurities, as well as sample photographs can be found in [58].

Emissivities provided for the three materials are based on measurements of post irradiated samples [82, 88]. Although graphite emissivities have been previously shown to be relatively insensitive to surface temperature, emissivity can vary significantly by graphite type and surface condition [2]. Emissivities of the isomolded and fine materials are relatively high and increase slightly with surface damage as irradiated (6 – 7%). Previous pyrolytic measurements have shown emissivities to be very anisotropic and sensitive to surface condition. Emissivities of the C-face can vary from 0.54 (undamaged) to 0.58 (irradiated) [88]. Additionally, A-face (layer edge) measurements have shown emissivities as high as 0.90 [88]. Although current measurements are taken normal to the surface (C-face), as the surface is irradiated and layers are eroded, emissivity values may go as high as A-face values.

Table 12. Graphite materials [3]

Material	ID	Emissivity ϵ	Density (g/cm^3)	Particle Size (μm)	Thermal Conductivity ($W/m/K$)	Ash (%)	Sample Size (in)
pyrolytic	PG-SN	0.58 ± 0.05	2.2	NA	$k_{ }$: 400 k_{\perp} : 3.5	-	3x3x1/4
isomolded	GM-10	0.90 ± 0.03	1.82	10.2	83	0.05	3x3x1/2
fine	GR008G	0.93 ± 0.01	1.76	203	130	0.06	3øx1/2

Plume Measurements.

The reacting layer was observed along the z axis using the Telops MWIR hyperspectral imager and Phantom v7 visible high speed camera. The MWIR Telops is an imaging Fourier Transform spectrometer (IFTS) which provides spectral content at each pixel in a 320 by 256 InSb focal plane array (FPA) responsive from 1800-6667 cm^{-1} ($\lambda = 1.5 - 5.5 \mu m$) with a variable spectral resolution of $\Delta \nu = 0.25 - 16 cm^{-1}$. A 2 cm^{-1} spectral resolution was chosen to allow for adequate resolution of CO features. A reduced window size of 64 x 256 was chosen to increase data cube rate (0.75 cubes/s). The 1.5 mrad pixel FOV resulted in a 0.5 mm/pixel spatial resolution. Further detail regarding the MW Telops and its use as a combustion diagnostic can be found in [1, 61, 62].

A simple two layer radiative transfer model (RTM) is used to fit the measured spectra. The measured spectra can be expressed as:

$$L_{det} = \tau_{atmos} \cdot [\epsilon_{plume}(n, X_{i-plume}, T_{plume}, \ell) \cdot B(T_{plume}) + \gamma B(T_{plume})] \quad (131)$$

where L_{det} is the measured spectral radiance, τ_{atmos} is the path transmission, ϵ_{plume} is the plume spectral emissivity, and $B(T_i)$ is the spectral radiance of a blackbody at T_i . The $\gamma B(\nu, T_{plume})$ term was added to account for the background radiance due to soot particles, which is assumed to be wavelength independent. Soot volume fraction is

low, with the $\gamma B(T_{plume})$ term accounting for less than $10 \mu\text{W}/\text{cm}^2/\text{sr}/\text{cm}^{-1}$ of the signal. Assuming equilibrium, emissivity can be written in terms of transmissivity ($\varepsilon = 1 - \tau$), with transmissivity defined by Beer's law:

$$\tau = \exp(-nl \sum_k X_k \sigma_k(\nu, T_{plume})) \quad (132)$$

where n is the number density, l is the path length, X_k is the plume species mole fraction, and σ_k is the species cross-section taken from HITRAN (CO , H_2O) and CDSD 4000 (CO_2) databases [46, 47]. The recent addition of the CDSD 4000 high temperature CO_2 cross-sections has been reported to provide much better agreement with reported CO_2 signatures above 2000 K [1, 63]. A least squares fitting routine on Equation 131 is used to infer T_{plume} , X_{CO} , and X_{CO_2} from the spectral signatures [1, 61]. Uncertainties quoted for plume properties are based on the 95% confidence bounds of the fit and do not include systematic error, such as line of sight averaging and pixel blurring [88]. Full 2D spatial maps of species concentration and plume temperature are inferred by fitting spectra at each pixel. Further detail regarding the use of RTMs in IFTIR combustion work can be found in Reference [62].

Thermal Measurements.

Surface temperatures were measured using the FLIR SC6000 thermal camera equipped with a 620 by 512 FPA sensitive at $3.8\text{-}4.0 \mu\text{m}$. The SC6000 is capable of interweaving multiple integration times in a single test acquisition, allowing for a wider detection range. Thermal measurements were taken using a 2.0 ND filter and integration times of 0.1-1.5 ms, resulting in a noise floor of 500 K. Images were taken at 10 Hz and window size of 128x160 to reduce data volume. The FLIR was mounted 36 degrees off normal to avoid laser path, resulting in vertical and horizontal spatial resolutions of 0.5 and 0.4 mm/pixel respectively. Raw signal is converted to temperature measurements

using an external blackbody (320-870 K) and calibrated using the material emissivities [82]. The largest source of error is the uncertainty in material emissivity. At 3000 K, emissivity uncertainties for the fine and isomolded translate to temperature uncertainties of 20 and 120 K respectively. However due to the low emissivity of the pyrolytic material, emissivity uncertainties are far more problematic, resulting in temperature uncertainties of 3000 ± 1260 K.

6.4 Results and Discussion

Surface Temperature.

Time profiles of peak surface temperature are shown in Figure 38. Surface temperatures show little dependence on flow velocity, which is consistent with thermal modeling efforts which find that radiative cooling and conduction to dominate heat transfer [82]. Observations can be divided between isotropic (fine, isomolded) and anisotropic (pyrolytic) materials. For the isotropic materials, samples are slowly heated, 26 K/s and 80-90 K/s for the low and high irradiance cases respectively, followed by ignition once the samples reached $T_s = 1450 \pm 150$ K. Steady state conditions were reached for all cases within 80 s. For the pyrolytic samples, the low conduction between layers causes a faster heating rate for the surface layer, resulting in heating rates of 180 K/s and 700 K/s for the low and high irradiance cases respectively. Samples ignite quickly ($t < 1$ s) and reach steady state within 20 s. Inferring ignition temperatures from pyrolytic material is difficult to uncertainties in ignition time and the high heating rates.

Temperature uncertainties are based on uncertainties in material emissivity. Surface temperatures for the pyrolytic high irradiance case may be severely overestimated due to the low pyrolytic emissivity and high emissivity uncertainty. Visual inspection of samples post test does not indicate sublimation conditions, suggesting surface temperatures under 3900 K. It is possible that pyrolytic emissivity at higher temperatures rises

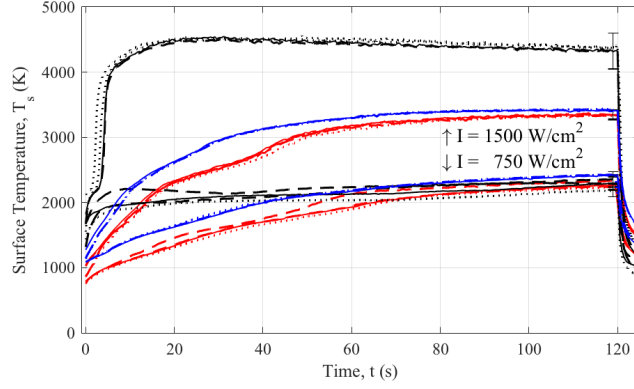


Figure 38. Surface temperatures over time. Material: (—) fine, (—) isomolded, (—) pyrolytic. Flow: (· ·) 5 m/s, (- -) 7 m/s, (- ·) 10 m/s.

and approaches A-face values, which would result in surface temperatures in better agreement with those reported for fine and isomolded samples.

Plume Properties.

Telops hyperspectral data was used to infer plume temperature and species concentration. Plume data is time averaged over the relatively steady region, from $t = 80–100$ s. Sample spectra from a single pixel of a hyperspectral datacube is shown Figure 39. Measured spectra was fit using the RTM given in Eq. (131). The resulting simulated spectra is shown overlayed with measured spectra. Simulation emissivities and path transmission are also shown below. Modeled spectra is in good agreement with measured data, with the exception of the $2250\text{--}2400\text{ cm}^{-1}$ region where path transmission features dominate, highlighting the limitations of the two layer model. Despite these issues, good fits of the fine CO structure and broad CO_2 feature outside of the atmospheric absorption region still allow good estimation of the plume properties (T_{plume} , CO , CO_2).

Full spatial maps are produced by fitting all pixels in the hyperspectral data cube. Plume maps are shown in Figure 40 for a fine sample irradiated at 1500 W/cm^2 with 7 m/s flow. The beam is incident vertically, centered at $x = 0$ with a radius of 7 mm. The

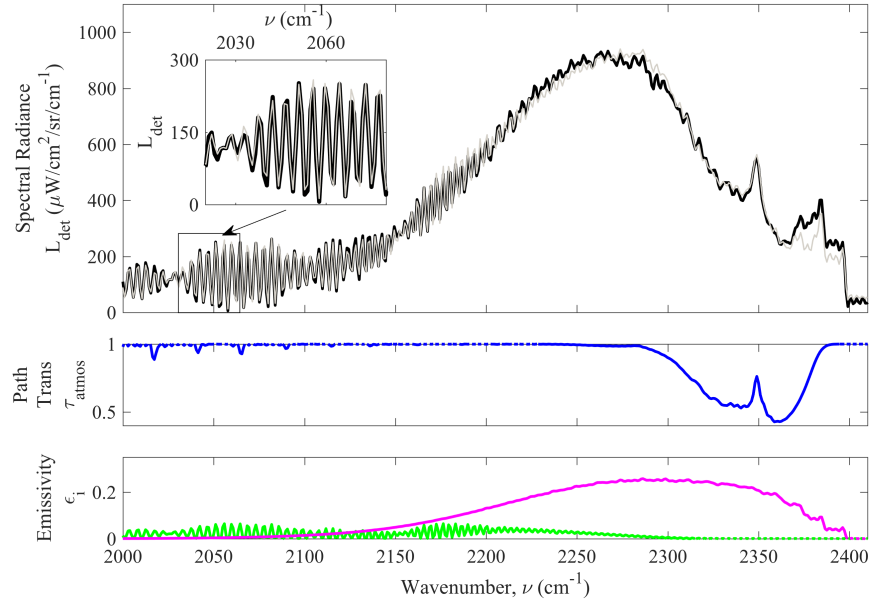


Figure 39. Sample spectra and fit for isomolded sample irradiated at 1500 W/cm with 5 m/s flow². (–) measured radiance, L_{det} , (–) modeled radiance, (–) path transmission, τ_{atmos} , (–) CO emissivity, ϵ_{CO} , (–) CO_2 emissivity, ϵ_{CO_2} . Model fits correspond to $T_{plume} = 2000 \pm 20$ K, $X_{CO_2} = 0.073 \pm 0.001$, $X_{CO} = 0.15 \pm 0.01$.

high temperatures within the beam activates surface oxidation, producing CO at the surface. As the CO diffuses away, it reacts with the available O_2 producing CO_2 , which then is transported downstream. Additional plume maps can be found in Appendix A.

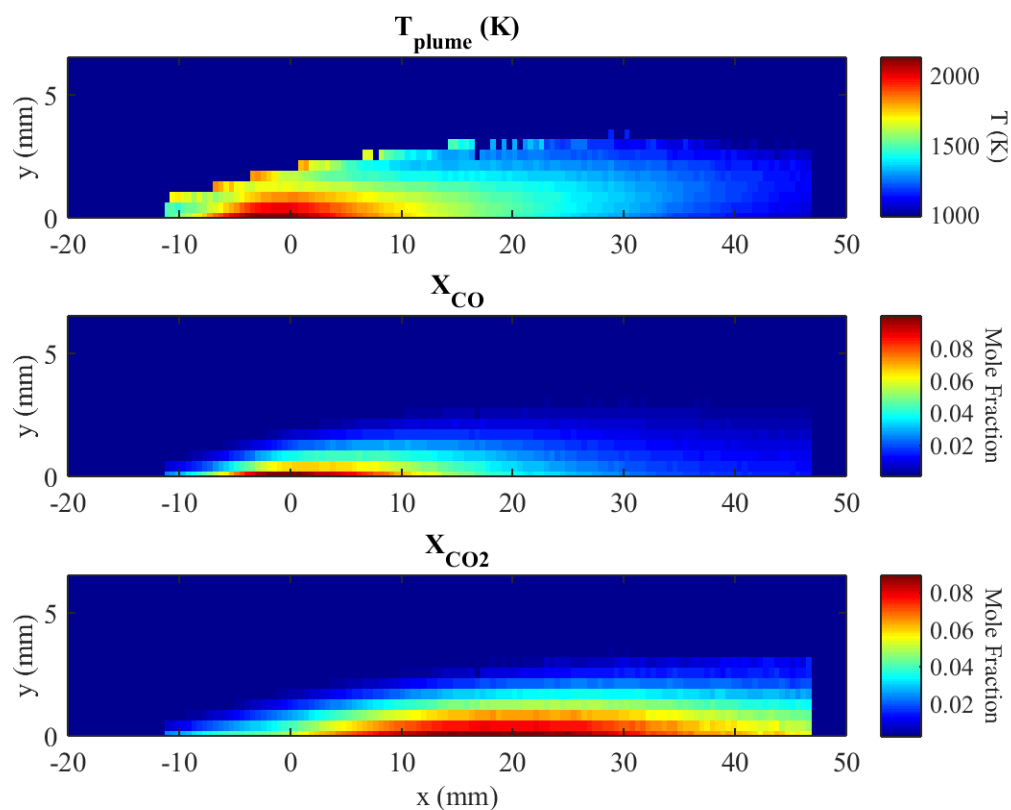


Figure 40. Plume temperature and species mole fractions, X_i , inferred from Telops data, fine sample irradiated at 1500 W/cm² with 7 m/s flow.

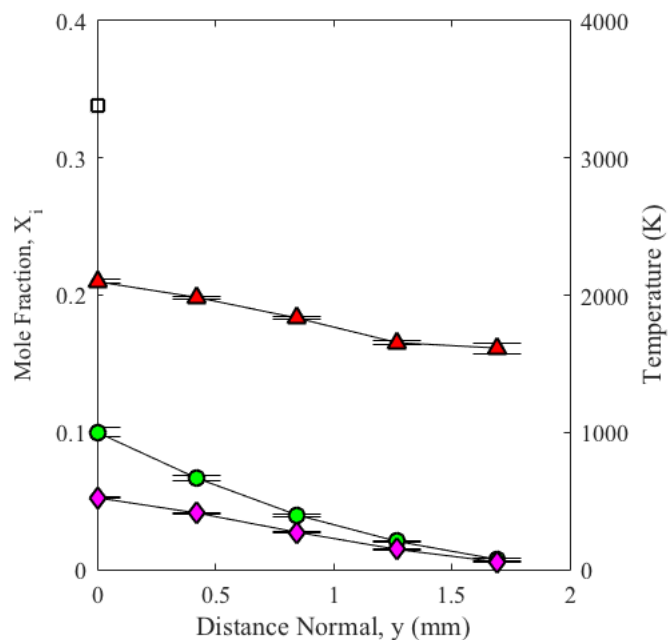


Figure 41. Plume properties normal to the surface at laser center ($x = 0$) for fine samples irradiated at 1500 W/cm² with 7 m/s flow. (●) CO , (◆) CO_2 , (▲) T_{plume} , (X) T_s

Plume properties normal to the surface are shown in Figure 41 evaluated at laser center ($x=0$) for a fine sample irradiated at 1500 W/cm^2 with 7 m/s flow. Error bars reflect the 95% confidence in fit values and do not include systematic error. The CO produced at the surface is consumed in the gas phase reaction as it diffuses from the surface, resulting in a reaction layer of $\delta_R = 1.7 \text{ mm}$. Plume temperature and CO_2 peak at the surface, suggesting sufficient O_2 reaches the surface (attached flame). In the detached flame case, O_2 is depleted before reaching the surface, pushing CO oxidation away from the surface, as indicated by CO_2 and T_{plume} peaking away from the surface.

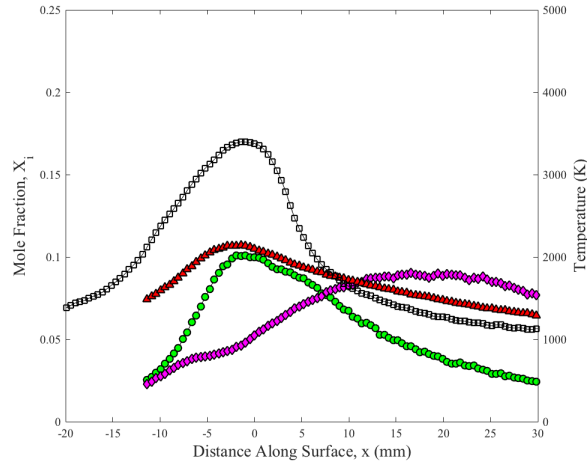


Figure 42. Plume properties along the surface ($x = 0$) for a fine sample irradiated at 1500 W/cm^2 with 7 m/s flow. (●) CO , (◆) CO_2 , (▲) T_{plume} , (□) T_s

Plume properties along the surface are shown in Figure 42 for a fine sample irradiated at 1500 W/cm^2 with 7 m/s flow. Although there is a correlation between plume and surface temperature, they are not in equilibrium, with deviations of 1400 K for the case presented and up to 2000 K for high irradiance pyrolytic cases. The CO concentration is highly correlated to with temperature, peaking at $X_{\text{CO}} = 0.1$. The CO_2 consumption through S2 is visible in the slight dip in CO_2 population near peak surface temperatures.

Farther downstream the CO_2 population grows as CO is oxidized and surface temperatures are sufficiently low to prevent CO_2 depletion though S2. The exothermic CO oxidation heats the downstream portion of the flow, causing asymmetry.

Irradiance Effects.

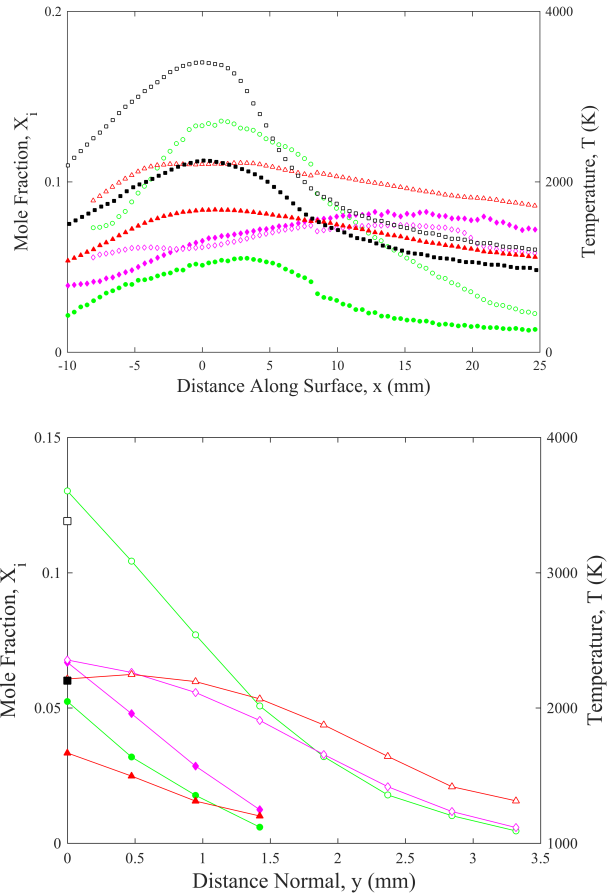


Figure 43. Plume properties along the surface (top) and normal to surface (bottom) for a fine sample irradiated at 750 W/cm² (solid) and 1500 W/cm² (open) with 5 m/s flow. Markers: (●) CO , (◆) CO_2 , (▲) T_{plume} , (■) T_s

A comparison of low and high irradiance cases of fine samples in 5 m/s flow is shown in Figure 43. The most obvious result of the increase in irradiance is the increase in

T_s profile, which increases by 1100 K. The increase in surface temperature increases surface oxidation, increasing the CO population from peak mole fractions of 0.05 to 0.13. The increase in CO at the surface creates a thicker diffusion region, increasing δ_R . The thicker diffusion region restricts O_2 from the surface. The lack of surface O_2 cause the gas phase oxidation rate to peak a few mm off the surface, as evident by the T_{plume} peak at 0.5 mm. Despite the higher CO population, little rise in CO_2 is seen due to the lack of O_2 available to oxidize the CO . The slightly negative slope of CO_2 at the surface implies diffusion flux of CO_2 away from the surface $\Gamma_{d-y} = -D \left(\frac{dCO_2}{dy} \right)_s$, suggesting some O_2 is still available at the surface to produce CO_2 . In the case of $(O_2)_s = 0$, CO_2 would purely be consumed at the surface due to the S2 reaction, resulting in a diffusion flux of CO_2 towards the surface, indicated by a positive slope in the species profile, $\left(\frac{dCO_2}{dx} \right)_s > 0$.

The $[CO]/[CO_2]$ ratio as a function of temperature for fine samples irradiated at 750 and 1500 W/cm² at 5 m/s flow rates is shown in Figure 44. Little difference is seen between the low and high irradiance cases, with only a slightly upward shift in $[CO]/[CO_2]$ for the higher irradiance case. One possible reason for the upward shift may be increased reaction layer thickness. The higher irradiance case produces a thicker reaction region, which prevents O_2 from reaching the surface. The $[CO]/[CO_2]$ ratio is generally believed to have a negative O_2 dependence. So the decrease in O_2 at the surface would result in an increase in $[CO]/[CO_2]$.

Flow Effects.

A comparison of fine samples irradiated at 750 W/cm² with flow speeds of 5 and 10 m/s is shown in Figure 45. Similar surface temperature profiles were observed for the two flow speed cases due to the relatively low contribution of convective cooling. The increase in flow speed results in a decrease in boundary layer thickness, decreasing the reaction layer thickness. CO population is reduced due to higher diffusion losses. The

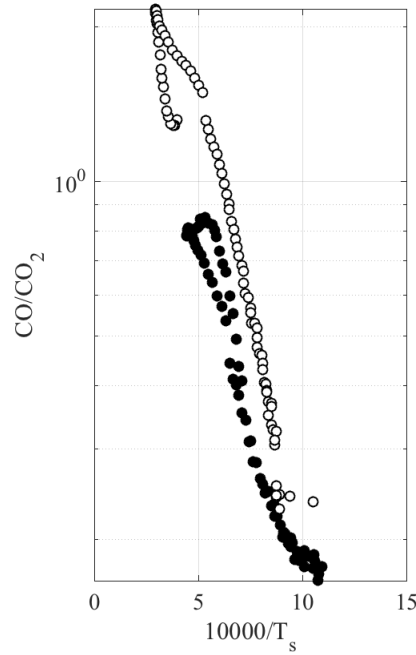


Figure 44. $[CO]/[CO_2]$ vs T_s evaluated at surface for fine samples irradiated at 750 W/cm^2 (●) and 1500 W/cm^2 (○) with flow speeds of 5 m/s

thinner reaction layer also allows more O_2 to reach the surface, lowering the $CO : O_2$ ratio and decreasing the T_{plume} . The CO_2 production is also decreased due to the lower CO availability for oxidation.

The $[CO]/[CO_2]$ ratio as a function of temperature for isomolded samples irradiated at 1500 W/cm^2 at 5 m/s and 10 m/s flow rates is shown in Figure 46. Higher $[CO]/[CO_2]$ values are observed for the higher flow rate case. Although both CO and CO_2 decrease with increasing flow speeds, the losses to CO_2 are slightly higher, causing a slight increase in $[CO]/[CO_2]$ ratio.

$[CO]/[CO_2]$ Temperature Dependence.

$[CO]/[CO_2]$ for all test cases is shown in Figure 47. In the lower temperature region, $1250 - 2500 \text{ K}$, each test case shows similar apparent activation energies with β values ranging from $2220 - 3460 \text{ K}$. Slight differences between materials is noted, with iso-

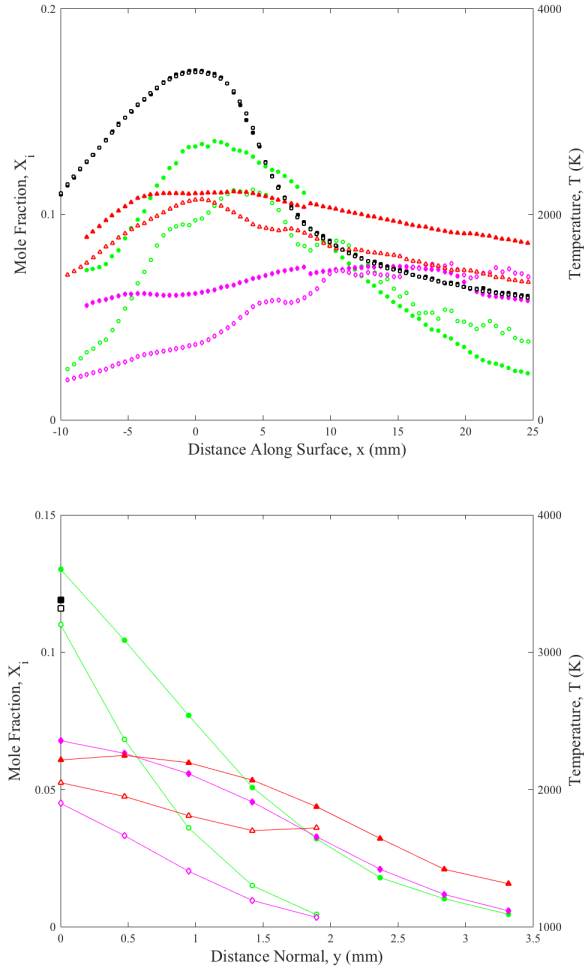


Figure 45. Plume properties along the surface (top) and normal to surface (bottom) for a fine sample irradiated at 750 W/cm^2 for $V = 5 \text{ m/s}$ (solid) and 10 m/s (open). Markers: (●) CO , (◆) CO_2 , (▲) T_{plume} , (■) T_s

molded exhibiting higher $[CO]/[CO_2]$ ratios for a given temperature. This is due mainly to higher isomolded CO populations for a given T_s . Combining data across materials in Figure 47, a general trend of:

$$\frac{CO}{CO_2} = (7.8 \pm 1.3) \exp\left(\frac{-3130 \pm 310}{T_s}\right) \quad (133)$$

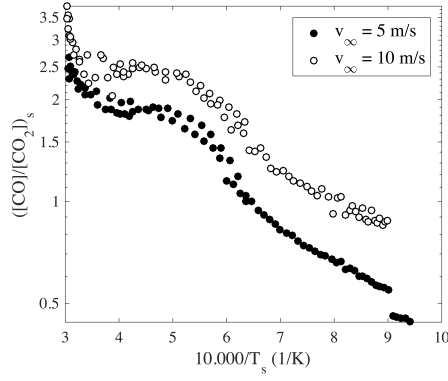


Figure 46. $[CO]/[CO_2]$ vs T_s evaluated at surface for isomolded samples irradiated at 1500 W/cm^2 with flow speeds of 5 m/s (●) and 10 m/s (○)

is observed. Values for β are consistent with values reported by Walker, Tognotti, Du, and Otterbien [21, 39, 40, 42], but significantly lower than those reported for buoyant flow ($\beta = 6000 \text{ K}$).

6.5 Model

Rate Equations.

A simplified, diffusion kinetic model is developed to further interpret the current observations. Applying the species conservation equations to a small control volume adjacent to the surface, the following rate equations are obtained (see Chapter III):

$$\left(\frac{dC_i}{dt} \right)_s = \omega_i + v_s \frac{dC_i}{dy} - \frac{1}{\Delta x} [\omega_s - \Gamma_i] \quad (134)$$

where ω_i is the reaction source term, $v_s \frac{dC_i}{dy}$ is the convective transport term assuming velocity $v = (0, v_s)$, ω_s is the surface reaction source term, Γ_i is the diffusion flux term, and Δx is the width of the control volume. Diffusion flux is assumed to be mainly in the x direction due to the strong concentration gradient normal to the surface, $\frac{dC_i}{dx} > \frac{dC_i}{dy}$. Applying Eq. (134) to the three species of interest, the following rate equations are

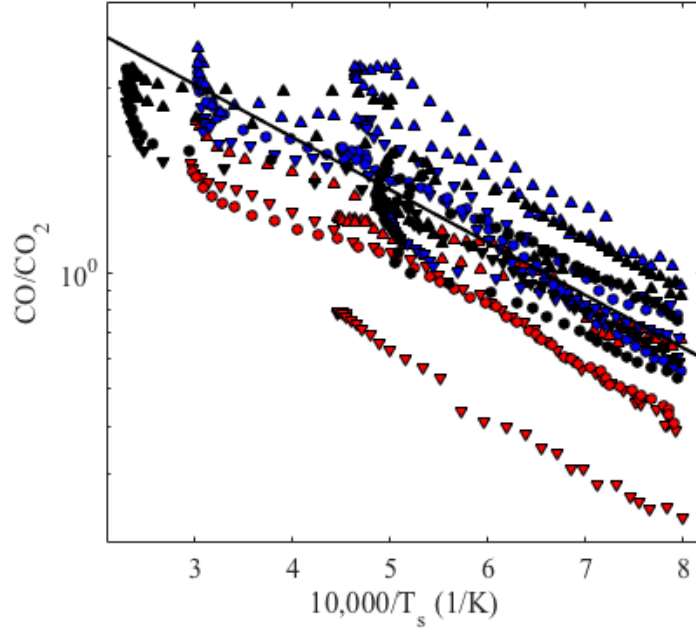


Figure 47. $[CO]/[CO_2]$ vs T_s evaluated at surface for all test cases. Material: (●) fine, (●) isomolded, (●) pyrolytic. Flow: (▽) 5 m/s, (○) 7 m/s, and (△) 10 m/s. Fit: (—) $[CO]/[CO_2] = 7.8 \exp(-3130/T_s)$

obtained:

$$\left(\frac{d[O_2]}{dt} \right)_s = -\frac{1}{2}R_g + v_s \frac{d[O_2]}{dy} + \frac{1}{\Delta x} [-R_{s1} - R_{s3} - \Gamma_{O_2}] \quad (135)$$

$$\left(\frac{d[CO]}{dt} \right)_s = -R_g + v_s \frac{d[CO]}{dy} + \frac{1}{\Delta x} [2R_{s1} + 2R_{s2} - \Gamma_{CO}] \quad (136)$$

$$\left(\frac{d[CO_2]}{dt} \right)_s = R_g + v_s \frac{d[CO_2]}{dy} + \frac{1}{\Delta x} [-R_{s2} + R_{s3} - \Gamma_{CO_2}] \quad (137)$$

where the rates, R_g is the gas phase reaction rate assumed to be of the the form:

$$R_g = A_g [O_2]^{0.2} [CO] \exp \left(-\frac{E_g}{T_{plume}} \right) \quad (138)$$

and R_{si} are the surface reaction rate assumed to be first order Arrhenius. Due to the non-equilibrium between gas and surface temperatures at the surface, a modified expression for k_i was chosen to reflect the surface reaction dependence on plume and

surface temperature using a temperature mixing coefficient, ϕ :

$$k_i = A_i \exp\left(-\frac{E_i}{\phi_i T_s - (1 - \phi_i) T_p}\right) \quad (139)$$

To reduce the species conservation equations into a simplified ODE, the following approximated diffusion flux is proposed:

$$\Gamma_i(j) = \begin{cases} -\frac{D_i}{\delta_d} [C_i^o - C_i(j, 1)] & i = CO, O_2 \\ 0 & i = CO_2 \end{cases} \quad (140)$$

where δ_d is a length scale on the order of the flame width, and C_i^o is the freestream concentration of species i . The CO_2 flux is assumed negligible compared to O_2 and CO flux.

Combining Eq. (135) - (140) and assuming steady state, results in a system of three first order ODEs. Boundary conditions are provided by the upstream conditions, which are assumed to be the free stream values ($X_{O_2}^o = 0.2$, $X_{CO}^o = 0$, and $X_{CO_2}^o = 0$). Due to nonlinearity and the coupling of the ODEs, a numerical solver is used. A nonlinear least squares fitting routine is used to determine reaction rate parameters necessary for agreement between simulated CO and CO_2 profiles and experimental observations. Surface reaction rates are controlled through fitting of A_i and E_i , which were allowed to vary from sample to sample. Gas phase reaction rates were controlled through fitting of A_g , which was then fixed based on best fit of the six test cases.

Model Results.

A nonlinear least squares fitting routine was used to fit kinetic rate parameters to achieve agreement between observed and simulated CO and CO_2 surface profiles. Model results for an isomolded sample irradiated at 1500 W/cm^2 with 7 m/s flow are

shown in Figure 48 with simulation parameters provided in Table 13. Kinetic and transport rates (middle panel) were inferred using observed temperature profiles, shown at the top of the figure, and the rate parameters shown in Table 13. The gas phase oxidation rate is scaled by Δx for unit agreement. The bottom of Figure 48 shows the measured CO and CO_2 surface profiles as well as simulated CO , CO_2 and O_2 profiles. Good agreement is found between simulated and measured profiles with a normalized root mean squared error (NRMSE) of 9%.

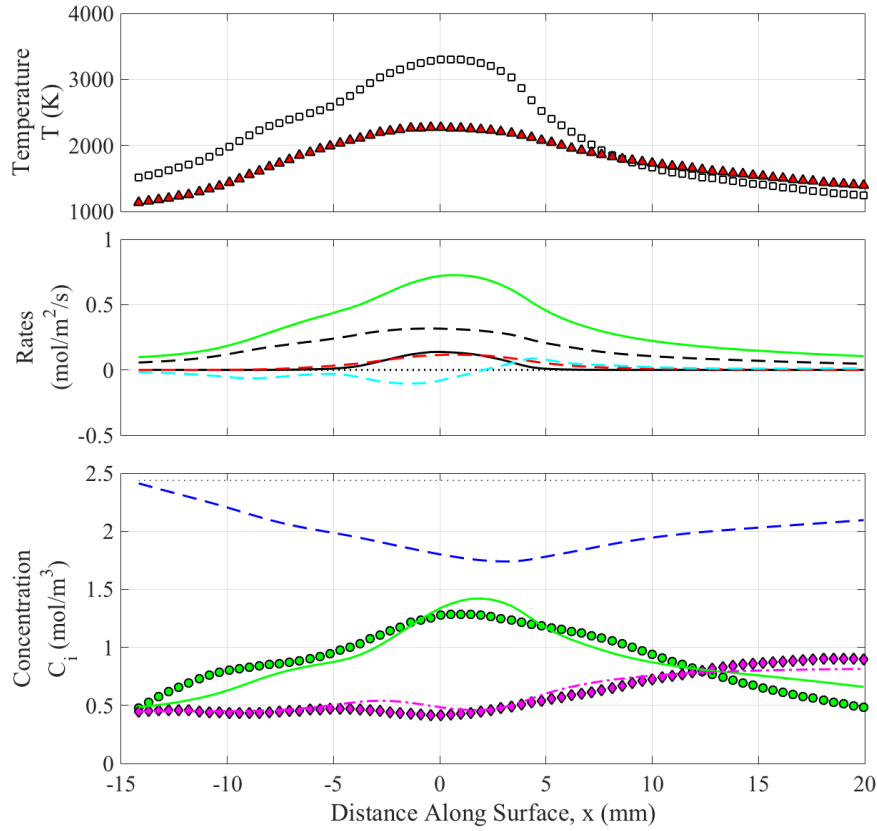


Figure 48. Sample model fitting for an isomolded sample irradiated at 1500 W/cm^2 with 7 m/s flow. Top: temperature measurements - (\blacktriangle) T_{plume} , (\square) T_s . Middle: simulated rates - (—) CO diffusion flux, Γ_{d-CO} , (---) CO net convection flux $\Delta\Gamma_{c-CO}$, (- -) CO oxidation rate $\Delta x R_g$, (- -) R_1 , (—) R_2 , Bottom: Species concentrations - Measurements: (\bullet) CO , (\blacklozenge) CO_2 , Model: (—) CO , (- -) CO_2 , (---) O_2 , (..) O_2^o

Table 13. Simulation parameters.

parameter	value	units
A_1 (S1) pre-exponential	1	m/s
A_2 (S2) pre-exponential	600	m/s
E_1 (S1) activation energy	5400	K
E_2 (S2) activation energy	20300	K
A_g (G) pre-exponential	$2 \cdot 10^5$	$(\text{mol}/\text{m}^3)^{-0.2} \text{ 1/s}$
E_g (G) activation energy	15,100	K
δ_d diffusion length scale	2-3	mm
v_s surface velocity	1-2	m/s

Results suggest CO production is dominated by the S1 reaction, contributing to 70% of CO production. CO transport is dominated by diffusion away from the surface due to the strong gradient, with slight contributions from convective transport. CO is then mainly controlled by the balance between S1 CO production and diffusion losses. In the case of CO_2 , the S2 surface consumption is found to be balanced by production through the gas phase reaction, with little contribution from transport terms.

Non-uniqueness.

While the presented model is useful in interpreting observations, limitations due to non-uniqueness should be noted. Given the large number of model fit parameters and wide range of possible values in literature, several fit solutions are possible. Central to this issue is the choice of gas phase reaction pre-exponential factor A_g , which in turn determines all other rate parameters. The balance of R_g and R_{s-2} implies that choice of A_g controls S2 parameters. Since the CO production is limited, choice of S2 then determines S1. Choice of A_g then dictates all other rate parameters. Since A_g varies by orders of magnitude in literature, this can lead to a large degree of uncertainty in surface reaction parameters.

6.6 Conclusions

We presented the first spatially resolved graphite oxidation measurements in a flat plate shear flow using IFTS. The oxidation of laser irradiated graphite in a reacting flow has been observed for three graphite materials at irradiances of 750 and 1500 W/cm² and freestream velocity of 5, 7, and 10 m/s. $[CO]/[CO_2]$ data is presented for varying material, irradiance, and freestream velocity with a general trend of $[CO]/[CO_2] = (7.8 \pm 1.3) \exp(-3130 \pm 310/T_s)$.

A simple model incorporating transport and kinetics is presented to interpret experimental observations. Increase in T_s results in an increase in CO due to increased surface reactivity, increasing the diffusion length. Higher T_s also decreases CO_2 due to increasing consumption from the S2 reaction, as observed by the dip in CO_2 near laser center. Downstream of laser center, the loss in CO_2 due to surface oxidation is offset by the CO to CO_2 conversion, resulting in an increase in CO_2 profiles. Increasing v_∞ results in a decrease in δ_R , likely due to a decrease in boundary layer thickness. The decrease in diffusion length leads to higher CO diffusion losses, decreasing CO population. This results in a decrease in CO_2 production in the gas phase, lowering the CO_2 population.

Relative strengths of kinetic and transport mechanisms are determined using a least squares fit of species profiles along the surface. Results suggest that CO population is determined by the balance between production at the surface, predominantly through the S1 reaction, and diffusion losses. For CO_2 , transport terms are negligible, leading to a balance between CO_2 consumed at the surface through S2 and produced through CO oxidation in the gas phase. Although general trends for CO and CO_2 surface profiles can be observed using the simplified model, it is difficult to perfectly replicate experimental results, likely due to the overly simplified kinetic and transport models. Full 2D simulations are necessary to gain a full picture of kinetic-transport coupling.

This highlights the necessity of CFD simulations which can not only greatly improve transport modeling, but can also incorporate complex kinetic rate packages.

VII. Imaging Fourier Transform Spectroscopy of Graphite Oxidation in a Stagnation Flow

This chapter focuses on characterizing graphite oxidation in stagnation flow using IFTS, in partial fulfillment of objective 1. The chapter is written in journal article format and can be read independently as a stand alone document. Additional details regarding background and experimental method can be found in Chapter II and IV, respectively.

7.1 Abstract

The oxidation of laser irradiated graphite in stagnation flow is characterized using imaging Fourier transform spectroscopy (IFTS). Graphite cone samples were placed in a 1.5 m/s dry (20% O_2 , < 1% H_2O) stagnation flow and irradiated at 650, 900, and 2400 W/cm², producing surface temperatures of up to 3100 K. The resulting reacting layer is observed using a midwave (MW) IFTS at 2 cm⁻¹ spectral resolution, 0.5 mm/pixel spatial resolution, and 0.75 Hz data cube rate. A cross-correlation technique for inferring velocity maps from IFTS imagery is demonstrated. Plume temperature, CO , and CO_2 concentrations are inferred from the IFTS spectral data. Temporal variations in the CO and CO_2 populations suggest some inhibition of the $C_s - CO_2$ reaction with increasing CO population. $[CO]/[CO_2]$ trends at lower temperatures compare favorably with previously reported values, with a general trend of: $[CO]/[CO_2] = 2 \exp(-2400/T_s)$. At higher temperatures, these trends transition to higher effective activation energies of 16,000 and 31,000 K. This transition coincides with the decline in CO_2 due to the $C_s - CO_2$. Additional data is needed to characterize the $C_s - CO_2$ reaction and its dependence on CO and T_s . This data set represents the first spatially resolved measurements of graphite oxidation in a flat plate shear flow.

7.2 Introduction

Although carbon oxidation has been studied extensively, much is still not understood regarding the coupling of kinetics and transport mechanisms. Carbon oxidation can be simplified to the reactions shown in Table 14. The CO produced at the surface through S1 and S2 is converted to CO_2 as it diffuses away from the surface. A portion of the CO_2 then diffuses back to the surface to supply the S2 reaction. The CO oxidation in the reacting layer then controls the oxidizing species available at the surface through consumption of O_2 and production of CO_2 . Accurately predicting carbon oxidation then requires detailed knowledge of CO and surface oxidation mechanisms as well as mass transport.

Table 14. Oxidation mechanisms

	Reaction
(G)	$CO + 1/2 O_2 \Rightarrow CO_2$
(S1)	$2C_s + O_2 \Rightarrow 2CO$
(S2)	$C_s + CO_2 \Rightarrow 2CO$

Imaging Fourier transform spectroscopy (IFTS) has recently been demonstrated as a useful tool to characterize graphite oxidation in a reacting flow [1]. CO and CO_2 spectral features in the midwave infrared (MWIR) were used to infer 2D maps of plume temperature and species concentration. Combined with surface temperature measurements using MWIR imagery, this technique allows full spatial characterization of the oxidizing surface and reacting plume. These species maps provide unique insight into how species are formed and transported from the surface. In the previous chapters, IFTS was used to characterize graphite oxidation in buoyant flow and flat plate shear flow for varying surface temperatures ($T_s = 1000\text{--}4000\text{ K}$) and graphite materials. Similar trends

in species population were observed for both flow cases. CO population was found to be highly correlated with surface temperature as a result of the S1 and S2 surface reactions. A decline in CO_2 population was observed near laser center due to the S2 reaction.

Carbon oxidation studies are often presented in terms of $[CO]/[CO_2]$ product ratio, typically expressed as:

$$\frac{[CO]}{[CO_2]} = \alpha \exp\left(-\frac{\beta}{T_s}\right) \quad (141)$$

where α and β are found to vary significantly across literature due to differences in material composition and test conditions (see Chapter II). In the case of buoyant flow, little difference in $[CO]/[CO_2]$ was seen across materials, with a general trend of $[CO]/[CO_2] = 22 \cdot \exp(-6,000/T_s)$. Similarly for flat plate shear flow, a general trend of $[CO]/[CO_2] = 8 \cdot \exp(-3,100/T_s)$ was observed. These studies were conducted using identical materials over similar temperature ranges, suggesting that differences in $[CO]/[CO_2]$ trends are a result of variations in transport effects between the two flow conditions. Although β values for buoyant and flat plate shear flow are within the range typically observed in literature ($\beta = 3,020 - 7,200$ K) [21, 37–42], these deviate significantly from those reported by Acosta ($\beta = 18,000$ K) for similar surface temperatures and material[1]. This variation in β values may be due differences in the evaluation of $[CO]/[CO_2]$. In the Acosta study, product ratios were evaluated at a single spatial point over the transient heating period, or $([CO]/[CO_2])(t)$ vs $T_s(t)$. Whereas in recent work, $[CO]/[CO_2]$ was evaluated at steady state using the spatial distribution, or $([CO]/[CO_2])(x)$ vs $T_s(x)$. Ideally, this would be confirmed by comparison of the transient response for both data sets. However the high heating rates for the more recent data sets prevent characterization during the transient period.

The current study focuses on characterizing laser irradiated graphite in a stagnation flow using IFTS. Graphite samples are irradiated in stagnation flow ($v = 1.5$ m/s) to

surface temperatures of up to 3100 K. Lower heating rates are used to allow for characterization of transient CO and CO_2 populations. Differences in $[CO]/[CO_2]$ concentration ratios across the three flow conditions (buoyant flow, flat plate shear flow, and stagnation flow) are discussed. This data set represents the first spatially resolved measurements of graphite oxidation in stagnation flow.

7.3 Experimental

Overview.

A schematic of the experimental set-up is shown in Figure 49. Samples were tested at the Wright-Patterson Air Force Base Laser Hardened Materials Evaluation Laboratory (LHMEL) using a 15 kW fiber laser at $1.07\ \mu\text{m}$, which produced a 1.3 cm diameter beam, where beam area, A_b , is defined as containing 86% of laser power. Samples were irradiated at 660 and $900\ \text{W}/\text{cm}^2$ until reaching surface temperatures of up to 2500 K. Quoted irradiance values are spatially averaged over the beam profile ($I = \text{Power}/A_b$).

Stagnation flow was established using a 2.5 cm diameter nozzle, designed to produce a flat top exit flow. A 1.5 m/s dry air ($< 2\% H_2O$) flow was established over the 6 in diameter cone test samples, creating a 3D stagnation flow with stagnation velocity gradient, $B = 3v_\infty/d = 30\ \text{s}^{-1}$ (v_∞ - flow velocity, d - sample diameter).

Graphite Samples .

Graphite samples were fine grade Graphtek GR008G samples which are produced through an extrusion method. Material properties are outlined in Table 15 [3]. Impurities found in the ash content are not reported by the manufacturer, but previous work report observations of Si, S, Fe, Ca, Al, and K [58]. Emissivities included are based on measurements of post irradiated samples [82]. Samples were machined into an ogive

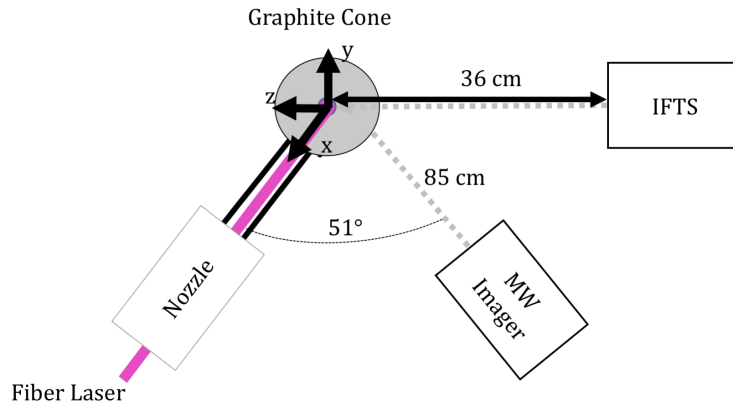


Figure 49. Schematic: laser irradiated graphite in stagnation flow

cone. Cones were machined from 6 in diameter and 2 in long cylinders. The cone surface was 4 mm in height, resulting in a gentle slope of less than 3°.

Table 15. Graphite properties [3]

Property	Value	Units
Emissivity	0.93 ± 0.01	
Density	1.76	g/cm^3
Particle Size	203	μm
Thermal Conductivity	130	W/m/K
Ash Content	0.06	%

Thermal Measurements.

Surface temperatures were measured using the FLIR SC6000 thermal camera equipped with a 620 by 512 FPA sensitive at 3.8-4.0 μm . The SC6000 is capable of interweaving multiple integration times in a single test acquisition, allowing for a wider detection range. Thermal measurements were taken using a 2.0 ND filter and integration times

of 0.1-1.5 ms, resulting in a noise floor of 500 K. Images were taken at 10 Hz and window size of 128x160 to reduce data volume. The FLIR was mounted 51 degrees off normal to avoid laser path, resulting in vertical and horizontal spatial resolutions of 0.8 and 1.2 mm/pixel respectively. Raw signal is converted to temperature measurements using an external blackbody (320-870 K) and calibrating using the material emissivities [82]. The largest source of error is the uncertainty in material emissivity, which can lead to a temperature uncertainties of 3000 ± 20 K.

Plume Measurements.

The reacting layer was observed along the z axis using the Telops MWIR hyperspectral imager and Phantom v7 visible high speed camera. The MWIR Telops is an imaging Fourier Transform spectrometer (IFTS) which provides spectral content at each pixel in a 320 by 256 InSb focal plane array (FPA) responsive from $1800\text{-}6667\text{ cm}^{-1}$ ($\lambda = 1.5 - 5.5\text{ }\mu\text{m}$) with a variable spectral resolution of $\Delta\nu = 0.25 - 16\text{ cm}^{-1}$. A 2 cm^{-1} spectral resolution was chosen to allow for adequate resolution of CO rotational features. A reduced window size of 64×256 was chosen to increase data cube rate (0.75 cubes/s). The 1.4 mrad pixel FOV resulted in a 0.5 mm/pixel spatial resolution. Further detail regarding the MW Telops can be found in [61, 64, 79–81].

A simple two layer radiative transfer model (RTM) is used to fit the measured spectra. The measured spectra can be expressed as:

$$L_{det} = \tau_{atmos} \cdot [\epsilon_{plume}(n, X_{i-plume}, T_{plume}, \ell) \cdot B(T_{plume}) + \gamma B(T_{plume})] \quad (142)$$

where L_{det} is the measured spectral radiance, τ_{atmos} is the path transmission, ϵ_{plume} is the plume spectral emissivity, and $B(T_i)$ is the spectral radiance of a blackbody at T_i . The $\gamma B(\nu, T_{plume})$ term was added to account for the background radiance due to soot particles, which is assumed to be wavelength independent. Soot volume fraction is

low, with the $\gamma B(T_{plume})$ term accounting for less than $10 \mu\text{W}/\text{cm}^2/\text{sr}/\text{cm}^{-1}$ of the signal. Assuming equilibrium, emissivity can be written in terms of transmissivity ($\varepsilon = 1 - \tau$), with transmissivity defined by Beer's law:

$$\tau = \exp(-nl \sum_k X_k \sigma_k(\nu, T_{plume})) \quad (143)$$

where n is the number density, l is the path length, X_k is the plume species mole fraction, and σ_k is the species cross-section taken from HITRAN (CO , H_2O) and CDSD 4000 (CO_2) databases [46, 47]. A least squares fitting routine of Eq. (??) is used to infer plume and atmospheric properties (T_{plume} , X_{CO} , X_{CO_2} , $X_{\text{atmos-CO}_2}$) from the measured spectral signatures [1, 61].

Visualization of the flow was achieved using the low frequency component of the IFTS interferograms. Interferograms are low pass filtered, removing any spectral content in the signal. The filtered signal is then cross-correlated with neighboring pixels to determine the signal delay, τ . Velocities are then estimated by $v = \Delta x / \tau$ where Δx is the pixel spatial resolution. A full velocity map is then achieved by repeating at all pixel locations, with horizontal and vertical pixel pairs used to determine x and y components of the velocity vector.

7.4 Results and Discussion

Surface Temperature.

Samples were heated at irradiances of 650, 900, and $2400 \text{ W}/\text{cm}^2$. Time profiles of peak surface temperature are shown in Figure 50. Once irradiated, the samples are heated with rates of 16, 20, and $113 \text{ K}/\text{s}$ for low, medium, and high irradiance respectively. Due to the large mass of the samples, equilibrium is not reached over the test duration. Final surface temperatures of 2340, 2500, and 3090 K are reported for the low, medium,

and high irradiance cases respectively. Temperature uncertainties are estimated based on emissivity uncertainty (0.93 ± 0.01). The resulting temperature uncertainties increase with surface temperature, with a peak uncertainty of 20 K estimated for $T_s = 3000$ K surface.

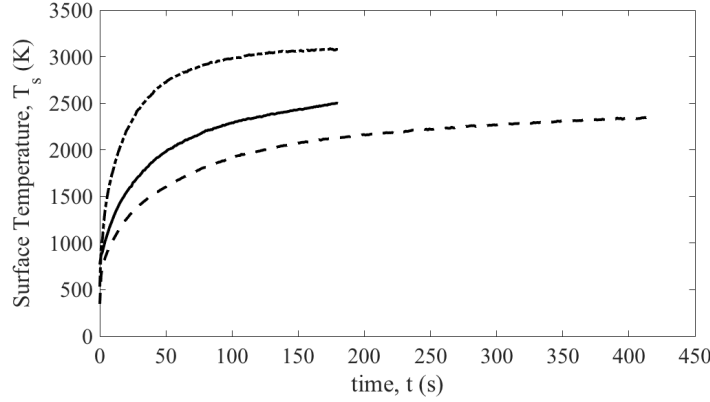


Figure 50. Surface temperatures over time at irradiances of: (- -) 650 W/cm²; (-) 900 W/cm²; (- . -) 2400 W/cm².

Flow.

Flow maps are achieved using the low frequency oscillations observed in the IFTS interferograms. A sample interferogram is shown in Figure 51 (a) for a pixel within the stagnation region. The low frequency oscillations are clearly visible on top of the interference pattern. A fast Fourier transform (FFT) of the signal is shown in Figure 51 (b). Middle frequencies (20% - 40% of the Nyquist frequency, f_N) of the FFT contain the spectral content of the signal. Lower frequencies, $< 5\% f_N$, are due to oscillations in the flow and changes in radiance due to intermittent particle ejection. Flow maps are achieved by using the low frequency oscillations to infer flow patterns. Interferograms are low pass filtered, $f < 5\% f_N$, removing any spectral content in the signal. Cross-

correlation of neighboring pixels then gives the delay due to flow travel time between pixels, from which flow velocity can be inferred.

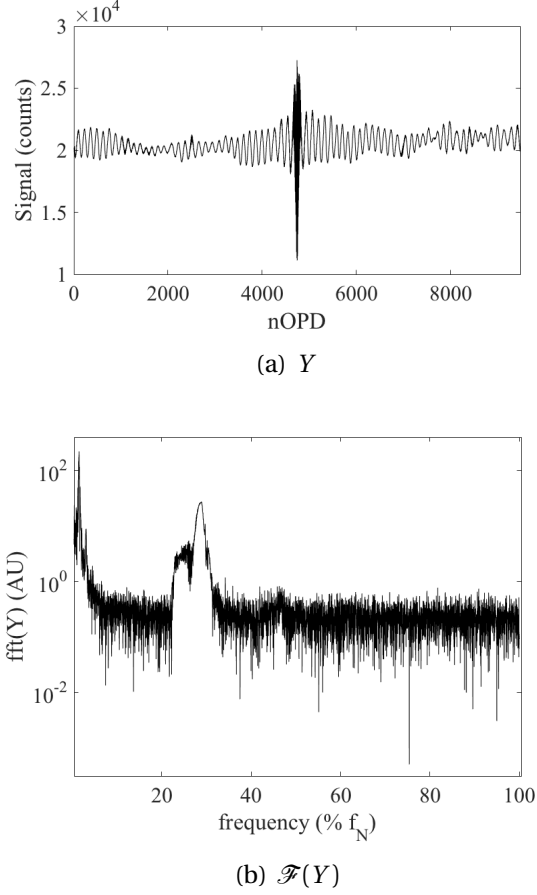


Figure 51. Sample interferogram, Y , and FFT, $\mathcal{F}(Y)$.

The resulting flow map for a 1.5 m/s stagnation flow on a sampled irradiated at 2400 W/cm^2 is shown in Figure 52. A broadband image is included in the background for spatial reference. Length and direction of vectors indicate velocity magnitude and direction. Velocities inferred at the edge of the stagnation region ($v = (-3, 3) \text{ m/s}$) are higher than nozzle flow exit velocities measured using an anemometer ($v = -1.5 \text{ m/s}$). However anemometer measurements may have been underestimated due to issues

coupling the anemometer to the nozzle exit. Within the stagnation region, the flow deviates from an ideal stagnation flow due to buoyancy effects, as evident by the upward movement of the plume below centerline. A stagnation region is visible approximately 1 mm away from the surface. This is consistent with current modeling approach which models graphite oxidation in stagnation flow as a counterflow problem [8]. In this case, surface oxidation products are modeled as being ejected from the surface, creating a stagnation plane as it interacts with the incoming flow.

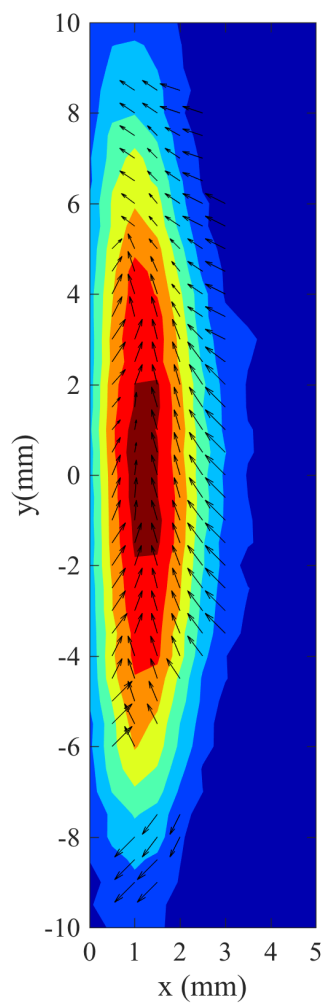


Figure 52. Velocity field for stagnation flow ($v=1.5$ m/s) on sample irradiated at 2400 W/cm^2 . Broad-band image in background included for spatial reference.

Plume.

Species and temperature maps are inferred using from the spectral content of the data. A sample plume maps is shown in Figure 53 for a sample irradiated at $I = 900$ W/cm² for 100 s, resulting in a peak surface temperature of $T_s = 2290$ K. The beam is incident horizontally, centered at the peak of the cone at $y = 0$ with a radius of 0.7 cm. The high surface temperatures within the beam cause any available oxidizer (O_2 , H_2O , CO_2) to react with the surface, producing CO . The CO diffuses away from the surface and reacts with the available O_2 , creating CO_2 . CO and CO_2 mole fractions are significantly lower than observed in the flat plate shear flow ($X_{CO} = 0.05$, $X_{CO_2} = 0.07$ at $T_s = 2250$ K) or buoyant flow ($X_{CO} = 0.16$, $X_{CO_2} = 0.13$ at $T_s = 2245$ K) cases for similar surface temperatures. This may be result of higher diffusional losses due to the thin reacting layer.

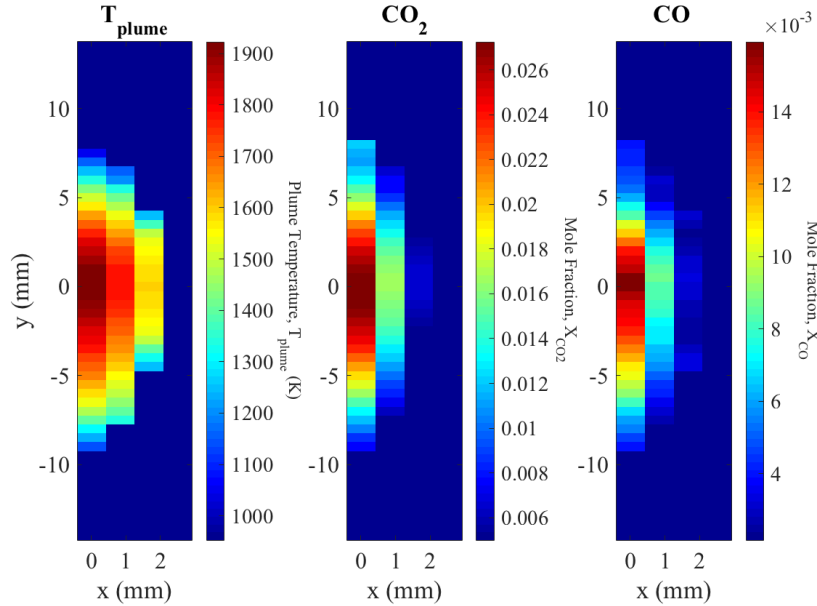
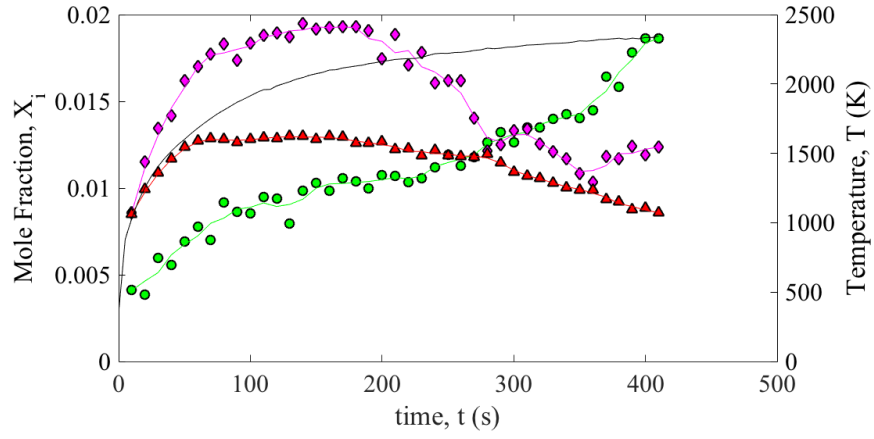
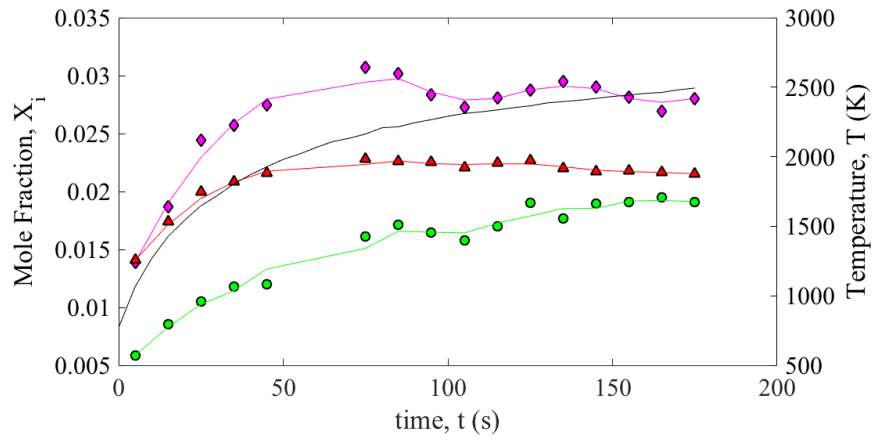


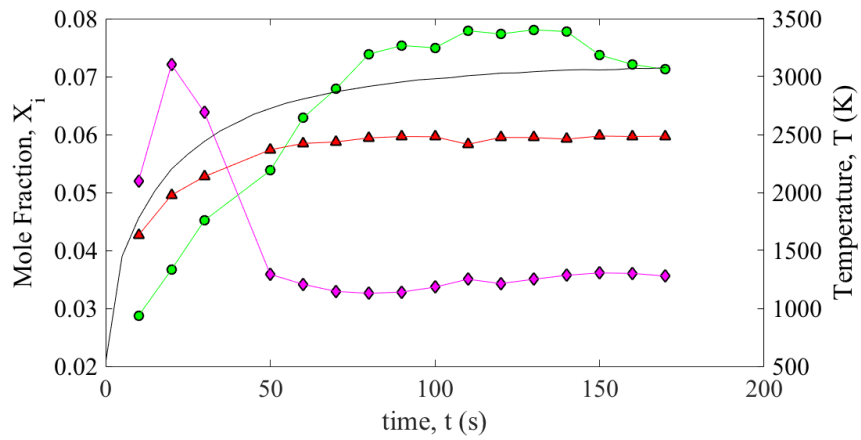
Figure 53. Species and temperature maps for sample irradiated at $I = 900$ W/cm² for $t = 100$ s producing peak surface temperatures of $T_s = 2290$ K.



(a) $I = 650 \text{ W/cm}^2$



(b) $I = 900 \text{ W/cm}^2$



(c) $I = 2400 \text{ W/cm}^2$

Figure 54. Species and temperature over time (●) X_{CO} , (◆) X_{CO_2} , (▲) T_{plume} , (—) T_s

Evolving species concentrations and temperature are shown in Figure 54 for all irradiance cases. In the initial heating stage, plume temperature is highly correlated to surface temperature, followed by a leveling off at 1500, 2000 and 2500 K for the low, medium, high irradiance cases respectively. Surface reactivity rises with T_s , resulting in an increase in CO over time for all cases. The most notable difference between the three cases is the CO_2 time profile. In the low irradiance case, CO_2 initially rises with temperature, but then declines significantly at $T_s > 2150$ K. The drop in CO_2 coincides with a cooling in plume temperature, and slight increase in CO growth rate. This suggests these observations are a result of the endothermic S2 reaction which converts CO_2 to CO . A similar trend is observed in the high irradiance case, with CO_2 dropping after $T_s > X$ K. However, these trends are not observed in the medium irradiance case. One possible explanation of this is inhibition of the S2 reaction by CO [85], which may influencing the reactivity of S2.

$[CO]/[CO_2]$ Temperature Dependence.

Plots of $[CO]/[CO_2]$ versus inverse surface temperature are given in Figure 55. At lower temperatures, all test cases follow the general trend of:

$$\frac{[CO]}{[CO_2]} = 1.7 \pm 0.3 \cdot \exp\left(\frac{-2400 \pm 400}{T}\right) \quad (144)$$

β values are consistent with those reported from the flat plate shear flow cases ($\beta = 2700$ K) and in reasonable agreement with values reported by Tognotti, Otterbien, Phillips, Du, and Walker ($\beta = 3000 - 3200$ K) [21, 39–41, 89].

At higher temperatures where the decline in CO_2 is observed, the slope changes dramatically. The high and low irradiance cases can then be characterized β values of 16,000 and 31,000 K respectively. While these results are significantly higher than flat plate case, they are comparable to those reported by Acosta ($\beta = 18,000$ K) [7]. The

temperature threshold for change in β varies for each case,, suggesting it may be related to inhibition of the S2 reaction by CO or a trace species.

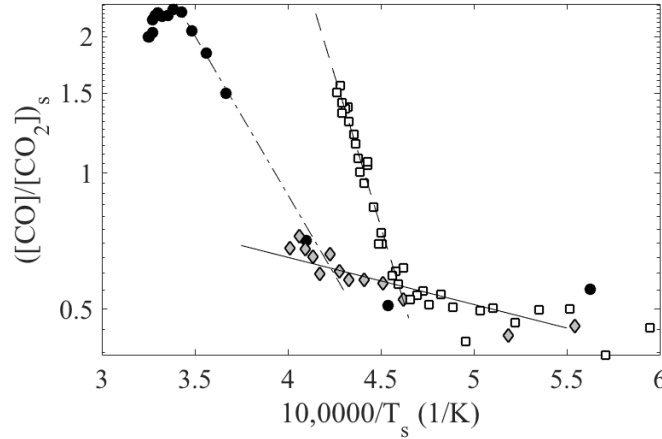


Figure 55. $[CO]/[CO_2]$ versus inverse surface temperature. **Data:** (\square) $I = 650 \text{ W/cm}^2$ (\diamond) $I = 900 \text{ W/cm}^2$ (\bullet) $I = 2400 \text{ W/cm}^2$. **Fits to Eq. (??):** (–) $\alpha = 1.7 \pm 0.3, \beta = 2,400 \pm 400 \text{ K}$; (– . –) $\alpha = 580 \pm 10, \beta = 16,000 \pm 3,000 \text{ K}$; (– –) $\alpha = 8.7 \cdot 10^5 \pm 0.3 \cdot 10^5, \beta = 31,000 \pm 4,000 \text{ K}$.

7.5 Conclusions

We report the first spatially resolved measurements of graphite oxidation in a stagnation flow. Laser irradiated samples were evaluated in a stagnation flow ($a = 30 \text{ s}^{-1}$) for surface temperatures of 1000 - 3100 K using IFTS. Temporal and spatial (0.5 mm/pixel) maps of plume temperature and CO and CO_2 have been provided. Observations of species temporal evolution agree well with work by Acosta [1]. An increase in CO and CO_2 is first observed as the samples are heated, followed by a decline in CO_2 and slight rise in CO , attributed to the $S2:C_s - CO_2$ reaction. Surface temperature threshold for this event varies by test case, suggesting non-Arrhenius behavior possibly related to CO inhibition of the S2 reaction as previously reported [85]. However, given the limited number of test runs, additional data is needed to for validation. The temporal evolu-

tion of $[CO]/[CO_2]$ concentration ratios is evaluated at laser center. Results show two general trends. At lower temperatures, trends of $[CO]/[CO_2] = 1.7 \exp(-2400/T)$ are observed. This is general agreement with steady state observations for flat plate shear flow ($\beta = 3100$ K). When the CO_2 population declines at higher temperatures (2200-2500 K), β values increase significantly, with trends of $\beta = 16,000$ and $31,000$ K. Higher β values are consistent with transient observations reported by Acosta ($\beta = 18,000$ K)[1], but it is unclear what produces these differences in β values.

This work provides the first demonstration of flow velocimetry using IFTS. Correlation of low frequency oscillations in raw IFTS data allow for identification of flow patterns. Magnitudes of the flow velocities can then be roughly estimated using camera frame rates, pixel resolution, and the delay inferred from cross-correlation. Flow maps show deviation from ideal stagnation flow due to buoyancy effects. However results suggest a counterflow like pattern between surface oxidation products being ejected from the surface and the incoming stagnation flow, with a stagnation zone visible 1 mm away from the surface.

VIII. Conclusions

Graphite oxidation has been investigated using IFTS hyperspectral imaging to provide 2D spatial maps of temperature and species concentration. Graphite samples were heated using a $1.07\ \mu\text{m}$ CW fiber laser. The resulting oxidation plume is characterized using MW IFTS. A two layer RTM was used to infer spatial maps of temperature and species (CO , CO_2) concentration from spectral data. The spatially resolved plumes provide unique insight into species formation and transport. Two simplified kinetic transport models are presented to interpret experimental observations. Graphite oxidation is evaluated at 3 flow conditions: buoyant flow, flat plate shear flow, and stagnation flow to observe transport effects.

Graphite oxidation in buoyant flow was observed at irradiances of 1000 and 3600 W/cm^2 producing surface temperatures of 1000 - 4000 K and 3-8 mm thick reacting plumes. Plume temperatures are found to be in non-equilibrium with surface temperatures, peaking at 2500 K. CO population was found to be highly correlated with surface temperature as a result of the $C_s + O_2 \Rightarrow 2CO$ and $C_s + CO_2 \Rightarrow 2CO$ surface reactions. A decline in CO_2 population was observed near laser center due to the $C_s + CO_2 \Rightarrow 2CO$ reaction.

Graphite oxidation in a flat plate shear flow was observed at flow speeds of 5, 7, and 10 m/s ($Re < 7 \cdot 10^4$). and irradiated at 750 and 1500 W/cm^2 , resulting in surface temperatures of 1000 - 4000 K and 2- 4 mm thick reacting plumes. Plume temperatures are again found to be in non-equilibrium with surface temperatures, peaking at 2500 K. CO population was again shown to be highly correlated with surface temperature, with some asymmetry due to flow effects. The decline in CO_2 population due to the $C_s + CO_2 \Rightarrow 2CO$ reaction is less pronounced than in the buoyant case, but can still be observed at laser center.

Graphite oxidation in a stagnation flow was observed in a stagnation flow ($\nu = 1.5$

m/s) at irradiances of 650, 900, and 2400, resulting in surface temperatures of 1500 - 3100 K and reacting stagnation layers on the order of 1 - 3 mm thick. Temporal evolution of CO and CO_2 are observed for the three irradiance conditions. A sharp decrease in CO_2 , associated with the S2 reaction is observed. However the decrease in CO_2 is observed at varying surface conditions. One possible explanation is the inhibition on S2 by CO , which varies for each of the three test cases. Further experiments are needed determine trends.

The $[CO]/[CO_2]$ product ratios are fairly consistent within a particular flow condition, with only slight variation in material. $[CO]/[CO_2]$ product ratios for each of the flow conditions can be expressed as:

$$\text{Buoyant Flow: } [CO]/[CO_2] = 22 \exp(-6000/T_s) \quad (145)$$

$$\text{Flat Plate Shear Flow: } [CO]/[CO_2] = 8 \exp(-3100/T_s) \quad (146)$$

$$\text{Stagnation Flow: } [CO]/[CO_2] = 2 \exp(-2400/T_s) \quad (147)$$

Values for β are generally consistent with the range of reported values, $\beta = 3020 - 7200$ K [21, 37–42]. $[CO]/[CO_2]$ measurements were made over similar T_s conditions for each flow case, suggesting that differences in the reported trends are due to transport effects. It should also be noted that the stagnation flow case exhibited two general trends. At low surface temperature, all data sets follow the trend defined in Eq. (147). At higher surface temperature, $[CO]/[CO_2]$ ratios suddenly increases ($\beta = 16,000$ and $31,000$ K), which coincides with the sharp decrease in CO_2 . Surface temperature threshold for this event varies by test case, suggesting non-Arrhenius behavior possibly related to CO inhibition of the S2 reaction[85].

8.1 Recommendations for Future Work

Although the simplified kinetic transport mechanisms were useful in interpreting observed trends, it is difficult to perfectly replicate experimental results, likely due to the over simplified kinetic and transport models. This highlights the need for development of simulations which incorporate more accurate transport models and detailed kinetic rate packages. CO oxidation kinetics has already been well defined using sets of elementary reactions [14], and similar efforts at defining graphite oxidation packages with semiglobal heterogeneous mechanisms have already been documented [75]. Incorporating these kinetic packages into CFD solvers to simulate complex flow conditions, such as flat plate shear flow and stagnation flow, has also been demonstrated [8]. However the lack of spatially resolved experimental data have prevented the validation of these efforts.

Both flat plate shear flow and stagnation flow measurements presented in this document were designed to provide data for validation of these numerical efforts. However several modifications to the numerical simulations are suggested for direct comparison with experimental work. First, surface temperature profiles should be modified from the uniform temperature assumption to a spatially varying profile, ideally based on experimental measurements. Second, the issue of IFTS line of sight averaging should be addressed. As deconvolution of line of sight measurements is difficult due to nonlinearity, an easier approach may be to convert 3D plume simulations into simulated line of sight radiance measurements. The simulated radiance profiles can then be processed similar to experimental data for more direct comparison.

Also needed for numerical validation is a more thorough and robust experimental data set to fully characterize observed trends. For each flow condition, this would involve repeating current measurements at varying irradiance conditions to fully cover the 1500 - 3500 K region. Also valuable would be a set of experiments in CO_2/N_2 environment.

The removal of O_2 from the environment provides two advantages. First, it would allow isolation of the $C_s - CO_2$ mechanism from any $C_s - O_2$ interactions, allowing for better observation of the S2 mechanism, particularly the inhibition due to CO . Second, the removal of O_2 would prevent the oxidation of CO after if it produced at the surface, removing the complication of coupling of the heterogeneous and homogeneous kinetics.

While IFTS has proven valuable for characterization of graphite oxidation, line of sight averaging continues to be an issue when interpreting species and temperature maps. This can be alleviated with the implementation of the multi-layer RTM method [62]. Current measurements assume a uniform flame along the line of sight, which may introduce systematic errors of up to 6% for plume temperature and 21% for species mole fraction (see Appendix B). Recently a technique has been developed which leverages the multiple line of sight measurements provided by IFTS to infer radial flame profiles [62]. However implementation of this technique would require redesign of experiments to produce a radially symmetric flame. This could be achieved through stagnation flow measurements or by reorienting the buoyant flow measurements such that the sample is prone with a upward buoyant symmetric flame.

Future laser lethality work will focus on more realistic materials, such as carbon fiber. Much of the kinetics of carbon fiber oxidation is initially dominated by volatile decomposition and combustion. However, once these volatiles are removed, the material consists primarily of bare carbon fibers. Therefore simulations for bare carbon fiber oxidation can build upon the heterogeneous rate packages developed for graphite oxidation. A similar set of experimental data focusing on laser irradiated bare carbon fibers would be required for validation.

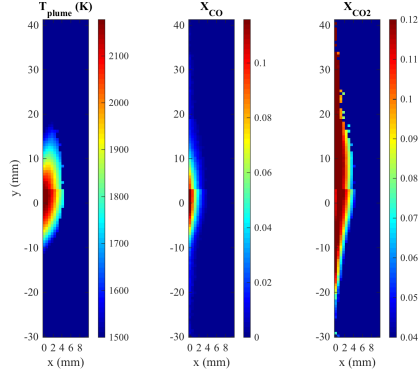
Appendix A. Supplemental Data

The following section provides supplemental data for each of experimental data sets. Spatial maps of plume temperature and species mole fraction are provided by IFTS, using a 2 layer RTM assuming a uniform path and flame length across the field of view (see Chapters II, IV-VI). Surface temperature data is provided using a MW camera and processed using graphite emissivities (see Chapters IV). Data files can be provided upon request.

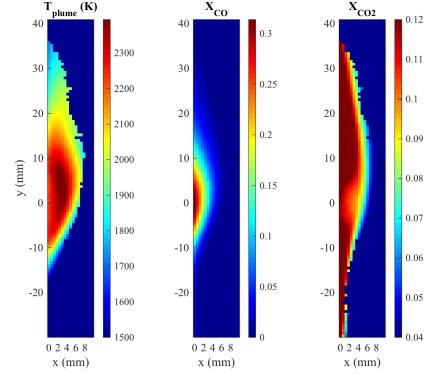
1.1 Graphite Oxidation in Buoyant Flow

Table 16. Test matrix: graphite oxidation in buoyant flow

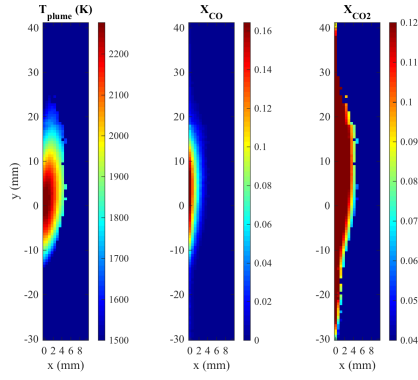
Material	Irradiance (W/cm ²)
Fine	1000
Fine	3600
Isomolded	1000
Isomolded	3600
Pyrolytic	1000
Pyrolytic	3600



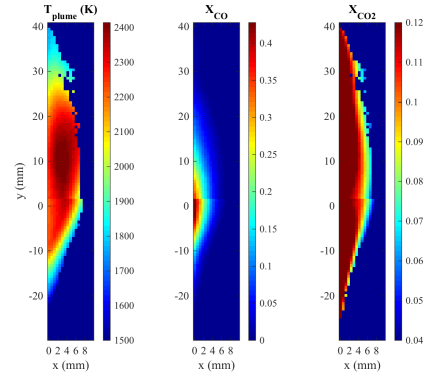
(a) Isomolded, $I = 1000 \text{ W/cm}^2$



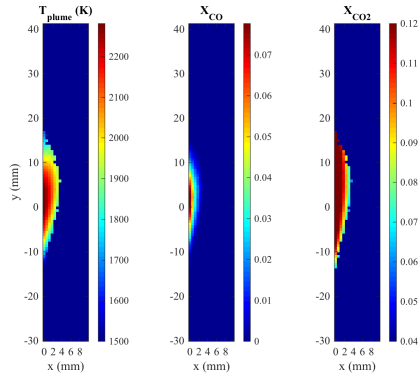
(b) Isomolded, $I = 3600 \text{ W/cm}^2$



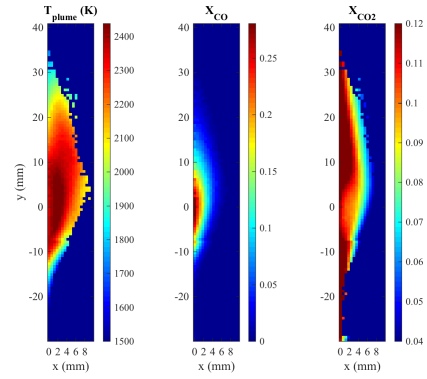
(c) Fine, $I = 1000 \text{ W/cm}^2$



(d) Fine, $I = 3600 \text{ W/cm}^2$



(e) Pyrolytic, $I = 1000 \text{ W/cm}^2$



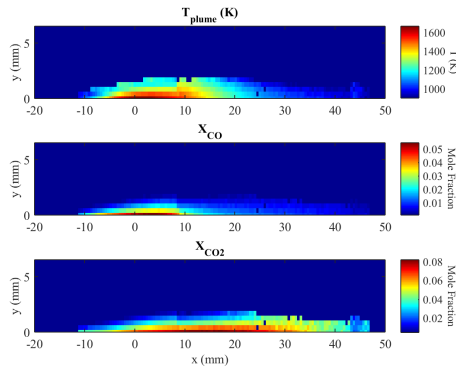
(f) Pyrolytic, $I = 3600 \text{ W/cm}^2$

Figure 56. Graphite oxidation in buoyant flow

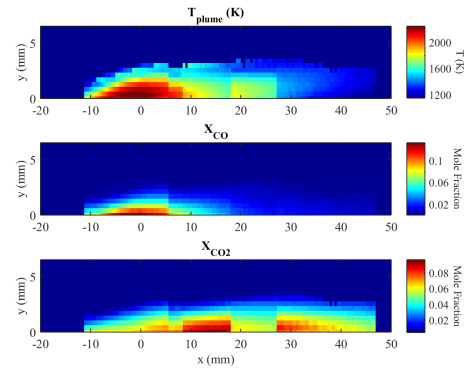
1.2 Graphite Oxidation in Flat Plate Shear Flow

Table 17. Test matrix: graphite oxidation in flat plate shear flow

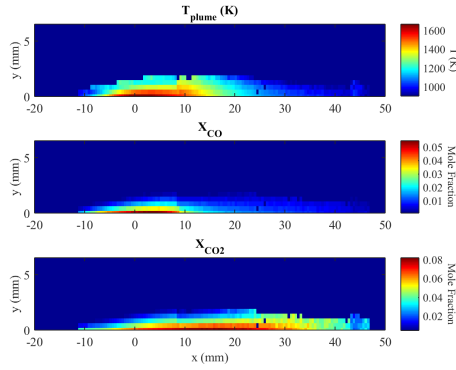
Material	Flow (m/s)	Irradiance (W/cm ²)	Notes
Fine	5	750	
Fine	7	750	
Fine	10	750	no data
Fine	5	1500	
Fine	7	1500	
Fine	10	1500	
Isomolded	5	750	
Isomolded	7	750	no data
Isomolded	10	750	
Isomolded	5	1500	
Isomolded	7	1500	
Isomolded	10	1500	
Pyrolytic	5	750	
Pyrolytic	7	750	
Pyrolytic	10	750	
Pyrolytic	5	1500	
Pyrolytic	7	1500	
Pyrolytic	10	1500	



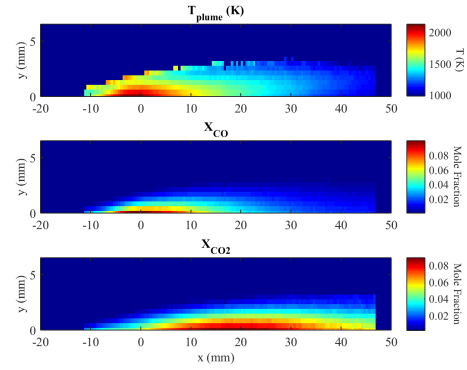
(a) $I = 750 \text{ W/cm}^2$, $V = 5 \text{ m/s}$



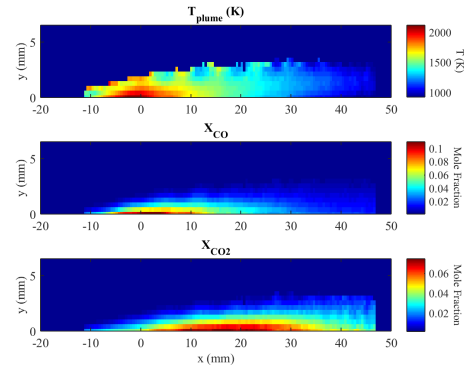
(b) $I = 1500 \text{ W/cm}^2$, $V = 5 \text{ m/s}$



(c) $I = 750 \text{ W/cm}^2$, $V = 7 \text{ m/s}$



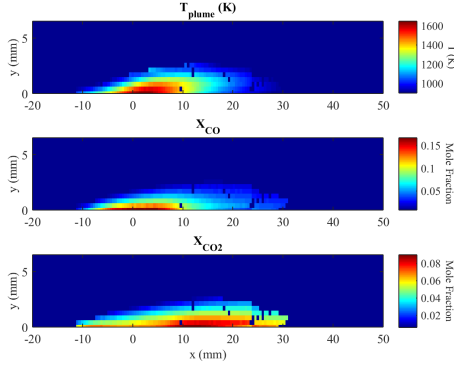
(d) $I = 1500 \text{ W/cm}^2$, $V = 7 \text{ m/s}$



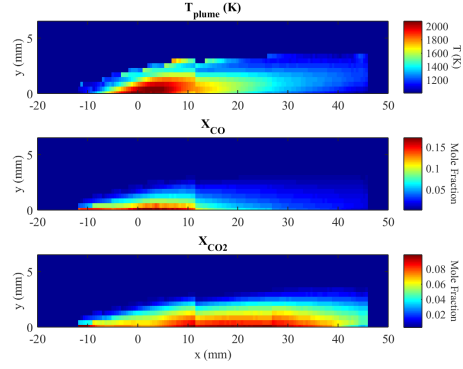
(f) $I = 1500 \text{ W/cm}^2$, $V = 10 \text{ m/s}$

(e) $I = 750 \text{ W/cm}^2$, $V = 10 \text{ m/s}$ - no data available

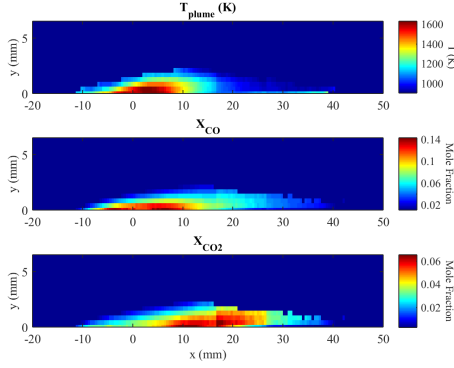
Figure 57. Oxidation of fine porosity graphite in flat plate shear flow



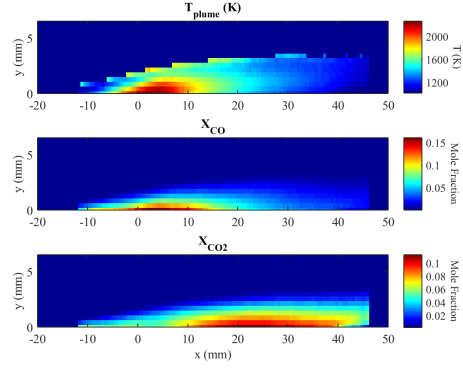
(a) $I = 750 \text{ W/cm}^2$, $V = 5 \text{ m/s}$



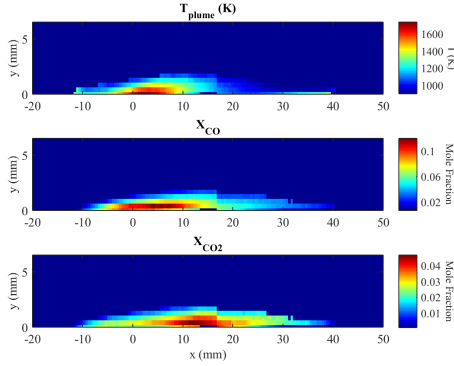
(b) $I = 1500 \text{ W/cm}^2$, $V = 5 \text{ m/s}$



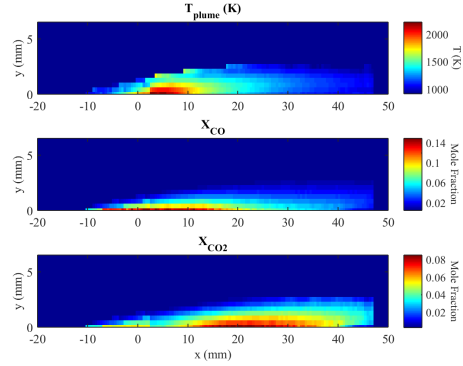
(c) $I = 750 \text{ W/cm}^2$, $V = 7 \text{ m/s}$



(d) $I = 1500 \text{ W/cm}^2$, $V = 7 \text{ m/s}$

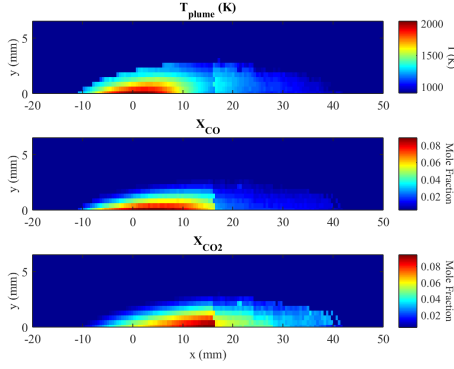


(e) $I = 750 \text{ W/cm}^2$, $V = 10 \text{ m/s}$

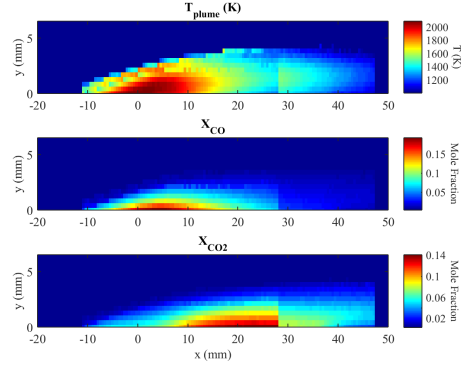


(f) $I = 1500 \text{ W/cm}^2$, $V = 10 \text{ m/s}$

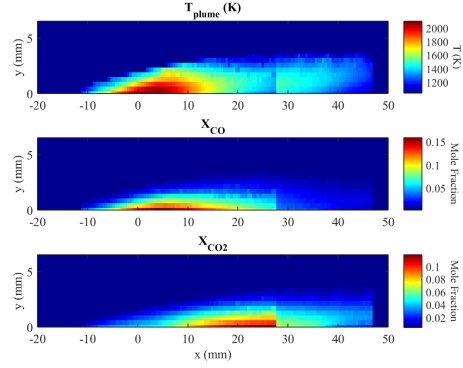
Figure 58. Oxidation of isomolded graphite in flat plate shear flow



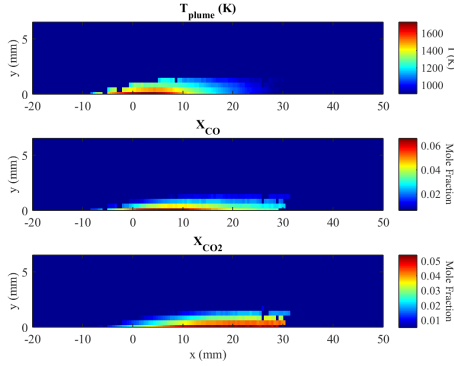
(a) $I = 750 \text{ W/cm}^2$, $V = 5 \text{ m/s}$



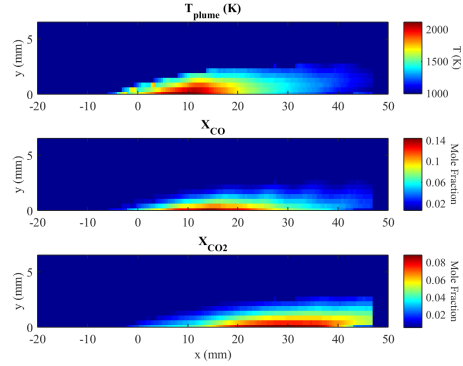
(b) $I = 1500 \text{ W/cm}^2$, $V = 5 \text{ m/s}$



(d) $I = 1500 \text{ W/cm}^2$, $V = 7 \text{ m/s}$



(e) $I = 750 \text{ W/cm}^2$, $V = 10 \text{ m/s}$



(f) $I = 1500 \text{ W/cm}^2$, $V = 10 \text{ m/s}$

Figure 59. Oxidation of pyrolytic graphite in flat plate shear flow

Appendix B. Two-Layer Radiative Transfer Model Error Analysis

This appendix presents an evaluation of the two-layer radiative transfer model (RTM) which is used throughout this document. The two-layer RTM assumes a flame layer which is uniform along the line of sight. Errors associated with this assumption are evaluated over a range of typical test conditions ($T_{plume} = 1000 - 2500$ K, $X_{CO} < 0.3$, $X_{CO_2} < 0.2$). Line of sight spectra are simulated for each simulated plume profile. A non-linear fit to the two-layer radiative transfer model (RTM) is then used to infer plume temperature and species profile. Errors associated with two-layer RTM and choice of flame thickness definition are discussed. Best results are achieved assuming a constant flame thickness, defined as the species profile width at 30% peak value, with typical errors of 1-6% for $T_{plume} = 1000-2500$ K, 5-21% for $X_{CO} = 0.001 - 0.3$, 5-21% for $X_{CO_2} = 0.001 - 0.2$.

2.1 Background

Imaging Fourier transform spectroscopy (IFTS) has been demonstrated as a useful combustion diagnostic due to the ability to infer 2D maps of species and temperature. Using a radiative transfer model (RTM) and available cross-section databases, the spectral content of each pixel is used to determine plume temperature and species concentration[61]. This is commonly done using a two-layer RTM, which assumes uniform flame and path layers. Realistic flames are certainly not uniform along the line of sight. However, the nonlinearity of radiative transfer make it difficult to infer flame profiles from the measured radiance without flame symmetry [62]. Therefore for current studies, the two-layer method was used.

There are several issues with the two-layer method which may introduce systematic error. The uniform flame layer assumption obviously neglects the strong gradients along the line of sight. Also, the choice of flame length, ℓ_f , can be problematic. While it

is easy to define the total length from detector to flame center, it is difficult to determine the appropriate transition point between flame and path. In many cases, this is avoided by reporting species population in terms of column density, $c'_i = \ell_f n X_i$, or fractional column density, $q_i = \ell_f X_i$, where n is concentration, X_i is species mole fraction. However for this work, it was desirable to report results in terms of species mole fraction.

This work assesses the errors associated with the two-layer RTM. Line of sight spectra are simulated for typical flame conditions. Species and temperature profiles are inferred using the two-layer RTM. Two possible definitions for ℓ_f are considered: 1) flame geometry based, line of sight varying and 2) constant flame length. Errors associated with the two-layer RTM and choice of flame length are discussed.

2.2 Method

Line of sight spectra are simulated for a set of plume profiles with parameters similar to those observed experimentally. A sample profile is given in Figure 60 with peak values of $T_{plume} = 1500$ K, $X_{CO_2} = 0.2$, and $X_{CO} = 0.3$. Test profiles are generated assuming a Gaussian temperature and species distribution, with standard deviation of $\sigma_{g-T} = 1$ cm and $\sigma_{g-c} = 0.7$ cm respectively. Free stream values of $T^o = 300$ K, $X_{CO}^o = 0$, and $X_{CO_2}^o = 0.0001$ were assumed. Values used for free stream CO_2 are based on typical measurements, which were higher than atmospheric values (400 ppm) due to the detector proximity to the flame (36 cm). Similar profiles with peak values of $X_{CO} = 0.1, 0.3$, $X_{CO_2} = 0.1, 0.2$, and $T_{plume} = 1500, 2500$ K were evaluated.

The measured radiance for each line of sight is a function of the species and temperature profiles along the line of sight. Written in discretized form, the measured radiance is a sum of contributions from each layer in the line of sight, weighted by the

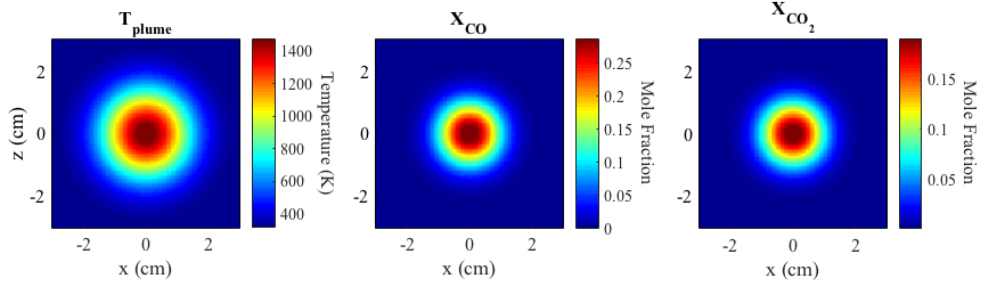


Figure 60. Simulated Gaussian flame profile. Temperature: $\sigma_{g-T} = 1$ cm with peak value of $T_{plume} = 1500$ K. **Species:** $\sigma_{g-c} = 0.7$ cm with peak values of $X_{CO_2} = 0.2$ and $X_{CO} = 0.3$.

transmissivity of subsequent layers:

$$L = \sum_{i=1}^K \left(\varepsilon_i(\alpha_i) B(T_i) \prod_{j=i+1}^K \tau_j(\alpha_j) \right) \quad (148)$$

where ε_i is the emissivity of layer i , $B(T_i)$ is the radiance of blackbody at temperature T_i , and τ_j is the transmissivity of layer j . Assuming equilibrium, emissivity can be written in terms of transmissivity, $\varepsilon = 1 - \tau$, where transmissivity is defined by Beer's Law in terms of optical depth, α :

$$\tau_i = \exp(-\alpha_i) \quad (149)$$

$$\alpha_i = n \ell_i \sum_m X_m \sigma_m(\nu, T) \quad (150)$$

where n is number density, ℓ_i is length of layer i , X_m is the mole fraction of species m , and σ_m is the cross-section of species m provided by HITRAN and CDSD databases.

Line of sight spectra are simulated using Eq. (148) at intervals of 0.05 cm based on instrument resolution. A total distance of 36 cm from detector to flame center is used based on current measurement conditions. A sample set of line of sight spectra is shown in Figure 61 for peak values of $T_{plume} = 1500$ K, $CO = 0.1$, and $CO_2 = 0.2$. Differ-

ences in path transmissivity along different lines of sight is most visible in comparing measurements at flame center (red) to outer layers, particularly in the 2300 - 2400 cm^{-1} CO_2 feature.

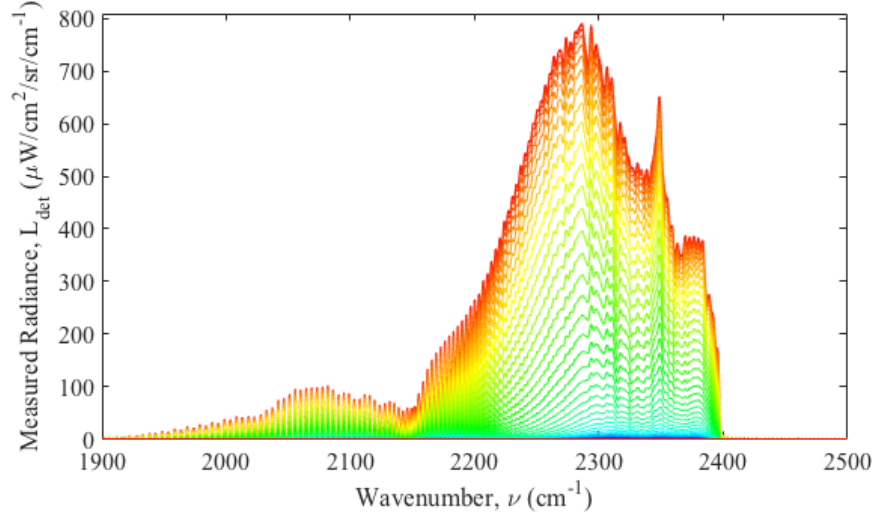


Figure 61. Line of sight spectra generated using Eq. (148) for peak T_{plume} , CO , and CO_2 of 1500 K, 0.1 and 0.2 respectively. Color corresponds to line of sight location with red corresponding to flame center with LOS spacing of $\Delta x = 0.05 \text{ cm}$.

A two-layer radiative transfer model, similar to that used for experimental work, is then fit to the simulated line of sight spectra to evaluate the use of the two-layer model. The measured radiance can be expressed as:

$$L_{det} = \tau_{atmos}(\alpha_{atmos}) \cdot \epsilon_{plume}(\alpha_{plume}) \cdot B(T_{plume}) \quad (151)$$

where α_{plume} and α_{atmos} are defined by Eq. (150) and plume and atmospheric parameters. A non-linear least squares fitting routine is then used to solve for T_{plume} , T_{atmos} , $q_{i-atmos}$, and $q_{i-plume}$, where q_i is the fractional column density, $q_i = \ell_f X_i$.

Determination of species mole fraction then relies on choice of flame length, ℓ_f .

Two flame length definitions are evaluated. First, a simple constant flame length is considered. This has the advantage of not assuming a particular flame geometry. Choice of flame length is determined by minimizing error along all line of sight measurements. Second, a line of sight varying flame length assuming a circular flame geometry is evaluated. Flame radius is determined by minimizing error along all line of sight measurements. The errors associated with the two-layer model and each flame length definition are then computed. Truth values are based on averaging along the line of sight, with each layer weighted by its relative radiance.

2.3 Results

A sample fit of simulated line of sight spectra is shown in Figure 62. The simulated spectra is taken from a flame profile with Gaussian peak values of $T_{plume} = 1500$ K, $X_{CO} = 0.3$, $X_{CO_2} = 0.1$, with line of sight through flame center. Good agreement is found using the two-layer RTM, with residuals of less than $10 \mu\text{W}/\text{cm}^2/\text{sr}/\text{cm}^{-1}$ for most of the spectral region. Larger residuals of $20 \mu\text{W}/\text{cm}^2/\text{sr}/\text{cm}^{-1}$ were observed in the 2350 - 2400 cm^{-1} absorption region. Fit results estimate plume parameters of: $q_{CO} = 0.492 \pm 0.002$ cm, $q_{CO_2} = 0.139 \pm 0.0004$ cm, and $T_{plume} = 1388 \pm 1$ K, where uncertainties are based on 95% fit confidence values. Fits using the two-layer model are repeated for each line of sight from flame center until insufficient signal, $L_{det} < 30 \mu\text{W}/\text{cm}^2/\text{sr}/\text{cm}^{-1}$.

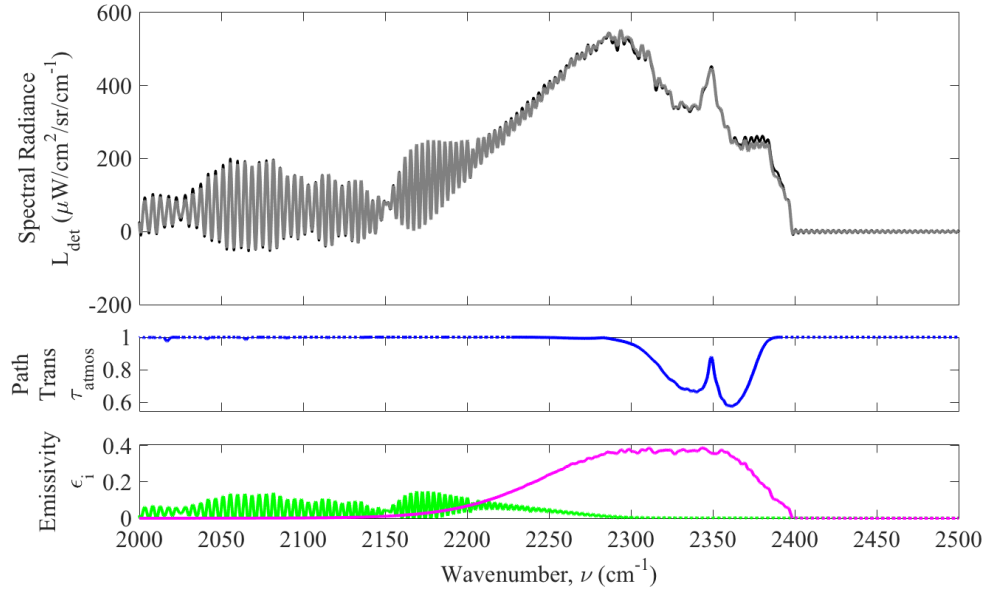


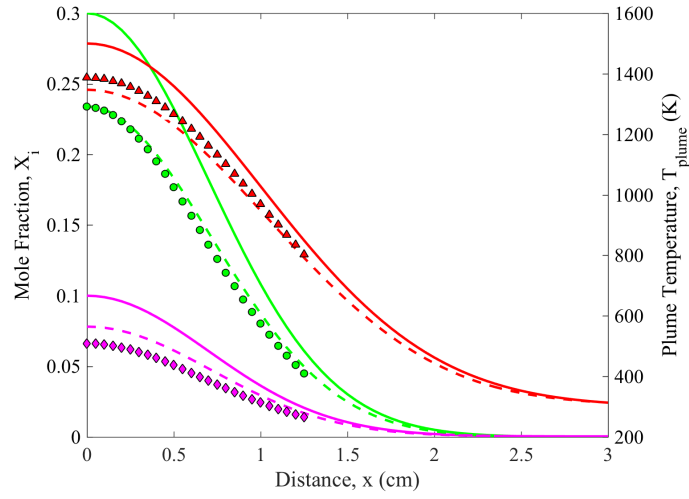
Figure 62. Sample two-layer model fit to simulated line of sight spectra. (---) simulated measured radiance, (—) two-layer RTM radiance, (—) τ_{atmos} ; (—) ϵ_{CO} ; (—) ϵ_{CO2} . Model fits correspond to $q_{CO} = 0.492 \pm 0.002$ cm, $q_{CO_2} = 0.139 \pm 0.0004$ cm, and $T_{plume} = 1388 \pm 1$ K,

Mole fractions are then computed assuming a constant flame length. Best results were achieved using flame length of $\ell_f = 2.1$ cm, which corresponds to the where species concentration decreases to 30% of the peak value. Results are compared with light of sight averaged values and radial profiles in Figure 63(a). Errors are estimated relative to line of sight averaged values. Plume temperatures are slightly over predicted, with errors of 1-3 %. Predicted species profiles maintain relative shape, but with higher errors of 2-10 % and 15-18% for X_{CO} and X_{CO_2} respectively.

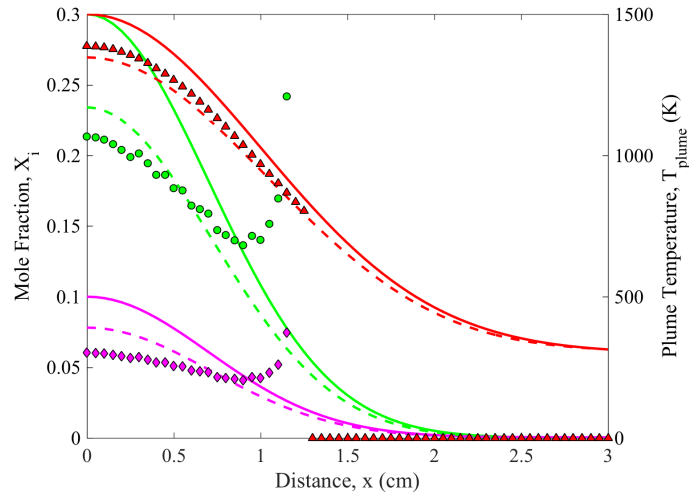
Similar analysis was repeated for varying flame length method. The flame is assumed to be circular, with fixed diameter d . Flame length is then determined based on chord length at each line of sight, $\ell_f(x) = 2\sqrt{(d/2)^2 + x^2}$. Results are compared with line of sight averaged values and radial profiles in Figure 63(b). Species profile curvature is found to be strongly dependent on choice of flame diameter. This is due to the coupling of the flame length and mole fraction, and the flame length dependence on choice of d .

Predicted species profiles show smaller errors than the constant flame length method, with inner flame errors of $<10\%$ for X_{CO} and X_{CO_2} at $x < 1$ cm. However, species profile curvature is poorly reconstructed. Results are even flatter for poor choice of flame diameter.

Comparing the two methods, constant flame length is preferred due to better reconstruction of the species profile. In the case of constant flame length, poor choice of ℓ_f will only scale mole fraction profiles, but leave the relative shape intact. In the case of variable flame length, poor choice of flame diameter can lead to large errors in profile shape and relative value. The remaining test profiles were analyzed assuming a constant flame length of 2.1 cm. Similar errors in plume temperature were reported across all cases, with errors of $<6\%$. Errors in species mole fraction of 5-21% were observed for $X_{CO} = 0.001 - 0.3$ and $X_{CO_2} = 0.001 - 0.2$.



(a) Constant flame length: $\ell_f = 2.1$ cm



(b) Variable flame length assuming circular flame ($d = 1.74$ cm):

$$\ell_f(x) = 2\sqrt{(d/2)^2 + x^2}$$

Figure 63. Comparison of two-layer RTM results with truth values using (a) constant and (b) variable flame length methods. Truth values: (---) radial profile, (- -) line of sight averaged, (---) T_{plume} , (---) X_{CO} , (---) X_{CO_2} . Two-layer RTM fit values: (▲) T_{plume} , (●) X_{CO} , (◆) X_{CO_2} .

2.4 Summary

The two-layer RTM has been evaluated using simulated line of sight spectra for a range of test profiles. Profiles were chosen to cover the range of typical test conditions, with peak profile values of $X_{CO} = 0.1, 0.3$, $X_{CO_2} = 0.1, 0.2$, and $T_{plume} = 1500, 2500$ K. Two methods at defining flame length are evaluated: constant flame length, and variable flame length based on flame geometry. Constant flame length is found to be preferable, due to better reconstruction of the species profile curvature and less sensitivity to poor choice in flame length. Results suggest errors for the two-layer method with constant flame length may be as high as 21% for X_{CO} and X_{CO_2} and 6% for T_{plume} . These errors are significantly higher than those errors based on fit confidence levels, and highlight the need for analysis of systematic errors when implementing the two-layer model.

Bibliography

1. Roberto I. Acosta, Kevin C. Gross, and Glen P. Perram. Combustion kinetics of laser irradiated porous graphite from imaging Fourier transform spectroscopy. *Combustion and Flame*, 163:90–99, jan 2016.
2. G.W Autio and E Scala. The normal spectral emissivity of isotropic and anisotropic materials. *Carbon*, 4(1):13–28, may 1966.
3. GraphiteStore. <https://www.graphitestore.com/>, 2015.
4. Glen P Perram, Michael A Marciniak, and Matthew Goda. Laser Technologies for Defense and Security; High-energy laser weapons: technology overview. volume 5414, page 1 <last_page> 25, 2004.
5. Annemie Bogaerts, Zhaoyang Chen, Renaat Gijbels, and Akos Vertes. Laser ablation for analytical sampling: What can we learn from modeling? *Spectrochimica Acta - Part B Atomic Spectroscopy*, 58(11):1867–1893, 2003.
6. H. K. Chelliah. The influence of heterogeneous kinetics and thermal radiation on the oxidation of graphite particles. *Combustion and Flame*, 104(1-2):81–94, 1996.
7. Roberto I Acosta. *Imaging Fourier Transform Spectroscopy of the Boundary Layer Plume from Laser Irradiated Polymers and Carbon Materials*. PhD thesis, AFIT, 2014.
8. Ryan Frederick Johnson. *Multidimensional Reacting Flow Simulations with Coupled Homogeneous and Heterogeneous Models*. PhD thesis, University of Virginia, 2014.
9. Christopher R. Shaddix, Franz Holzleithner, Manfred Geier, and Brian S. Haynes. Numerical assessment of Tognotti determination of CO₂/CO production ratio during char oxidation. *Combustion and Flame*, 160(9):1827–1834, sep 2013.
10. Normand M Laurendeau. Heterogeneous kinetics of coal char gasification and combustion. *Progress in Energy and Combustion Science*, 4(4):221 – 270, 1978.
11. a. Makino, N. Araki, and Y. Mihara. Combustion of artificial graphite in stagnation flow: Estimation of global kinetic parameters from experimental results. *Combustion and Flame*, 96(3):261–274, 1994.
12. Sang-min Lee, Dong-su Kang, and Jea-seung Roh. Bulk graphite : materials and manufacturing process. *Carbon Letters*, 16(3):135–146, 2015.
13. R.A. Yetter and F.L. Dryer. Inhibition of moist carbon monoxide oxidation by trace amounts of hydrocarbons. *Symposium (International) on Combustion*, 24(1):757–767, 1992.
14. R.A. Yetter, F.L. Dryer, and H. Rabitz. Complications of one-step kinetics for moist CO oxidation. *Symposium (International) on Combustion*, 21(1):749–760, 1988.

15. G.K. Sobolev. High-temperature oxidation and burning of carbon monoxide. *Symposium (International) on Combustion*, 7(1):386–391, jan 1958.
16. Raymond Friedman and Joseph A Cyphers. Flame structure studies. iii. gas sampling in a low-pressure propane-air flame. *The Journal of Chemical Physics*, 23(10):1875–1880, 1955.
17. HC Hottel, GC Williams, NM Nerheim, and GR Schneider. Kinetic studies in stirred reactors: combustion of carbon monoxide and propane. In *Symposium (International) on Combustion*, volume 10, pages 111–121. Elsevier, 1965.
18. FL Dryer and I Glassman. High-temperature oxidation of co and ch₄. In *Symposium (International) on combustion*, volume 14, pages 987–1003. Elsevier, 1973.
19. Richard K Lyon, James E Hardy, and William Von Holt. Oxidation kinetics of wet co in trace concentrations. *Combustion and flame*, 61(1):79–86, 1985.
20. J.B. B Howard, G.C. C Williams, and D.H. H Fine. Kinetics of carbon monoxide oxidation in postflame gases. *Symposium (International) on Combustion*, 14(1):975–986, 1973.
21. Zhiyou Du, Adel F Sarofim, John P. Longwell, and Charles A Mims. Kinetic measurement and modeling of carbon oxidation. *Energy & Fuels*, 5(1):214–221, 1991.
22. Atsushi Makino and C K Law. Ignition and Extinction of CO Flame over a Carbon Rod. *Combustion Science and Technology*, 73(4-6):589– 615, 1990.
23. Guillermo Calleja, Adel F Sarofim, and Christos Georgakis. Effect of char gasification reaction order on bounding solutions for char combustion. *Chemical Engineering Science*, 36(5):919–929, 1981.
24. Morris Mentser and Sabri Ergun. Kinetics of oxygen exchange between co₂ and co on carbon. *Carbon*, 5(4):331–337, 1967.
25. Sabri Ergun. Kinetics of the reaction of carbon with carbon dioxide. *The Journal of Physical Chemistry*, 60(4):480–485, 1956.
26. Jo Gadsby, FJ Long, P Sleightholm, and KW Sykes. The mechanism of the carbon dioxide–carbon reaction. In *Proceedings of the Royal Society of London A: Mathematical, Physical and Engineering Sciences*, volume 193, pages 357–376. The Royal Society, 1948.
27. S. Dutta, C. Y. Wen, and R. J. Belt. Reactivity of Coal and Char. 1. In Carbon Dioxide Atmosphere. *Industrial & Engineering Chemistry Process Design and Development*, 16(1):20–30, jan 1977.
28. E.T. Turkdogan and J.V. Vinters. Kinetics of oxidation of graphite and charcoal in carbon dioxide. *Carbon*, 7(1):101–117, feb 1969.

29. E.T. Turkdogan, R.G. Olsson, and J.V. Vinters. Pore characteristics of carbons. *Carbon*, 8(4):545–564, oct 1970.
30. E.T. Turkdogan and J.V. Vinters. Effect of carbon monoxide on the rate of oxidation of charcoal, graphite and coke in carbon dioxide. *Carbon*, 8(1):39–53, feb 1970.
31. A.N. Hayhurst and M.S. Parmar. Does solid carbon burn in oxygen to give the gaseous intermediate CO or produce CO₂ directly? Some experiments in a hot bed of sand fluidized by air. *Chemical Engineering Science*, 53(3):427–438, feb 1998.
32. L Laine, F J Vastola, P L Walker, N R Laine, F J Vastola, and P L Walker. The Importance of Active Surface Area in the Carbon-Oxygen Reaction. *The Journal of physical chemistry*, 67(10):2030, 1963.
33. I.M. Bews, A.N. Hayhurst, S.M. Richardson, and S.G. Taylor. The order, Arrhenius parameters, and mechanism of the reaction between gaseous oxygen and solid carbon. *Combustion and Flame*, 124(1-2):231–245, jan 2001.
34. I.W. W Smith. Kinetics of combustion of size-graded pulverized fuels in the temperature range 1200–2270 K. *Combustion and Flame*, 17(3):303–314, 1971.
35. A Tomita, OP Mahajan, and PL Walker Jr. Catalysis of char gasification by minerals. *Prepr. Am. Chem. Soc. Div. Fuel ...*, pages 4–6, 1977.
36. Muhammad F Irfan, Muhammad R. Usman, and K. Kusakabe. Coal gasification in CO₂ atmosphere and its kinetics since 1948: A brief review. *Energy*, 36(1):12–40, jan 2011.
37. J. R. Arthur. Reactions between carbon and oxygen. *Transactions of the Faraday Society*, 47:164, 1951.
38. M Rossberg. Experimentelle Ergebnisse uber die Primarreaktionen bei der Kohlenstoffverbrennung. *Zeitschrift fur Elektrochemie, Berichte der Bunsengesellschaft fur physikalische Chemie*, 60(952-956), 1956.
39. L Tognotti, J P Longwell, and A F Sarofim. The products of the high temperature oxidation of a single char particle in an electrodynamic balance. *Symposium (International) on Combustion*, 23(1):1207–1213, 1991.
40. Michel Otterbein and Lucien Bonnetain. Combustion d'un carbone vitreux sous basses pressions d'oxygene. *Carbon*, 6(6):877–885, 1968.
41. Roger Phillips, F J Vastola, and P L Walker. Factors affecting the product ratio of the carbon-oxygen reaction-II. Reaction temperature. *Carbon*, 8(2):205–210, 1970.
42. P L Walker, Frank Rusinko, and L G Austin. Gas Reactions of Carbon. 11:133–221, 1959.

43. Temi M Linjewile, Venkata S Gururajan, and Pradeep K Agarwal. The COCO₂ product ratio from the combustion of single petroleum coke spheres in an incipiently fluidized bed. *Chemical Engineering S*, 50(12):1881–1888, 1995.
44. Micheal Eismann. *Hyperspectral Remote Sensing*. SPIE, 2012.
45. Elizabeth a. Moore, Kevin C. Gross, Spencer J. Bowen, Glen P. Perram, Martin Chamberland, Vincent Farley, Jean-Philippe Gagnon, Philippe Lagueux, and Andre Villemaire. Characterizing and overcoming spectral artifacts in imaging Fourier-transform spectroscopy of turbulent exhaust plumes. *Proceedings of SPIE*, 7304, 2009.
46. L.S. Rothman, I.E. Gordon, R.J. Barber, H. Dothe, R.R. Gamache, A. Goldman, V.I. Perevalov, S.A. Tashkun, and J. Tennyson. HITEMP, the high-temperature molecular spectroscopic database. *Journal of Quantitative Spectroscopy and Radiative Transfer*, 111(15):2139–2150, oct 2010.
47. S.A. Tashkun and V.I. Perevalov. CDSD-4000: High-resolution, high-temperature carbon dioxide spectroscopic databank. *Journal of Quantitative Spectroscopy and Radiative Transfer*, 112(9):1403–1410, jun 2011.
48. Frank P. Incropera, David P. Dewitt, Theodore L. Bergman, and Adrienne S. Levine. *Fundamentals of Heat and Mass Transfer*. John Wiley & Sons, sixth edition, 2007.
49. H Blasius. Grenzsichten in Fliissigkeiten mit kleiner Reibung. *Zeitschrift fur Mathematik und Physik*, 56(1):1–37, 1908.
50. Fritz Homann. Der einfluss grosser zähigkeit bei der strömung um den zylinder und um die kugel. *ZAMM-Journal of Applied Mathematics and Mechanics/Zeitschrift für Angewandte Mathematik und Mechanik*, 16(3):153–164, 1936.
51. Merwin Sibulkin. Heat transfer near the forward stagnation point of a body of revolution, 1952.
52. Frank M. White. *Viscous Fluid Flow*. McGraw-Hill, third edition, 2001.
53. Atsushi Makino. A theoretical and experimental study of carbon combustion in stagnation flow. *Combustion and Flame*, 81(2):166–187, 1990.
54. Simon Ostrach. An Analysis of Laminar Free-Convection Flow and Heat Transfer about a Flat Plate Parallel to the Direction of the Generating Body Force. Technical report, 1953.
55. Michael L. Lander, John O. Bagford, Daniel B. Seibert, and Robert J. Hull. High power calibration of commercial power meters using an NIST-traceable secondary standard. *Journal of Laser Applications*, 8(2):103, 1996.

56. R. J. Hull and M. L. Lander. Laser Hardened Materials Evaluation Laboratory (LH-MEL). *Journal of Laser Applications*, 8(3):161, 1996.
57. Michael L. Lander, John O. Bagford, Mark T. North, and Robert J. Hull. Characterization of the thermal performance of high heat flux systems at the Laser Hardened Materials Evaluation Laboratory. In Ali M. Khounsary, editor, *Proc. SPIE, High Heat Flux Engineering III*, pages 129–137, Denver, CO, nov 1996. International Society for Optics and Photonics.
58. Grady T Phillips, William A Bauer, Charles D Fox, and Ashley E Gonzales. Mass removal by oxidation and sublimation of porous graphite during fiber laser irradiation. *Optical Engineering*, 56(1), 2016.
59. Nicholas C Herr. *Degradation of Carbon Fiber Reinforced Polymer and Graphite by Laser Heating*. PhD thesis, Air Force Institute of Technology, 2016.
60. Sean M. Baumann, Cameron Keenan, Michael A. Marciniak, and Glen P. Perram. Spectral and temperature-dependent infrared emissivity measurements of painted metals for improved temperature estimation during laser damage testing. In Gregory J. Exarhos, Vitaly E. Gruzdev, Joseph A. Menapace, Detlev Ristau, and MJ Soileau, editors, *SPIE Laser Damage*, page 923713. International Society for Optics and Photonics, oct 2014.
61. Kevin C. Gross, Kenneth C. Bradley, and Glen P. Perram. Remote Identification and Quantification of Industrial Smokestack Effluents via Imaging Fourier-Transform Spectroscopy. *Environmental Science and Technology*, 44:9390–9397, 2010.
62. Michael R Rhoby. *Laminar flame combustion diagnostics using imaging Fourier transform spectroscopy*. PhD thesis, Air Force Institute of Technology, 2016.
63. S. Depraz, M.Y. Perrin, Ph. Rivière, and A. Soufiani. Infrared emission spectroscopy of CO₂ at high temperature. Part II: Experimental results and comparisons with spectroscopic databases. *Journal of Quantitative Spectroscopy and Radiative Transfer*, 113(1):14–25, jan 2012.
64. Jacob L Harley. *Development of Imaging Fourier-Transform Spectroscopy for the Characterization of Turbulent Jet Flames*. PhD thesis, Air Force Institute of Technology, 2014.
65. J.R Egerton and R.F Strickland-Constable. Catalysis of the oxidation of graphite in the temperature range 1000-2000C. *Carbon*, 7(6):719, dec 1969.
66. Eung Soo Kim and Hee Cheon No. Experimental study on the oxidation of nuclear graphite and development of an oxidation model. *Journal of Nuclear Materials*, 349:182–194, 2006.

67. Daehee Kim, Sangmin Choi, Christopher R. Shaddix, and Manfred Geier. Effect of CO₂ gasification reaction on char particle combustion in oxy-fuel conditions. *Fuel*, 120:130–140, mar 2014.
68. Atsushi Makino. An attempt for applying formulation of the carbon combustion in the stagnation flowfield to some experimental comparisons related to the boundary layer combustion. *Combustion and Flame*, 161(6):1537–1546, 2014.
69. I. W. Smith. The combustion rates of coal chars: A review. *Symposium (International) on Combustion*, pages 1045–1065, 1982.
70. J.R. Walls and R.F. Strickland-Constable. Oxidation of carbon between 1000–2400C. *Carbon*, 1(3):333–338, apr 1964.
71. Luo Xiaowei, Robin Jean-Charles, and Yu Suyuan. Effect of temperature on graphite oxidation behavior. *Nuclear Engineering and Design*, 227:273–280, 2004.
72. Juan Yu, Wei Ou, and Kuan Zhou. Mass transfer coefficients considering boundary layer reaction in oxy-fuel combustion of coal char. *Fuel*, 124:173–182, 2014.
73. André Zoulalian, Roda Bounaceur, and Anthony Dufour. Kinetic modelling of char gasification by accounting for the evolution of the reactive surface area. *Chemical Engineering Science*, 138:281–290, dec 2015.
74. Chao'en Li and Trevor C. Brown. Carbon oxidation kinetics from evolved carbon oxide analysis during temperature-programmed oxidation. *Carbon*, 39(5):725–732, apr 2001.
75. H. K. Chelliah, a. Makino, I. Kato, N. Araki, and C. K. Law. Modeling of graphite oxidation in a stagnation-point flow field using detailed homogeneous and semiglobal heterogeneous mechanisms with comparisons to experiments. *Combustion and Flame*, 104(4):469–480, 1996.
76. L. Tognotti, J. P. Longwell, and a. F. Sarofim. The products of the high temperature oxidation of a single char particle in an electrodynamic balance. *Symposium (International) on Combustion*, 23(1):1207–1213, 1991.
77. Roger Phillips, F J Vastola, and P L Walker. Factors of the Affecting the Product Ratio of the Carbon-Oxygen Reaction - II Reaction Temperature. *Carbon*, 8:205–210, 1970.
78. K M Kratsch, M R Martinez, F I Clayton, R B Greene, and J E Wuerer. Graphite Ablation in High Pressure Envirconments. In *AIAA Entry Vehicle Sysyems and Technology Meeting*, 1968.
79. Micheal R Rhoby and K C Gross. Application of an Imaging Fourier Transform Spectrometer to Determine Two-Dimensional Scalar Values in Laminar Flames.

In Spring Technical Meeting of the Central States Section of Combustion Institute, University of Dayton, 2012.

80. Rhoby M. R., Blunck L David, and Gross K C. Mid-IR Hyperspectral imaging of laminar flames for 2-D scalar values. *Optics Express*, 2014.
81. Michael R. Rhoby and K C Gross. IFTS for Harmonically Unsteady Combustion.pdf. In *Fourier Transform Spectroscopy; Lake Arrowhead, CA*, mar 2015.
82. Nicholas Herr. (Herr- Ts Paper Preprint). 2016.
83. M. R. Null and W. W. Lozier. Measurement of Reflectance and Emissivity of Graphite at Arc Temperature with a Carbon Arc Image Furnace. *Journal of Applied Physics*, 29(11):1605, 1958.
84. M.R Null and WW. Lozier. Spectral reflectance and emissivity of carbon and graphite. *Carbon*, 1(3):393, apr 1964.
85. Zhimin Huang, Jiansheng Zhang, Yong Zhao, Hai Zhang, Guanxi Yue, Toshiyuki Suda, and Masahiro Narukawa. Kinetic studies of char gasification by steam and CO₂ in the presence of H₂ and CO. *Fuel Processing Technology*, 91(8):843–847, 2010.
86. Carl L Yaws. Yaws' Handbook of Thermodynamic and Physical Properties of Chemical Compounds.
87. Hugo S. Caram and Neal R. Amundson. Diffusion and Reaction in a Stagnant Boundary Layer about a Carbon Particle. *Industrial & Engineering Chemistry Fundamentals*, 16(2):171–181, may 1977.
88. Ashley Gonzales, Nicholas Herr, and Glen Perram. Experimental Study of Oxidation of Laser Irradiated Graphite. pages 1–6.
89. P. L. Walker, R. J. Foresti, and C. C. Wright. Surface Area Studies of Carbon—Carbon Dioxide Reaction. *Industrial & Engineering Chemistry*, 45(8):1703–1710, aug 1953.

REPORT DOCUMENTATION PAGE

Form Approved
OMB No. 0704-0188

The public reporting burden for this collection of information is estimated to average 1 hour per response, including the time for reviewing instructions, searching existing data sources, gathering and maintaining the data needed, and completing and reviewing the collection of information. Send comments regarding this burden estimate or any other aspect of this collection of information, including suggestions for reducing this burden to Department of Defense, Washington Headquarters Services, Directorate for Information Operations and Reports (0704-0188), 1215 Jefferson Davis Highway, Suite 1204, Arlington, VA 22202-4302. Respondents should be aware that notwithstanding any other provision of law, no person shall be subject to any penalty for failing to comply with a collection of information if it does not display a currently valid OMB control number. **PLEASE DO NOT RETURN YOUR FORM TO THE ABOVE ADDRESS.**

1. REPORT DATE (DD-MM-YYYY) DD-09-2016			2. REPORT TYPE Doctoral Dissertation		3. DATES COVERED (From — To) August 2013 - September 2016	
4. TITLE AND SUBTITLE Imaging Fourier Transform Spectroscopy of Graphite Oxidation					5a. CONTRACT NUMBER	
					5b. GRANT NUMBER	
					5c. PROGRAM ELEMENT NUMBER	
6. AUTHOR(S) Gonzales, Ashley E., Capt., U.S. Air Force					5d. PROJECT NUMBER	
					5e. TASK NUMBER	
					5f. WORK UNIT NUMBER	
7. PERFORMING ORGANIZATION NAME(S) AND ADDRESS(ES) Air Force Institute of Technology Graduate School of Engineering and Management (AFIT/EN) 2950 Hobson Way WPAFB OH 45433-7765					8. PERFORMING ORGANIZATION REPORT NUMBER AFIT-ENP-DS-16-J-018	
9. SPONSORING / MONITORING AGENCY NAME(S) AND ADDRESS(ES)					10. SPONSOR/MONITOR'S ACRONYM(S)	
					11. SPONSOR/MONITOR'S REPORT NUMBER(S)	
12. DISTRIBUTION / AVAILABILITY STATEMENT APPROVED FOR PUBLIC RELEASE; DISTRIBUTION UNLIMITED.						
13. SUPPLEMENTARY NOTES This material is declared a work of the U.S. Government and is not subject to copyright protection in the United States.						
14. ABSTRACT This study investigates the kinetic and transport mechanisms of laser irradiated graphite oxidation using mid-wave infrared (MWIR) imaging Fourier transform spectroscopy (IFTS). Oxidation was studied for varying graphite materials and surface temperatures of 1000 - 4000 K in a dry air environment (20% O ₂ , < 1% H ₂ O). Samples were heating using a 1.07 μm continuous wave (CW) fiber laser while surface temperatures were monitored using a MW camera. The resulting oxidation plume was observed using MW IFTS at spectral resolution of 2 cm ⁻² and spatial resolution of 0.5 mm/pix with framing rates of 1 Hz. A two layer radiative transfer model (RTM) was used to infer spatial maps of temperature and species (CO, CO ₂) concentration from hyperspectral (spatial - spectral) data. Three flow conditions (buoyant, flat plate shear flow, and stagnation flow) were evaluated to determine the role of transport. Two simplified kinetic transport models are presented and compared with experimental data. Experimental results for the flat plate shear flow and stagnation flow represent the first spatially resolved measurements of reacting carbon oxidation flow, and are vital for validation of numerical work.						
15. SUBJECT TERMS Imaging Fourier-transform spectrometer, Graphite Oxidation, Reacting Boundary Layer, Laminar flame						
16. SECURITY CLASSIFICATION OF:			17. LIMITATION OF ABSTRACT	18. NUMBER OF PAGES	19a. NAME OF RESPONSIBLE PERSON	
a. REPORT	b. ABSTRACT	c. THIS PAGE			Dr. Glen Perram, AFIT/ENP	
U	U	U	UU	170	19b. TELEPHONE NUMBER (include area code) (937) 255-3636 x 4504; glen.perram@afit.edu	